同志社大学

DOSHISHA UNIVERSITY

Water Vapor in DC Reactive Magnetron Sputtering Plasma: Characteristics and Applications

反応性マグネトロンスパッタリングプラズマ中の水蒸気：特徴と応用

A dissertation submitted in partial fulfillment
of the requirements for the degree of
Doctor of Engineering

Plasma Physics Laboratory
プラズマ物理学研究室
Department of Electrical and Electronic Engineering
電気電子工学専攻
Graduate School of Science and Engineering
理工学研究科

CATAPANG ALLEN VINCENT BARABONA
カタパング アレン ビンセント バラボナ

2020年度 3301番

June 2023

“Sic Parvis Magna”

Sir Francis Drake

SYNOPSIS

Water Vapor in DC Reactive Magnetron Sputtering Plasma: Characteristics and Applications

by CATAPANG ALLEN VINCENT BARABONA

The use of water vapor plasma in a thin film deposition process realizes the addition of hydrogen (H) in the plasma. The added H in the thin film structure improved the film properties for oxides, such as zinc oxide (ZnO), by acting as a shallow donor dopant. By using water vapor plasma, the doping of ZnO with H onto the lattice to improve the film's conductivity and reduce lattice stresses can be realized, with intended applications in optoelectronics such as in transparent conductive electrodes. This dissertation investigated the application of water vapor as the reactive gas in a DC magnetron sputtering system. The deposition process was systematically investigated by exploring the different areas, from the introduction of water vapor, the bulk plasma, and the magnetron cathode surface, to the thin film substrate region. The reactive magnetron sputtering plasma was applied to a plasma source with a pulsed conduit-type extraction electrode.

In Chapter 2, the stable flow of water vapor into a low-pressure deposition system using a heated vaporization-driven reservoir was controlled using the temperature. Increasing the temperature increased the responsiveness of the water vapor reservoir as a gas source. Numerical simulations of the reactive magnetron sputtering process through Berg's reactive sputtering model for water vapor plasma showed that adsorption-dependent parameters significantly affected the deposition process. The effect on the pressure behavior at different discharge parameters was investigated by fitting the time-resolved pressure curves to the model, and the gas admixture was determined as the most suitable form of process control for oxide formation at the substrate region.

In Chapter 3, the effect of the water vapor plasma on the target surface condition was investigated. The dominant surface processes at the target surface region are dependent. At the target center, the redeposition of material was strong compared to the target racetrack where the erosion of target material by sputtering was dominant. Redeposited layers with preferred crystallographic orientations were observed at low water vapor content, and oxide overlayers were detected at high water vapor content settings. The oxide formation and surface morphology were compared with *in-situ* laser differential reflectance measurements, and the trends were similar to the compound formation according to Berg's sputtering model. The laser differential reflectance incident at the center was determined to be a viable method for monitoring the target surface condition during the plasma operation.

In Chapter 4, the ZnO thin films were deposited on borosilicate glass at varying water vapor content in an Ar – H_2O gas admixture. The change in film properties related was correlated to the near substrate surface plasma parameters obtained from a single Langmuir probe. The addition of water to the plasma significantly changed the behavior of the plasma and the growth mechanism of the film. The transition between a metallic Zn film to ZnO was observed with 40% water vapor content, and transparent and conductive films was deposited (87.5% transmittance, $\rho = 1.2\ \Omega$ cm). The measure confirmed the shallow H donor doping phenomenon with water vapor plasma. The effect of deposition control by adding a substrate bias and temperature was investigated in a 1.0 Pa H_2O plasma. The polarity of the substrate bias changed the incident charged species, while the bias magnitude affected the incident energy. The film characteristics were directly linked to the ion and electron flux to the surface. The shallow donor doping and optical transparency were unaffected by the substrate bias. For substrate heating, increasing the substrate temperature resulted in a localized increase in ions near the surface. As the substrate temperature increased, the growth of multiple ZnO peaks was promoted at higher temperatures while the resistivity consistently decreased. The shallow donor doping of ZnO for films deposited using water vapor plasma was stable for the 20 to 140°C range.

In Chapter 5, the production of positive and negative ions in water vapor plasma was confirmed using optical emission spectroscopy and ion energy measurements. The production of Ar^+, H^+, Zn^+, O^+, and OH^+ ions was confirmed from the atomic and molecular band spectra at the visible (400-1000 nm) and UV regions (200-500 nm). The relative intensities indicated that the maximum ion formation was at 40% water vapor content. The positive ion energy distribution across the water vapor settings had an average peak ion energy at ≈5.4 eV and the addition of water vapor to the plasma increased the peak energy by ≈0.26 eV. The negative ion energy distribution was significantly broader and at higher energies (≈274 eV for the 20 to 100% settings). The negatively-biased target surface accelerated the negative ions by ≈69 to 89% of the cathode discharge voltage.

In Chapter 6, a reactive magnetron sputtering plasma source with a pulsed, conduit-type extraction electrode was designed. The charged species transport to the differentially pumped downstream region was confirmed by quadrupole mass spectrometry (QMS). The pulsed extraction electrode extracted Ar^+, H_2O^+, H_3O^+, and Zn^+ ions, and the intensities were dependent on the extraction electrode voltage frequency. Multiple plasma characterization techniques confirmed the proposed space charge-dependent extraction mechanism. The simulation of the ion transport trajectories showed that plasma at the conduit volume was dependent on the condition at the plasma source and the extraction electrode voltage frequency. The ion current peaked at varying frequencies depending on the position inside the conduit volume. The electron saturation current steadily decreased as the frequency increased, indicating the possibility of electron trapping. The positive space charge in the conduit volume accelerated the ions further to higher energies than that set by the extraction electrode voltage (1 kHz to 250 kHz), but the trapping of electrons steadily decreased the ion energy as the frequency increased (<250 kHz). The average ion current density measured by a shielded Faraday cup exhibited an average ion current density with a Gaussian profile centered at 171 kHz. For the time-resolved measurements, the indirect time-of-flight showed that the extraction electrode voltage could control the mass ratio of extracted ions, with lower voltages favoring heavier ions. The addition of water vapor significantly complicated the behavior of the ion extraction and negative ions were detected by the Faraday cup. A positive tailing pulse in the off phase realized an increased ion extraction density compared to a similar increase in the extraction electrode voltage.

Chapter 7 states the main results of each of the chapters and the recommendations for further investigations in regards to water vapor in reactive plasma.

Acknowledgements

I would like to acknowledge the contributions of several people towards the completion of this doctoral dissertation.

To my adviser, Dr. Motoi Wada, I am deeply indebted to you for all the knowledge and wisdom that you have imparted to me, and the unwavering support towards the various experiments that were performed in this dissertation. Thank you for believing in me and helping me become the researcher that I am today.

I would like to thank Doshisha University, its professors,, and the ISTC and OIS staff, for all the help and support throughout my stay here in Doshisha University. In particular, I would like to thank Dr. Yuuki Sato and Dr. Tadashi Ohachi of the Electronic Materials Laboratory, for teaching me in solid state materials physics and the X-ray diffraction technique.

To the students of the Plasma Physics Laboratory throughout my whole stay in Doshisha University, for the acceptance and the camaraderie during the my experiments. In particular, I would like to thank my undergraduate kouhai, Hirotaka Tatematsu and Shinsaku Inoue, for the help in experiments.

To my Filipino colleagues and friends for the camaraderie in my stay here in Japan. In particular, to my batchmates, Keith Nealson Penado and Aliena Mari Miranda, and co-authors in publications and presentations, James Edward Hernandez, Marlo Nicole Gilos, Oliver Streeter, Jose Gabriel Abalos, and Arantxa Danielle Montallana.

I'd also like to extend my gratitude to my family, for the encouragement that I can accomplish this venture.

To my cats, Mingmong, Juju and the litter, Splooty, Nathaniel, Natasha and Tiger, for the cute, calm, and judging presence.

Lastly, I would like to specially thank Nelly Karen Viktoria D. Rosales, for the unconditional support, encouragement, and the patience with me as I finish my 5-year stay here in Doshisha University. You are the foundation which has made all of this possible.

CONTENTS

Synopsis iii

Acknowledgements vi

List of Figures xvii

List of Tables xviii

List of Abbreviations xix

Physical Constants and Units xx

List of Symbols xxi

1 Introduction 1
- 1.1 Overview . . . 1
  - 1.1.1 Sputtering Process . . . 1
- 1.2 Objectives . . . 2
- 1.3 Organization of the Study . . . 2
- 1.4 Related Works . . . 3
- References . . . 4

2 Water Vapor Plasma in Magnetron Sputtering Discharges 6
- 2.1 Water vapor in low pressure deposition systems . . . 6
- 2.2 Experimental system . . . 7
- 2.3 Water vapor reservoir . . . 8
  - 2.3.1 Vaporization mechanism and gas flow . . . 9
  - 2.3.2 Effect of temperature to flow control . . . 10
- 2.4 Simulation of Water Vapor Plasma in Reactive Magnetron Sputtering . . . 12
  - 2.4.1 Berg's model for reactive magnetron sputtering . . . 13
  - 2.4.2 Effect of adsorption-dependent parameters . . . 14
- 2.5 Time-resolved pressure measurements . . . 15
  - 2.5.1 Effect of working pressure . . . 16
  - 2.5.2 Effect of discharge current . . . 18
  - 2.5.3 Effect of water vapor content . . . 19
- 2.6 Summary of Results . . . 21
- References . . . 22

3 Plasma surface processes in water vapor reactive sputtering 24
- 3.1 Introduction . . . 24
- 3.2 Target Surface Characterization . . . 24

3.2.1 Target Composition using X-ray Diffraction 25
3.2.2 Surface Morphology using Laser Microscopy 25
3.2.3 *In-situ* Laser Differential Reflectance Spectroscopy 25
3.3 Experimental System 26
3.3.1 Target cathode configuration and Differential Reflectance Spectroscopy . 27
3.3.2 Surface Composition and Morphology 29
3.4 Results and Discussion 29
3.4.1 Target Composition 31
3.4.2 Surface Morphology 33
3.4.3 Laser Differential Reflectance Spectroscopy 36
3.5 Summary of Results 38
References 39

4 Deposition of ZnO thin films using water vapor plasma 41
4.1 Introduction 41
4.2 Thin Film Deposition 41
4.3 Experimental System 42
4.3.1 Substrate Holder Design 42
4.3.2 Near Surface Single Langmuir Probe 44
4.3.2.1 Langmuir Probe Theory 44
4.3.2.2 Experimental Configuration 46
4.3.2.3 Analysis of Langmuir Probe Trace 47
4.3.3 Materials Characterization Techniques 48
4.3.3.1 X-ray Diffraction and Reflectivity 49
4.3.3.2 Optoelectronic Properties 50
4.4 Effect of Water Vapor 51
4.4.1 Plasma Parameters 52
4.4.2 Film Properties 55
4.5 Effect of Substrate Bias 58
4.5.1 Plasma Parameters 58
4.5.2 Film Properties 59
4.6 Effect of Substrate Heating 60
4.6.1 Ambient Heating from the Plasma 60
4.6.2 Plasma Parameters 60
4.6.3 Film Properties 61
4.7 Summary of Results 62
References 64

5 Ion Formation of Water Vapor Plasma in Reactive Magnetron Sputtering 69
5.1 Introduction 69
5.1.1 Reactive Characteristics of Water Vapor Plasma 69
5.2 Experimental System 70
5.2.1 Optical Emission Spectroscopy 70

5.2.1.1 Experimental Configuration and Analysis 71
5.2.2 Retarding Potential Analyzer 72
5.2.2.1 Experimental Configuration and Analysis 73
5.3 Optical Emission Spectroscopy of Water Vapor Plasma 74
5.3.1 The Effect of Water Vapor Content 74
5.4 Ion Energy Measurements of Water Vapor Plasma 76
5.4.1 Positive Ion Energy Measurements. 77
5.4.2 Negative Ion Energy Measurements 79
5.5 Summary of Results 81
References 83

6 Ion transport control using a pulsed conduit-type extraction electrode 86
6.1 Introduction 86
6.2 Magnetron Plasma Sources 86
6.3 Experimental System 87
6.3.1 Pulsed Conduit-type Extraction Electrode 88
6.4 Plasma Source Characterization Techniques 89
6.4.1 Quadrupole Mass Spectrometry 90
6.4.2 Ion Current Measurements by Faraday Cup 90
6.4.3 Retarding Potential Energy Analyzer 91
6.4.4 Langmuir Probe Measurements 91
6.4.5 Finite Element Simulations 92
6.5 Mass Dependent Ion Extraction 93
6.5.1 Detection by Quadrupole Mass Spectrometry 93
6.5.2 Effect of the Pulsed Extraction Potential 94
6.6 Extraction Characteristics of a Pulsed Conduit-type Electrode 97
6.6.1 Simulation of Ion Extraction Mechanism 97
6.6.2 Ion and Electron Transport using a Single Langmuir Probe 99
6.6.3 Ion Energy Distributions 101
6.6.4 Ion Current Measurements 102
6.6.4.1 Average and Peak-to-Peak Current Density Measurements . . . 102
6.6.4.2 Phase Dependent Measurement 104
6.7 Summary of Results 107
References 108

7 Conclusions and Recommendations 110
7.1 Conclusions 110
7.2 On the stable introduction of water vapor plasma and simulation using a reactive magnetron sputtering model 110
7.3 On the surface processes at the target surface region 110
7.4 On the deposition of ZnO thin films 111
7.5 On the positive and negative ion production 111

7.6 On the controlled ion transport using a pulsed-conduit type extraction electrode system 112
7.7 Further Studies and Recommendations 112

A Chapter 2: Supplementary Data

B Energy Distribution from Retarding Potential Analyzers

LIST OF FIGURES

1.1 Schematic depicting the interaction of energetic ions with surfaces. 2

2.1 (*Left*) The Lennard Jones potential energy plot of a water vapor molecule at the surface at a specific distance, x, and (*right*) the possible chamber wall processes when adsorbed phases are present. 7
2.2 The reactive magnetron sputtering system. The magnetic field lines are shown to indicate an unbalanced magnetron configuration. 8
2.3 The vaporization-driven, heated water reservoir used in this study. The highlighted area in the red indicates the heated portions of the reservoir 9
2.4 *(Left)* The effect of water reservoir heating temperature to the chamber pressure upon opening and closing of the water vapor reservoir, and *(Right)* the effect of the second metering valve aperture to the equilibrium pressure at a temperature of 65^{o}C. The temperature indicated is the water reservoir temperature. 11
2.5 The effect of the water reservoir heating temperature to the effective pumping speed, S *(left)*, and the flux, F_{sat} *(right)*, at varying temperatures and flow rate . . 12
2.6 Fitting of $\frac{1}{\Delta p}$ against $T^{\frac{1}{2}}$ of the water reservoir at different flow rates 12
2.7 The surface processes considered in the time-resolved Berg's reactive sputtering model 13
2.8 The effect of the α ratio, the $\frac{Y_c}{Y_m}$, and $k(n_s)$ to the pressure of the discharge for water vapor plasma. Unless specified, the typical settings were: α_t = 8x10^{-5}, α_s = 9x10^{-5}, Y_m = 1.0, Y_c = 2.5x10^{-3}, and k = 720. The discharge current (100 mA) and the working pressure (1.0 Pa) was kept throughout. 15
2.9 Fitting of the averaged pressure curves of 1.0 Pa H_2O plasma to Berg's time-resolved reactive magnetron sputtering model at 100 mA discharge current. The parameters obtained from fitting are: α_t = 8.0x10^{-5}, α_s = 9.0x10^{-5}, Y_c = 2.5x10^{-3}, $k(n_s)$ = 720 (χ^2= 1.63x10^{-4}). 16
2.10 The effect of the water vapor working pressure to the sticking coefficient (α) at the target and substrate regions and the sputtering yield, Y_c. The dashed and the dotted lines are to guide the eyes. 17
2.11 The effect of the water vapor working pressure to the compound fraction (θ) at the target and substrate regions as determined experimentally with the pressure curve fitted to Berg's model. The trend lines show what is theoretically predicted by varying the working pressure directly with the parameters used in Fig. 2.9. . . 17
2.12 The effect of the water vapor plasma discharge current to the sticking coefficient (α) at the target and substrate regions, the sputtering yield, Y_c, and the surface site density $k(n_s)$. The dashed and the dotted lines are to guide the eyes. 18

2.13 The effect of the discharge current to the compound fraction (θ) at the target and substrate regions as determined experimentally with the pressure curve fitted to Berg's model. The trend lines show what is theoretically predicted by varying the working pressure directly with the parameters used in Fig. 2.9. 19
2.14 The effect of the water vapor plasma discharge current to the sticking coefficient (α) at the target and substrate regions, the sputtering yield, Y_c, and the surface site density $k(n_s)$. The dashed and the dotted lines are to guide the eyes. 20
2.15 The effect of the gas admixture, Ar-H_2O, to the compound fraction (θ) at the target and substrate regions as determined experimentally with the pressure curve fitted to Berg's model. The dotted lines are to guide the eyes, and is proportional to a 1:1 correspondence of θ to the water vapor content. 21

3.1 The reactive magnetron sputtering system with a differential reflectance spectroscopy setup. The setup was changed to realize a 65^o incidence angle for the 405 nm laser incident onto the target surface. 26
3.2 The cathode and the relative placement of the concentric toroidal magnets forming the magnetron sputtering cathode. 27
3.3 (Left) The magnetic flux density at different positions across the unbalanced magnetron cathode surface and (right) the magnetic flux density at varying distances from the target surface at the center and racetrack positions. 27
3.4 The intensity of the incident 405 nm laser at different polarization and the optical spectra of the reflected laser at different target conditions and 1.0 Pa Ar plasma duration 28
3.5 The optical emission spectra of the magnetron sputtering discharge at 1.0 Pa Ar and 1.0 Pa water vapor. The discharge current is at 100 mA. The peaks from the discharge support gas, Ar, the reactive gas, water vapor, and the Zn metal are indicated. The peak position for the 405 nm laser is indicated. 29
3.6 The 70.0 mm Zn metal target surface images at different instances: after SiC cleaning, after 1.0 Pa Ar cleaning, and after 10 minutes of reactive magnetron sputtering at varying water vapor content. 30
3.7 The target surface composition at the center and racetrack region of the as-prepared, cleaned, 0% and 20% water vapor content settings as measured by X-ray diffraction. 31
3.8 The target surface composition at the center and racetrack region for the 50% and 100% water vapor content as measured by X-ray diffraction and indicating the formation of the ZnO at the target surface through the (100) and (002) peaks. 32
3.9 The ratio of the XRD peak intensity at $2\theta = 36^o$ and 43^o at increasing water vapor content. The ratio is compared with the compound target fraction at the target, θ_t, and at the substrate, θ_s, obtained from fitting discharge pressure curves to Berg's time-resolved reactive magnetron sputtering model. The dashed lines are to guide the eyes 33

3.10 Target surface images under a laser microscope at varying water vapor content, at the center and the racetrack region 34
3.11 The effect of the water vapor content to the R_a and R_{sk} of the center and racetrack regions at an increasing water vapor content. The dashed lines are there to guide the eyes and highlight the change in the measured parameters. 35
3.12 The differential reflectance of the 0%, 20%, 50% and 100% water vapor content settings against the discharge duration, at 1 minute intervals, for a total duration of 10 minutes. 36
3.13 The differential reflectance and the H_α/Zn I ratio from the OES, at varying water vapor content and discharge duration 37
3.14 The averaged differential reflectance (5 to 10 minutes) at increasing water vapor content. The compound fraction θ_t and θ_s from Berg's time-resolved reactive magnetron sputtering model are shown as comparison. The dashed lines are to guide the eyes. 37

4.1 The reactive magnetron sputtering system with the substrate holder-Langmuir probe configuration for the near substrate surface measurements. The optical emission spectroscopy was performed at an axial axis without the substrate holder. 42
4.2 The effect of 1.0 Pa Ar cleaning on the measured discharge voltage and the H_α to Zn I ratio obtained using optical emission spectroscopy (OES) at the central axis as indicated in Fig. 4.1. The target was exposed to a 1.0 Pa water vapor plasma prior to the cleaning step. 43
4.3 The near substrate Langmuir probe setup with the substrate heating and bias configuration utilized. The heating was realized using a resistive substrate heater and the bias was powered using a DC power supply. The whole configuration is mounted on a rotational feedthrough 44
4.4 The single Langmuir probe tip configuration used for the near surface measurements. 46
4.5 The typical single Langmuir probe trace and how the plasma parameters (V_f, $I_{ion,sat}$, T_e, V_p) were measured. The blue trace indicates the probe current, and the red trace indicates the electron current, $I_{electron}$, at a 1.0 Pa Ar plasma, at a 100 mA discharge current. The inset graph shows the fitting of the two T_e typically observed for magnetron sputtering plasmas. 47
4.6 The electron energy distribution obtained using the Druyvesteyn method for 0%, 50%, and 100% water vapor content settings. 49
4.7 The Gaussian peak fitting of the XRD peak for the β and peak area 50
4.8 The typical normalized X-ray reflectivity (XRR) of ZnO deposited using 1.0 Pa water vapor plasma. The Kiessig fringes and the component correlated with the roughness in the XRR data are shown. 51
4.9 The Tauc plot for the measurement of the deposited thin film's band gap. The x-interecept of the linear portion of the plot denotes the film's band gap. 52

4.10 The XRD peaks obtained from the deposited film samples at varying Ar-H_2O content . . . 53
4.11 The X-ray reflectivity curve of the thin films deposited at varying Ar-H_2O content. 54
4.12 The transmittance of the deposited thin films at varying Ar-H_2O content. The inset images show the actual images of the deposited films on the glass substrate. 54
4.13 The effect of water content on the plasma parameters, as measured by a single Langmuir probe. . . . 55
4.14 Optical emission spectra of 1.0 Pa water vapor at the UV (200-400 nm) and visible (400-900 nm) region. The atomic and molecular spectra for H, O, OH, and Zn are highlighted . . . 56
4.15 Discharge voltage measurements at varying water vapor content . . . 56
4.16 The effect of water content on the film's properties . . . 57
4.17 Effect of the substrate bias (-50 to 50 V) to the measured near surface plasma characteristics and the deposited film's properties. . . . 58
4.18 Ambient heating from the plasma as measured by a K-type thermocouple for a duration of 10 minutes, at varying water vapor content (0%, 50% and 100% water vapor content). . . . 61
4.19 Effect of substrate temperature (20^o to 140^o C) to the measured near surface plasma characteristics and the deposited film's properties. . . . 62
4.20 The XRD peaks ((100), (002) and (101)) of ZnO films deposited at varying substrate temperatures. The working pressure is kept at 1.0 Pa of water vapor, and 100 mA discharge. . . . 63

5.1 The electron impact ionization and dissociative electron attachment cross sections for the H_2O molecule and Ar [1–3]. The dissociative electron attachment for H_2O^- does not account for rotovibrational states. . . . 70
5.2 The experimental system in the optical emission spectroscopy measurement configuration . . . 71
5.3 The mechanism for a triple-plate retarding potential analyzer to measure the ion energy distribution of plasma . . . 72
5.4 The retarding potential analyzer (RPA) schematic used for ion energy distribution measurements of the reactive magnetron sputtering plasma containing water vapor. . . . 73
5.5 The optical emission spectra at the visible range (400-1000 nm) and UV range (200-500 nm) at varying water vapor content . . . 75
5.6 The OES peak intensity ratios of Ar I, H (Balmer Series), and OH ($A^2\Sigma^+ \rightarrow X^2\Pi$) at varying water vapor content. The Ar I and H intensity ratios were taken at the visible wavelength region (400-1000 nm) and the OH band spectra was taken at the UV wavelength region (200-500 nm). . . . 76
5.7 The typical Faraday cup current and the positive ion energy distribution obtained from the RPA using the biased Faraday cup detection circuit. This measurement was taken at 1.0 Pa, 100 mA discharge current. . . . 77

5.8 The positive ion energy distributions measured by the RPA at 0 to 50% and 100% water vapor content. 78
5.9 The (a) peak position and the change in current, ΔCurrent, and (b) the peak characteristic ratios ($Peak_2/Peak_1$) at varying water vapor content. The lines are added to guide the eyes. 79
5.10 The negative ion energy distributions measured by the RPA at 0 to 50% and 100% water vapor content. 80
5.11 The peak position and the peak-to-cathode voltage ratio of the negative ion energy distributions measured using the RPA. The lines were added to guide the eyes. 81

6.1 The reactive magnetron sputtering plasma source system with the pulsed conduit-type extraction electrode. Differential pumping of the plasma source from the downstreamr region was accomplished using the conduit-type electrode aperture. 87
6.2 The pressure ratio of the plasma source region and the downstream region at varying plasma source pressure. The difference was approximately two orders of magnitude lower when using the 2.0 mm diameter aperture. The dashed lines indicate a logarithmic relation between the ratio and ion source pressure (r^2 = 0.932) 88
6.3 The pulsed, conduit-type extraction electrode used in this study. The ground plate aperture was set at 2.0 mm diameter, and the extraction gap and length was 4.8 mm and 72 mm, respectively. PTFE insulators isolate the conduit from the grounded plasma source and downstream region. 89
6.4 The positive tailing pulse after the negative voltage phase of the pulsed extraction voltage 89
6.5 The schematic of a typical quadrupole mass spectrometer. Ions of with a specific mass-to-charge ratio are able to reach the detector at the z-axis direction, while lighter or heavier ions result to unstable trajectories and are collected at the electrodes. 90
6.6 The different Faraday cup configurations used in this study. (a) shows the front shielded configuration, while (b) shows a fully shielded configuration with a magnet filter. 91
6.7 The retarding potential energy analyzer schematic used for the plasma source ion extraction energy measurements. The retardation bias and current were supplied and measured simultaneously using a 4-wire source measure unit. 92
6.8 The mass spectra for 1.0 Pa Ar and 1.0 Pa H_2O plasma in the reactive magnetron sputtering plasma source (A) without pulsed extraction and (B) with pulsed extraction. The filament ionizer in the RGA was used for the detection of the neutral species transport to the downstream region for the case (A) without pulsed extraction. 93
6.9 The effect of the pulse frequency to the mass spectra peak intensity for Ar^+, H_2O^+, H_3O^+ and Zn^+ ions 94

6.10 The effect of varying the pulse extraction potential to the current measured using a front-shielded Faraday cup in Fig. 6.6a and the peak current magnitude as the extraction pulse voltage was increased. 94
6.11 The proposed mechanism for the pulsed conduit-type extraction electrode configuration. 95
6.12 The ion current at varying extraction pulse frequencies, measured from the mass spectra. The gas ions, Ar^+ and H_2O^+, and sputtered metal, Zn^+, are shown. . . . 96
6.13 The effect of the space charge to the ion transport in the pulsed conduit-type extraction electrode as simulated by the finite element method using AMaze software. The divergence of the trajectories are highlighted. 97
6.14 (a) The extraction electrode aperture after use in the pulsed conduit-type extraction electrode. A film deposit approximately 8.5 mm can be seen, indicating a 68.2^o beam divergence as it enters the conduit volume. (b) The electric field components (x, y and z directions) across the central axis of the experimental system as obtained from the space charge-considered ion transport trajectories in Fig. 6.13. 98
6.15 The effect of the initial energy at the plasma source and the extraction electrode voltage frequency to ϕ at varying positions along the central axis of the extraction electrode configuration. 99
6.16 The ion and electron saturation current measured from single Langmuir probes measured in the conduit volume for 1.0 Pa Ar, 100 mA discharge current plasma and a -100 V pulse extraction voltage. The positions are based on the exit aperture location, where 0 mm was at the exit aperture and the 55 mm position was 5 mm away from the entrance aperture. 99
6.17 The effect of a positive tailing pulse to the $I_{ion,sat}$ and $I_{e,sat}$ obtained from single Langmuir probe measurements at the exit aperture position. 100
6.18 The typical ion energy distribution obtained from the retarding potential analyzer, for 1.0 Pa Ar plasma at 100 mA discharge current extracted using a 100 kHz, 100 V extraction electrode voltage pulse. 101
6.19 (A) The comparison of the simulation results to the measured ion energy distribution of the extracted ions at a 100 kHz, -100 V pulsed extraction voltage of 1.0 Pa Ar plasma. (B) The effect of the extraction electrode voltage frequency to the peak position of the ion energy. 102
6.20 The steady state ion current density measurements at varying discharge and extraction parameters. 103
6.21 The typical Faraday cup signal obtained in Sec. 6.6.4 at the off phase. The Gaussian deconvolution of the signal yielded six peaks present in the signal. Peak 3 corresponded to an ion mass of 40.6 amu. 104
6.22 The analysis method for obtaining t_{ion} using the indirect time-of-flight measurement method that uses the phase-dependent measurements of a lock-in amplifier. 105
6.23 The ion transit time, t_{ion}, as measured from the phase shift, at varying discharge and extraction parameters 106

A.1 The fit of the pressure at varying water vapor plasma working pressures . . . . .
A.2 The fit of the pressure at varying water vapor plasma discharge currents . . . . .
A.3 The fit of the pressure at varying water vapor content . . . .

LIST OF TABLES

5.1 The electron impact ionization and electron attachment reactions for the water molecule. Argon is shown for comparison. [1–3] 69

A.1 Parameters for the fitting of the time-dependent pressure at varying water vapor pressure . . . .
A.2 Parameters for the fitting of the time-dependent pressure at varying discharge current . . . .
A.3 Parameters for the fitting of the time-dependent pressure at varying Ar - H_2O content . . . .

LIST OF ABBREVIATIONS

CVD	**C**hemical **V**apor **D**eposition
DC	**D**irect **C**urrent
DRS	**D**ifferential **R**eflectance **S**pectroscopy
EEDF	**E**lectron **E**nergy **D**istribution **F**unction
FWHM	**F**ull **W**idth at **H**alf **M**aximum
IEDF	**I**on **E**nergy **D**istribution **F**unction
OD	**O**ptical **D**ensity
OES	**O**ptical **E**mission **S**pectroscopy
PVD	**P**hysical **V**apor **D**eposition
QMS	**Q**uadrupole **M**ass **S**pectrometry
RF	**R**adio**f**requency
RGA	**R**esidual **G**as **A**nalyzer
RPA	**R**etarding **P**otential **A**nalyzer
SCCM	**S**tandard **C**ubic **C**entimeter per **M**inute
SUS	**S**teel **U**se **S**tainless, Stainless steel
TMP	**T**urbo**m**olecular **P**ump
UV	**U**ltra**v**iolet
XRD	**X**-**r**ay **D**iffraction
XRR	**X**-**r**ay **R**eflectivity
ZnO	**Z**i**n**c **O**xide

PHYSICAL CONSTANTS

Atomic Mass Unit	amu = 1.660540199 x 10^{-27} kg
Avogadro's Constant	N_A = 6.02214076 x $10^2$3 mol^{-1}
Boltzmann's Constant	k_B = 1.380649 x 10^-23 m^2 kg s^{-2} K^{-1}
Copper K_α	Cu K_α = 1.540598 Å
Electron charge	q = 1.60217663 x 10^{-19} C
Electron mass	m_e = 9.1093837 x 10^{-31} kg
Electron Volt	eV = 1.60217663 x 10^{-19} J
Electron Volt (Temperature)	eV = 11,604.51812 K
Euler's number	e = 2.71828 (approx)
Exponent of Interaction Potential (Thompson's Random Cascade Model)	m_k = 0.2
Gauss	G = 10^{-4} T
Permittivity of Vacuum	ϵ_o = 8.8541878128 x 10^{-12} F m^{-1}
Pi	π = 3.14159265359 (approx.)
Planck's constant	h = 6.62607015 x 10^{-34} J Hz^{-1}
Probe Correction Factor (4-point probe)	K_o = 4.0095 (dependent on probe geometry)
Shape Factor (Debye-Scherrer Equation)	K = 0.94 (ZnO)
Speed of Light	c = 2.99799245 x 10^8 m s^{-1}

LIST OF SYMBOLS

α	Sticking Coefficient
α^+	heating rate
α_{tauc}	Absorption Coefficient
A	Area
A_j	Einstein Coefficient
β	Full width at half maximum
d	Interatomic spacing
$d_{conduit}$	Conduit length
E	Energy
$E_{p-probe}$	V_p - V_{probe}
E_g	Band Gap
E_λ	Photon Energy
E_{sb}	Surface Binding Energy
F	Gas Flux
$f(E)$	Distribution Function
$f(x, y, z, v, t)$	Electron Distribution Function
G_{flow}	Vaporization Flow Rate
g_j	Degeneracy
$I(E, t)$	Intensity
$I_{electron}$	Electron Current
$I_{e,sat}$	Electron Saturation Current
I_{ion}	Ion Current
$I_{ion,sat}$	Ion Saturation Current
J_{ion}	Ion Current Density
j_e	Current Density
λ	Wavelength
λ_D	Debye Shielding Length
M	Molecular Weight
m	Mass of atom or molecule
τ (pressure)	Time constant ($\tau = \frac{\nu}{S}$)
T	Temperature
T_e	Electron Temperature
T_{tr}	Transmittance
t_{film}	Film Thickness
θ_{xrd}	Bragg Diffraction Angle
θ_t, θ_s	Compound Fraction
θ_M	Kiessig Fringes Angle
θ_c	Critical Angle (XRR)
t_{ion}	Ion Transit Time
θ_{xrr}	Diffraction angle (XRR)
$p(t)$	Pressure
p_{sat}	Saturation Pressure
n	Number of molecules
n_e	Electron Density
n_i	Ion Density
n_s	Surface Site Density
n_{ref}	Order of reflection
ϕ	Potential
Q	Gas Flow Rate
r^2	Coefficient of Determination
ρ	Resistivity
ΔR	Change in Reflectance
R	Reflectance
R_{res}	Resistance
R_a	Roughness
R_{sk}	Skewness
S	Effective Pumping Speed
ν	Volume
ν_λ	Frequency at wavelength, λ
v	Velocity
V	Voltage
V_f	Floating Potential
V_p	Plasma Potential
V_{bias}	Bias Voltage
χ^2	Chi-square Test
Y_c, Y_m	Sputtering Yield
z	Stoichiometric Factor

Chapter 1

INTRODUCTION

1.1 Overview

Water vapor in a state of plasma has applications in surface treatment and modification [1–3] and thin film deposition processes. In oxide film deposition, water vapor can substitute conventional oxygen gas, such as in titanium oxide (TiO_2), indium oxide (In_2O_3), chromium oxide (CrO), tin oxide (SnO_2), and zinc oxide (ZnO) [4–11]. The advantage of water vapor over O_2 gas is the addition of hydrogen (H) ions into the plasma. The presence of H in the plasma could result in the shallow donor doping of H into ZnO thin films. The shallow donor doping improved the film conductivity and minimized the lattice stresses on the film surface while minimizing changes in the band structure (ΔE_g < 50 meV) [12–15]. This modification allows the use of ZnO for optoelectronic applications, such as in transparent conductive electrodes [16, 17], quantum dots [18], thin film transistors [19, 20], etc.

The behavior of water vapor in low-pressure environments is highly complicated [21]. This complexity hinders its widespread application in deposition processes when precise control is required. In physical vapor deposition (PVD) or chemical vapor deposition (CVD) processes, the water molecules adsorb easily onto surfaces in the vacuum system. The adsorbed species are then difficult to desorb, as they can form multiple layers of water molecules on the surface via a combination of physisorption and chemisorption. Removing these adsorbed species is difficult and time-consuming, as the energy of adsorption is in the range of 0.8 to 1.08 eV [21–25]. The introduction of water vapor to the bulk plasma can result in the addition of differently charged species because of numerous possible reaction pathways. The reactions can range from electron impact ionization, dissociation, neutralization, and ion-ion or ion-to-neutral interactions. It can also dissociate to form negative ions [26] and has multiple rotational-vibrational states [27, 28] that further complicate the process. The stable vapor flow from a water reservoir is difficult, as the adsorbed species can affect the pressure readings causing inaccurate pressure control [29]. The phase change from a liquid reservoir to the gas phase is not as direct when compared to an inert gas, resulting in a low flow rate for water vapor. In electrically biased surfaces, the adsorbed species can act as an insulating layer that produces an inhomogeneous plasma and electric field distribution.

1.1.1 Sputtering Process

Sputtering is a commonly used method in thin film deposition. The process, as shown in Fig. 1.1, involves the removal of material from a surface due to an incident energetic particle. Depending on its ion energy, the incident particle can result in sputter removal and secondary electron emission, ion implantation of the bulk material, or its reflection from the surface. These incident particles modify the surface structure through changes in the lattice from the added

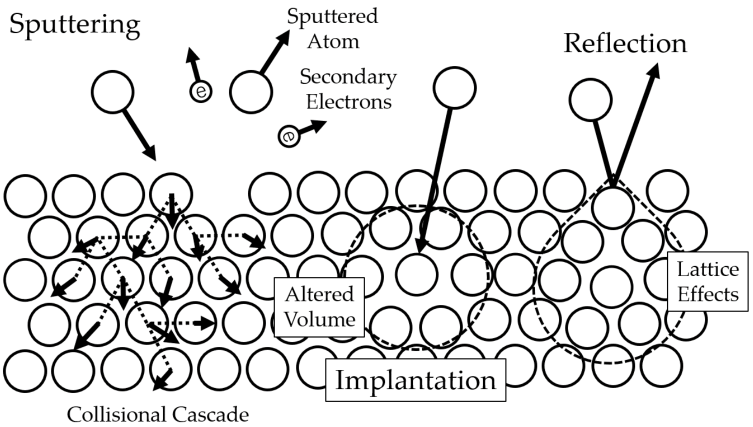

FIGURE 1.1: Schematic depicting the interaction of energetic ions with surfaces.

energy by the reflected particle, the presence of the implanted ions that distort the lattice spacing, or through collisional cascades that can remove multiple atoms or terminate and dissipate energy as heat to the surface [30]. Given these processes, it is necessary to characterize its behavior at the bulk plasma and with the surface processes relevant to the sputtering phenomenon to realize the potential of water vapor for the sputter deposition processes.

1.2 Objectives

This dissertation aims to improve the understanding of water vapor as a plasma in reactive magnetron sputtering and identify key operating parameters and mechanisms required to allow control over the deposition process and take advantage of its unique behavior. The focus of the study was on three regions: the bulk plasma, the target surface, and the substrate region. Specifically, the main objectives are as follows:

- To stabilize the introduction of water vapor into low-pressure deposition systems and predict its behavior when used in the reactive magnetron sputtering plasma.
- To identify the effect of water vapor on the surface processes in a reactive magnetron sputtering discharge, and to quantify the change in the target surface as the reactive plasma discharge is sustained.
- To determine the effect of using water vapor plasma in ZnO thin film deposition at varying conditions in terms of the near substrate surface plasma and the deposited thin film.
- To identify the species produced when the magnetron sputtering plasma with water vapor plasma is utilized and extend this to applications in plasma sources.

1.3 Organization of the Study

The succeeding chapters in this dissertation aim to explain the behavior and characteristics of water vapor plasma at different areas of interest in a reactive magnetron sputtering discharge and an extension of the application to plasma sources. Chapter 2 discusses the introduction of water vapor into a reactive magnetron sputtering system, and the simulation of the pressure behavior of water vapor plasma during its operation with a reactive magnetron sputtering model highlighted its adsorption behavior. Chapter 3 involves the effect of using water vapor on the target surface cathode, and an *in-situ* method for probing the surface during operation, differential reflectance spectroscopy, was explored. Chapter 4 examines the film formation process using water vapor plasma at varying deposition conditions and explains the effect of the near surface plasma characteristics on the measured film properties. Chapter 5 explores the reactive attributes of the bulk plasma for water vapor, particularly the positive and negative ion formation in magnetron sputtering plasma. Chapter 6 extends the application of water vapor plasma to a reactive magnetron sputtering plasma source with a pulsed conduit-type extraction electrode, which aims to improve ion transport control to a surface, given the presence of multiple species in the ion source. Chapter 7 summarizes the main points of this dissertation, as well as recommendations for future work involving water vapor plasma.

1.4 Related Works

The published works related to this dissertation are correlated to the chapters of this dissertation, as listed:

- Chapter 2:
  - A.V. Catapang, "The glow discharge ignition behavior of a DC magnetron water vapor plasma," Master's Thesis, Dept. Elect. Electron. Eng., Doshisha University, Kyotanabe, Kyoto, 2020
  - A.V. Catapang and M. Wada, "Effect of adsorption and reactive behavior of water vapor in reactive magnetron sputtering simulations using Berg's model," in The 40th JSST Annual International Conference on Simulation Technology Conference Proceedings, 2021, pp. 49-52. 2021
- Chapter 3:
  - A.V. Catapang, H. Tatematsu, O. Streeter, J.E. Hernandez, M. Vasquez and M. Wada, "Surface condition of Zn target in a DC reactive magnetron sputtering plasma source using water vapor plasma," Plasma and Fusion Research, vol. 17, pp.2406040-1-2406040-5, 2022.
- Chapter 4:
  - A.V. Catapang, J.G. Abalos, J.E. Hernandez, M. Vasquez and M. Wada "Near substrate surface plasma characteristics of ZnO film deposition in DC reactive magnetron sputtering with water vapor," Japanese Journal of Applied Physics, vol. 62, pp. SL1024-1-SL1024-7, 2023
  - A.V. Catapang, H. Tatematsu, S. Inoue and M. Wada "Effect of substrate heating and bias on the DC reactive magnetron sputtering of ZnO using Ar-H_2O plasma," in the Proceedings of the Samahang Pisika ng Pilipinas 41st Samahang Pisika ng Pilipinas Physics Conference, pp. SPP-2023-3C-04-1-SPP-2023-3C-04-4, 2023
- Chapter 6:
  - A.V. Catapang, J.E. Hernandez, M. Vasquez and M. Wada, "Performance of a reactive magnetron sputtering ion source using water vapor plasma," Journal of Physics: Conference Series, vol. 2244, pp.012099-1-012099-5, 2022.

References

[1] A. Sarani, A. Nikiforov, N. D. Geyter, R. Morent, and C. Leys, "Surface modification of polypropylene with an atmospheric pressure plasma jet sustained in argon and an argon/water vapour mixture," *Applied Surface Science*, vol. 257, 8737–8741, 20 2011.

[2] A. Y. Nikiforov, A. Sarani, and C. Leys, "The influence of water vapor content on electrical and spectral properties of an atmospheric pressure plasma jet," *Plasma Sources Science and Technology*, vol. 20, 1 Feb. 2011.

[3] T. Acsente, M. D. Ionita, M. Teodorescu, V. Marascu, and G. Dinescu, "Surface modification of polymethylmethacrylate foils using an atmospheric pressure plasma jet in presence of water vapors," *Thin Solid Films*, vol. 614, 25–30, Sep. 2016.

[4] T. Nakada, Y. Ohkubo, and A. Kunioka, "Effect of water vapor on the growth of textured zno-based films for solar cells by dc-magnetron sputtering," *Japanese Journal of Applied Physics*, vol. 30, 3344–3348, 12 R 1991.

[5] Q. J. Jiang, J. G. Lu, Y. L. Yuan, L. W. Sun, X. Wang, Z. Wen, Z. Z. Ye, D. Xiao, H. Z. Ge, and Y. Zhao, "Tailoring the morphology, optical and electrical properties of dc-sputtered zno:al films by post thermal and plasma treatments," *Materials Letters*, vol. 106, 125–128, 2013.

[6] T. Koida, H. Fujiwara, and M. Kondo, "Hydrogen-doped in2o3 as high-mobility transparent conductive oxide," *Japanese Journal of Applied Physics, Part 2: Letters*, vol. 46, 25-28 2007.

[7] B. Jeong, D. Norton, J. Budai, and G. Jellison, "Epitaxial growth of anatase by reactive sputter deposition using water vapor as the oxidant," *Thin Solid Films*, vol. 446, 18–22, 2004.

[8] C. Nouvellon, J. P. Dauchot, M. Hecq, and H. Cornil, "Chromium reactive sputtering in argon-oxygen and argon-water vapor mixtures," *Surface and Coatings Technology*, vol. 200, 425–430, 1-4 SPEC. ISS. 2005.

[9] N. Hayashi, S. Tsutsui, T. Tomari, and W. Guan, "Sterilization of medical equipment using oxygen radicals produced by water vapor rf plasma," *IEEE Transactions on Plasma Science*, vol. 36, 1302–1303, 4 PART 1 2008.

[10] F. Herklotz, I. Chaplygin, E. V. Lavrov, and V. F. Agekyan, "Photoconductive detection of a hydrogen-related donor in sno2," *Applied Physics Letters*, vol. 114, 15 Apr. 2019.

[11] Z. Jakub *et al.*, "Partially dissociated water dimers at the water-hematite interface," *ACS Energy Letters*, vol. 4, 390–396, 2 2019.

[12] C. G. V. D. Walle, "Hydrogen as a cause of doping in zinc oxide," *Physical Review Letters*, vol. 85, 1012–1015, 5 2000.

[13] H. Yamada, Y. Ushimi, H. Kawamura, M. Takeuchi, Y. Yoshino, and T. Makino, "Effects of h2o partial pressure on the crystallinity of zno thin film and electrical characteristics of film bulk acoustic wave resonators," *Vacuum*, vol. 80, 814–817, 7 SPEC. ISS. 2006.

[14] B. K. Meyer, J. Sann, D. M. Hofmann, C. Neumann, and A. Zeuner, "Shallow donors and acceptors in zno," *Semiconductor Science and Technology*, vol. 20, 4 2005.

[15] D. C. Look, J. W. Hemsky, and J. R. Sizelove, "Residual native shallow donor in zno," *Physical Review Letters*, vol. 82, 2552–2555, 12 1999.

[16] I. Crupi, S. Boscarino, V. Strano, S. Mirabella, F. Simone, and A. Terrasi, "Optimization of zno:al/ag/zno:al structures for ultra-thin high-performance transparent conductive electrodes," *Thin Solid Films*, vol. 520, 2012.

[17] Z. Chen *et al.*, "A transparent electrode based on solution-processed zno for organic optoelectronic devices," *Nature Communications*, vol. 13, 2022.

[18] E. Moyen, J. Kim, J. Kim, and J. Jang, "Zno nanoparticles for quantum-dot-based light-emitting diodes," *ACS Applied Nano Materials*, vol. 3, 5203–5211, 2020.

[19] J. Chung, J. Lee, H. Kim, N. Jang, and J. Kim, "Effect of thickness of zno active layer on zno-tft's characteristics," *Thin Solid Films*, vol. 516, 5597–5601, 2008.

[20] J. Zhang, X. Li, J. Lu, P. Wu, J. Huang, Q. Wang, B. Lu, Y. Zhang, B. Zhao, and Z. Ye, "Evolution of electrical performance of zno-based thin-film transistors by low temperature annealing," *AIP Advances*, vol. 2, 2012.

[21] A. Berman, "Water vapor in vacuum systems," *Vacuum*, vol. 47, 327–332, 4 1996.

[22] K. Jousten, "Thermal outgassing," *CAS 2006 - CERN Accelerator School: Vacuum in Accelerators, Proceedings*, 87–116, 1 2007.

[23] R. Grinham and A. Chew, "A review of outgassing and methods for its reduction," *Applied Science and Convergence Technology*, vol. 26, 95–109, 5 2017.

[24] P. A. Redhead, "Modeling the pump-down of a reversibly adsorbed phase. i. monolayer and submonolayer initial coverage," *Journal of Vacuum Science and Technology A: Vacuum, Surfaces, and Films*, vol. 13, 467–475, 2 1995.

[25] P. A. Redhead, "Modeling the pump-down of a reversibly adsorbed phase. ii. multilayer coverage," *Journal of Vacuum Science and Technology A: Vacuum, Surfaces, and Films*, vol. 13, 2791–2796, 6 1995.

[26] C. Melton, "Cross sections and interpretation of dissociative attachment reactions producing oh, o, and h in h2o," *The Journal of Chemical Physics*, vol. 57, 4218–4225, 2003.

[27] M. Jiménez-Redondo, E. Carrasco, V. J. Herrero, and I. Tanarro, "Chemistry in glow discharges of h2/o2 mixtures: Diagnostics and modelling," *Plasma Sources Science and Technology*, vol. 24, 1–25, 1 2015.

[28] A. V. Bernatskiy, I. V. Kochetov, and V. N. Ochkin, "Transformations of neutral particles in the discharge plasma in inert gases with water vapor and deuterium," *Physics of Plasmas*, vol. 25, 8 Aug. 2018.

[29] A. V. Bernatskiy, V. V. Lagunov, V. N. Ochkin, and S. N. Tskhai, "Study of water molecule decomposition in plasma by diode laser spectroscopy and optical actinometry methods," *Laser Physics Letters*, vol. 13, 7 2016.

[30] B. Chapman, *Glow Discharge Processes. Sputtering and Plasma Etching*. Wiley Interscience, 1980.

Chapter 2

WATER VAPOR PLASMA IN MAGNETRON SPUTTERING DISCHARGES

2.1 Water vapor in low pressure deposition systems

The use of water vapor in low-pressure environments has often presented challenges in terms of process control. In vacuum systems, it can affect the operation of vacuum components, such as seals, metal surfaces, and the vacuum pump [1]. To fully utilize water vapor in low-pressure plasma processes, it is vital to establish a stable procedure to properly control the process parameters.

The main factor that makes the water vapor partial pressure difficult to control is its reactive and adsorptive behavior. The adsorption behavior is significant to discharge stability as it affects the system pressure. One of the most time-consuming parts of the process is the pumping down of the system to the high vacuum pressure range, which is delayed exponentially when water vapor is present. As shown in Fig. 2.1a, water vapor can adsorb onto the surface through either physisorption or chemisorption. Physisorption is typically a reversible process and has a lower desorption energy compared to chemisorption onto the surface. In the formation of multiple layers, physisorption often dominates. The energy range for water vapor desorption typically lies between 0.8 eV to 1.08 eV for surfaces typically used in vacuum systems such as stainless steel. This range makes the plasma process particularly difficult, as it is low enough to significantly affect multiple vacuum pressure stage operations used in deposition processes [1–3].

When these adsorbed species are considered with the presence of plasma, the analysis becomes much more difficult. As shown in Fig. 2.1b, the energetic particles incident on the chamber wall surface can interact with the adsorbed species. These can result in numerous surface processes, depending on the energy and the reactive behavior. At low energies, the adsorbed particle could be transported toward the bulk plasma or reabsorbed back on the surface. At higher energy, sputtering or shallow implantation onto the wall could occur. When reactive species are concerned, they can form compounds at the surface that act as a getter pumping phenomena [3–7].

Given these challenges, it is vital to ensure the stability of the introduction of water vapor as a reactive gas and investigate its behavior as a plasma for material modifications and synthesis. In this study, the introduction of water vapor from the water reservoir was explored in terms of its pressure, and the behavior as a plasma was investigated through Berg's reactive magnetron sputtering model. This chapter aims to realize the stable introduction of water vapor and identify the characteristic behavior based on an established model to highlight its difference compared with other gases.

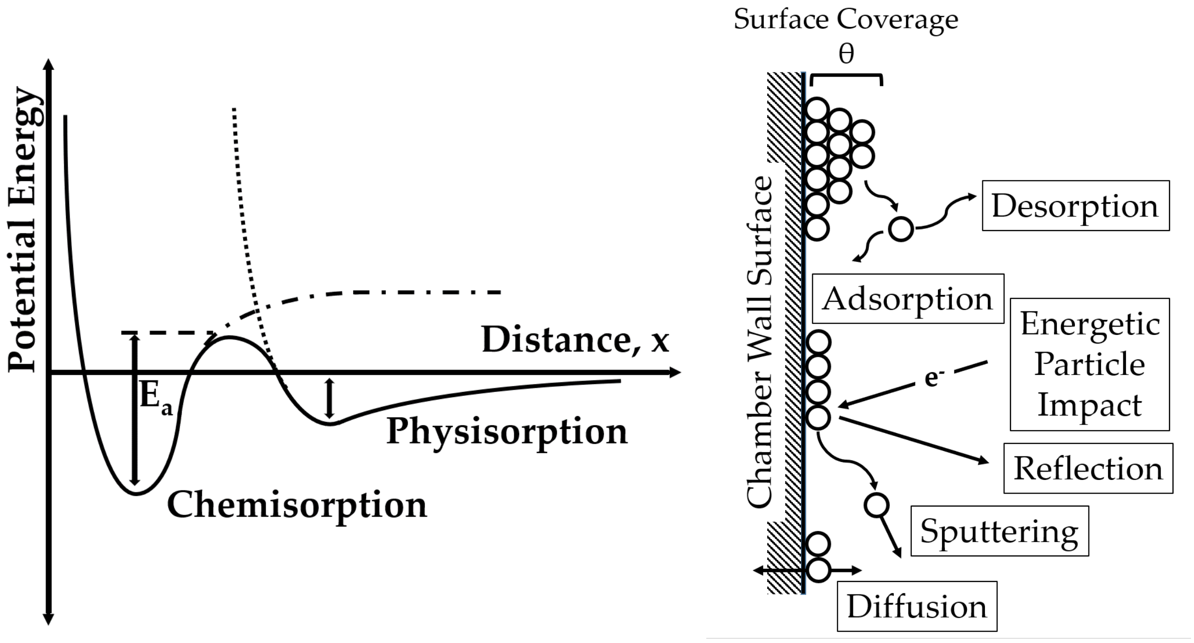

FIGURE 2.1: (*Left*) The Lennard Jones potential energy plot of a water vapor molecule at the surface at a specific distance, x, and (*right*) the possible chamber wall processes when adsorbed phases are present.

2.2 Experimental system

As shown in Fig. 2.2, the experiments to investigate the pressure change of water vapor plasma were carried out in an 84 mm diameter, 85.0 mm long SUS cylindrical system with a 70.0 mm diameter Zn (Nilaco, 99.2%) magnetron cathode. The cathode made of Al housed two concentric, toroidal NdFeB magnets that realized an unbalanced magnetron sputtering configuration. The pressure was maintained using a turbomolecular pump (Osaka Vacuum, TG50FVAB) and an oil rotary vacuum pump (ULVAC, GVD-100). The pressure was monitored using a crystal/cold cathode combination gauge (Tokyo Electronics, CC-10) and a digital data logger (Graphtec Corp., GL900). To ensure accurate pressure measurements, the gauge was directly calibrated to a capacitance manometer (ULVAC, CCMT-10A). The gauge entrance aperture was positioned perpendicularly 40 mm away from the axis of the magnetron cathode and was attached to a 90^o NW25 elbow to minimize deposition onto the gauge sensing elements. The center electrode of the CC-10 gauge was cleaned periodically to maintain the stability of the gauge readings. The base pressure was set in the 10^{-3} Pa range. The discharge support gas used was argon (Ar, 99.9999%)

The reactive magnetron sputtering discharge was maintained using a DC power supply (Takasago Co. Ltd., HV1.0-10). Arc suppression during discharge operation was achieved using a ballast resistor (1 kΩ, 400 W) and a choke inductor (11.2 mH). The discharge current and voltage were monitored directly through a voltage probe (Yokogawa Electric Corp., 700960, 1X) across the ballast resistor and a voltage probe (10X) monitoring the magnetron sputtering power supply, respectively. These data were recorded simultaneously together with the

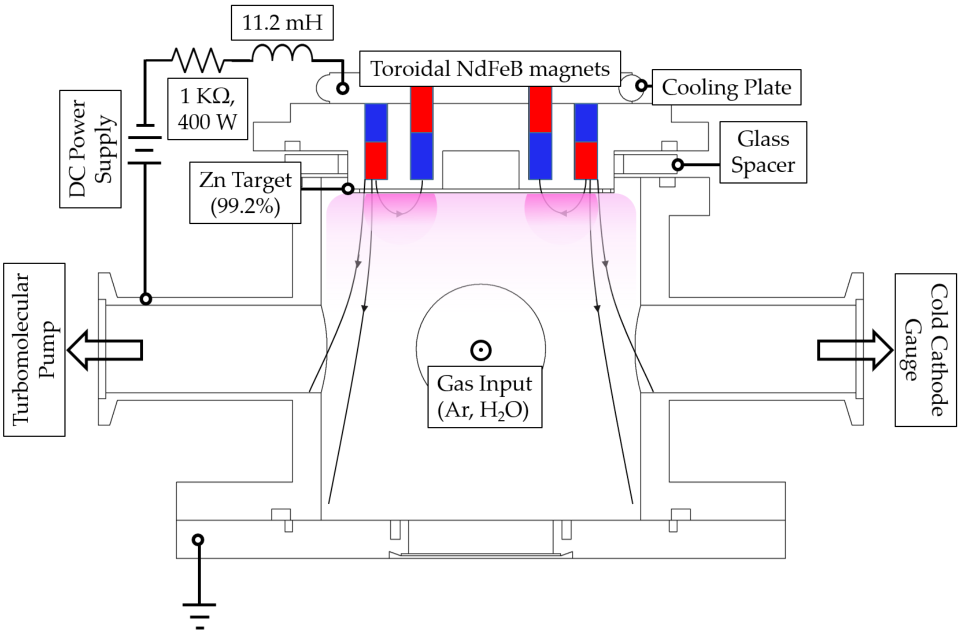

FIGURE 2.2: The reactive magnetron sputtering system. The magnetic field lines are shown to indicate an unbalanced magnetron configuration.

pressure using the digital data logger.

2.3 Water vapor reservoir

Shown in Fig. 2.3 is the vaporization-driven, heated water reservoir used throughout this study. This type of reservoir allows for the independent water vapor introduction as compared to a gas bubbler-type source where the water vapor content is dependent on the carrier gas flow [8, 9] and at a relatively simpler design. Distilled water (Nacalai Tesque, 14029-33) was the water vapor source. The primary flow control was realized using two flow-stop manual metering valves connected in series (Swagelok, SS-22RS4, and SS-4MG) with a quarter-turn valve (Swagelok, SS-42GS4). The series configuration, when opened at increasing increments with respect to the reservoir, realizes a gradual change in the pressure from the main chamber to the water's surface. This configuration minimized abrupt increase in the pressure in the main deposition chamber. The quarter valve also acts as a quick cut-off mechanism in case of the pressure spikes, such as those arising from hydraulic shock or flash evaporation from the water reservoir [10, 11]. Heating of the reservoir was accomplished using a ribbon band heater (Misumi, MRBH2) connected to a variable autotransformer (Yamabishi Co. Ltd., V-130-3), but was generally limited to below 70°C to maximize the elastomer seal lifetime present in the system. The temperature was monitored directly inside the reservoir with a K-type thermocouple (Misumi, SSM1.6-200) attached to the digital data logger

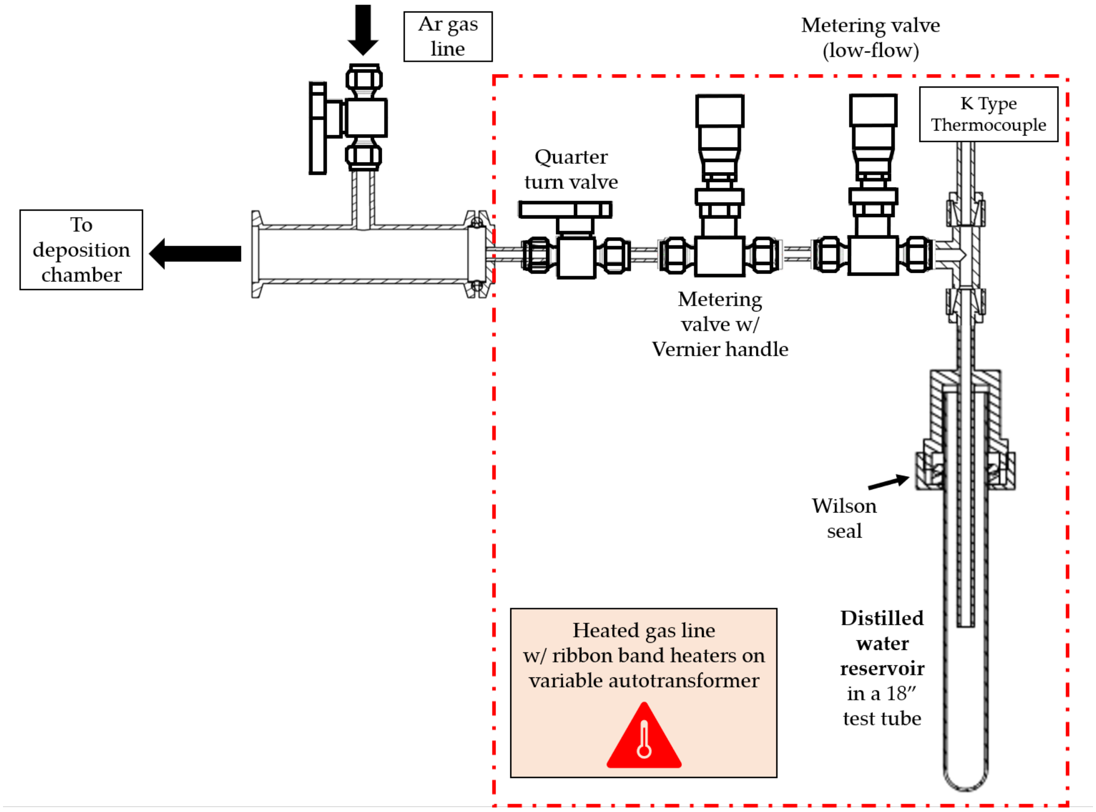

FIGURE 2.3: The vaporization-driven, heated water reservoir used in this study. The highlighted area in the red indicates the heated portions of the reservoir

2.3.1 Vaporization mechanism and gas flow

Precise flow control of the water vapor must first be realized to stabilize the water vapor pressure in the reactive magnetron sputtering system. The flow of water vapor was made difficult by water's adsorption behavior and its pressure-temperature dependent phase transitions [1, 2]. In the low-pressure regimes explored in this study, water mainly exists as a vapor, and the flow rate from its vaporization (G_{flow}) was described as shown in Eq. 2.1, assuming both molecular and viscous flow from a fixed aperture radius [12, 13]:

$$G_{flow} = K_o(\Delta p\sqrt{\frac{\pi N_A k_B T}{2M}}) \tag{2.1}$$

where K_o is a geometry factor that takes into account the effective aperture of the vaporization source, M is the molecular weight, N_A is Avogadro's constant, k_B is Boltzmann's constant, T is the temperature, and Δp is the pressure difference. From this equation, the stability of the flow is mainly dependent on the temperature and the aperture geometry as reflected with K_o. In this study, the reservoir aperture was fixed at 14.86 mm^2 near the liquid water surface and temperature control was used to modify the flow rate from the reservoir.

The change in the flow rate from the water reservoir can be quantified by examining the time-resolved pressure behavior of the system as the valves are opened. The pressure of the system behaves according to Eq. 2.2 by taking into consideration the mass balance of the introduction of gas and its removal by the pump:

$$\frac{dp}{dt} = \frac{k_B T}{\nu}(\frac{dn}{dt}) = \frac{k_B T}{\nu}(Q - \frac{pS}{k_B T}) \tag{2.2}$$

where $\frac{dp}{dt}$ is the change in pressure, ν is the volume of the magnetron sputtering system (~8.22x10^{-4} m^3), n is the number of gas molecules, Q is the gas flow rate, and S is the effective gas-dependent volumetric pumping speed [14, 15]. Assuming a constant Q and an initial pressure p_o at zero, solving this equation will yield the pressure of the system, $p(t)$, as shown in Eq. 2.3:

$$p(t) = p_{sat}(1 - e^{-\frac{t}{\tau}}) \tag{2.3}$$

where p_{sat} is the saturation pressure mainly dependent on Q and S, and a time constant τ (τ=$\frac{\nu}{S}$) [2, 5, 6]. The effective molecular gas flux (F_{sat}) into the system can be directly estimated from p_{sat} using Eq. 2.4:

$$F_{sat} = \frac{p(t)}{\sqrt{2\pi m k_B T}} \tag{2.4}$$

where m is the mass of the reactive gas molecule in this equation [15]. Comparing S and F_{sat} across different temperatures and with a reference non-adsorptive gas, such as Ar, the water vapor flow behavior from the water reservoir could be quantified.

2.3.2 Effect of temperature to flow control

Shown in Fig. 2.4 is the pressure curve of water vapor from the reservoir at varying temperatures. From both the opening and the closing of the valves, the pressure change directly observed was not as fast as that of Ar. The temperature also affects this change, as can be seen when comparing the 26^{o}C and 63^{o}C settings. This difference confirmed the temperature dependence seen in Eq. 2.1, and the relation was further quantified using the parameters F_{sat} and S obtained by fitting the curves to Eq. 2.3. Another important factor was linearity and the operational pressure range of the water reservoir with respect to the metering valve apertures. However, as the pressure change needs to be gradual to minimize spikes in the pressure, only the second metering valve aperture was varied. At around a 0.9 mm aperture opening, the pressure exponentially increased, and decreased slowly as the aperture opened further. This behavior limited the operational range of the water reservoir to the 0.1 Pa to 10 Pa range, as the time rate of change in pressure after opening might be too small to control effectively beyond this pressure range. The maximum pressure that can be stably controlled was measured to be 3.2 Pa, or in terms of water vapor flow rate, 0.614 SCCM.

The pressure curves for the introduction of water vapor were fitted to Eq. 2.3. The effective S normalized to a non-adsorbing gas, Ar, and the F_{sat} (Eq.2.4) obtained are shown in Fig. 2.5. The experiments were performed at two flow rates (0.0367 and 0.0725 SCCM measured without reservoir heating) such that the dependence upon the aperture size and the effect upon the pressure due to adsorption were accounted for. At the 0.0367 SCCM, S monotonically increased as the temperature increased. However, at 0.0725 SCCM, a sharp increase to a saturation value

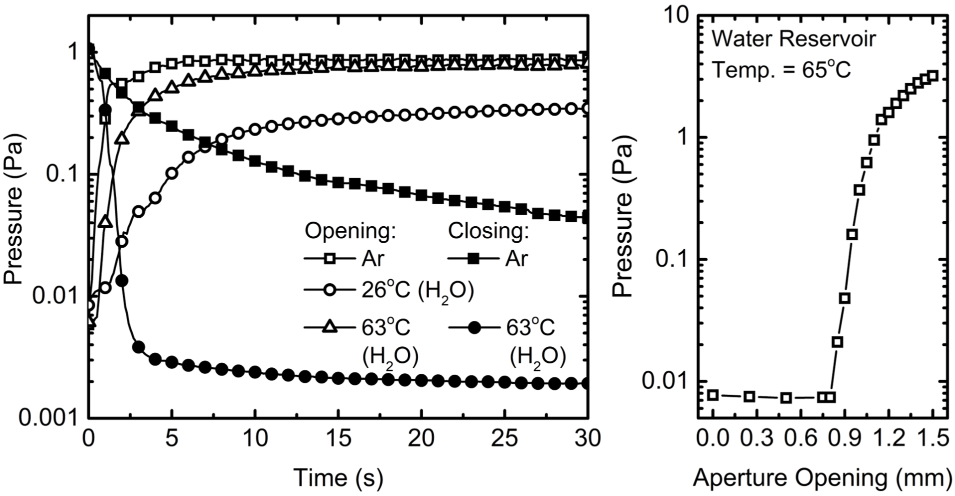

FIGURE 2.4: *(Left)* The effect of water reservoir heating temperature to the chamber pressure upon opening and closing of the water vapor reservoir, and *(Right)* the effect of the second metering valve aperture to the equilibrium pressure at a temperature of 65^{o}C. The temperature indicated is the water reservoir temperature.

was observed with a magnitude of around 2.2 to 2.5 times that of the lower flow rate setting. This shift indicated that the higher temperature allowed for a faster response of the reservoir to changes in pressure and that there was a maximum limit at a higher flow rate. The trend could be attributed to the release of more molecules from the surfaces along the water reservoir lines at higher temperatures [7] and its dominant adsorption mechanism. Fewer amounts of physisorbed species are present at the low flow rate setting because the coverage by the incoming flux becomes smaller at the lower pressure ranges. This change results in the lowered effective S and its gradual change as the temperature increases. However, at the higher flow rates, more physisorbed layers are present. Thus, as the temperature was increased, the dominant adsorption mechanism of water molecules to the surface could have shifted from physisorption to chemisorption as more of the adsorbed species were removed. As chemisorbed species are much harder to remove from the surface, this causes the observed saturating behavior at the higher temperatures observed at the 0.0725 SCCM flow rate setting[2, 16, 17]. The obtained F_{sat} value explains this observation, whereas the temperature increased, the increase in F_{sat} was faster at the higher flow rate.

The temperature effect was also seen in the vaporization flow rate, G_{flow}. Shown in Fig. 2.6 is the plot of the change in pressure with that of $T^{\frac{1}{2}}$. Considering the ratio of the flow rates and the changes in the effective aperture as the valves are opened, the fit of the line was taken. The slopes of the fit were relatively similar and differed only by 11.1% at the given temperature range. This dependence follows what is theoretically predicted by Eq. 2.6 at a fixed effective aperture size and emphasizes the importance of temperature control to realize higher flow rates and increased sensitivity with the water reservoir temperature. Thus, experiments were carried out at the higher end of the temperature range investigated (≈60 to 65^{o}C) for further experiments.

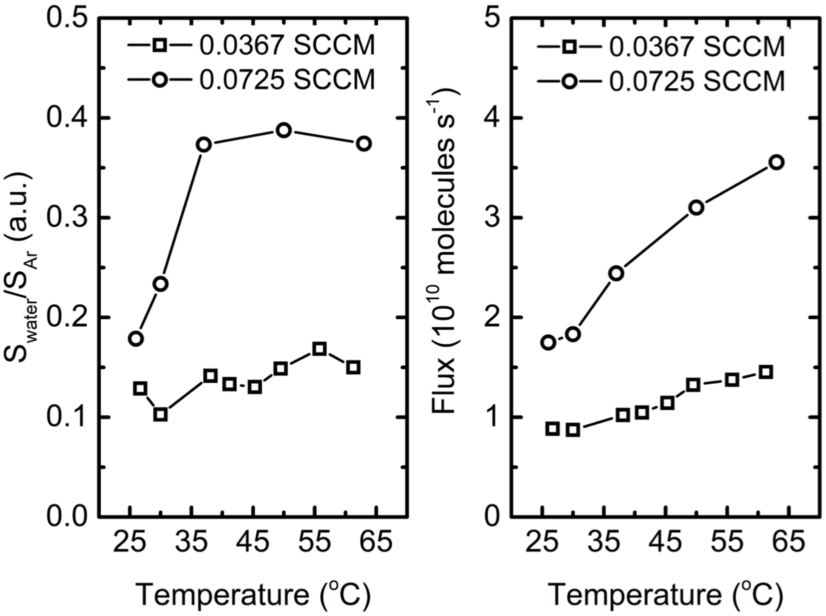

FIGURE 2.5: The effect of the water reservoir heating temperature to the effective pumping speed, *S (left)*, and the flux, F_{sat} *(right)*, at varying temperatures and flow rate

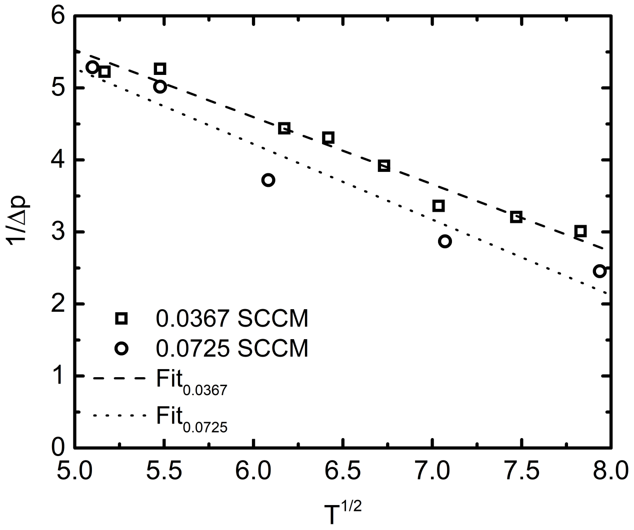

FIGURE 2.6: Fitting of $\frac{1}{\Delta p}$ against $T^{\frac{1}{2}}$ of the water reservoir at different flow rates

2.4 Simulation of Water Vapor Plasma in Reactive Magnetron Sputtering

After achieving the stable flow of water vapor, the next step is to investigate the plasma behavior. As a plasma, the behavior of the pressure in the system becomes a balance of multiple competing processes at different locations in the system. Particularly for reactive magnetron sputtering, nonlinear phenomena such as hysteresis of process parameters and discharge instabilities make the bulk process complicated. A numerical simulation model can explore multiple areas of the system simultaneously [15, 18–22]. One of the models that were developed for this is Berg's model, one of the fundamental models for reactive sputtering process[15, 20].

2.4.1 Berg's model for reactive magnetron sputtering

In this study, Berg's time-resolved model explained the pressure behavior of water vapor reactive magnetron sputtering. While it was considered as a basic model because it simplified some of the complex phenomena and the model assumed uniform sputtering and deposition profiles, it was capable of identifying key processing problems [15, 19].

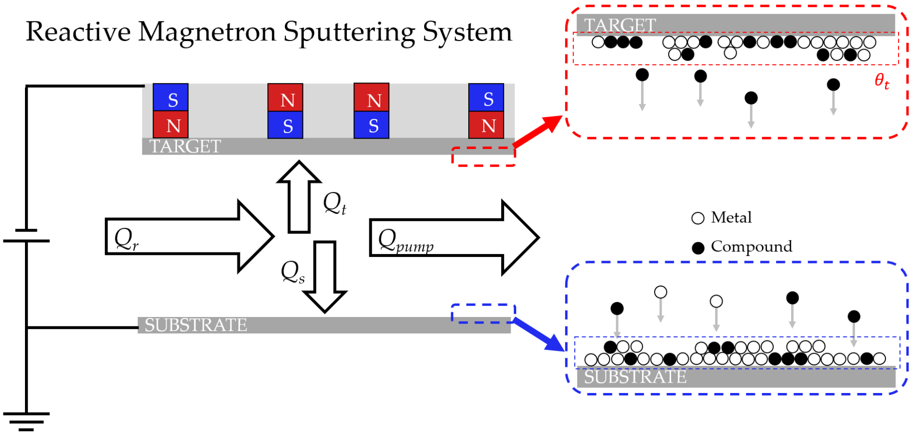

FIGURE 2.7: The surface processes considered in the time-resolved Berg's reactive sputtering model

Shown in Fig. 2.7 are the surface processes considered in time-resolved Berg's reactive magnetron sputtering model [15]. In this model, the pressure of the reactive magnetron sputtering system can be described as a flow of gas into the sputtering chamber. The change in pressure can be expressed as a modification of Eq. 2.2 and is defined as:

$$\frac{dp}{dt} = \frac{k_B T}{\nu}(Q_r - Q_t - Q_s - Q_{pump}) \tag{2.5}$$

where Q is the gas flow rate and the subscript denotes the region (Q_r: reactive gas flow, Q_s: flow to the substrate, Q_t:flow to the target, and $Q_{pump} = \frac{pS}{k_B T}$: flow due to vacuum pump removal). The values of Q_s and Q_t are determined using the following Eq.:

$$Q_t(t) = \alpha_t F_r(t)[1 - \theta_t(t)]A_t \tag{2.6}$$

$$Q_s(t) = \alpha_s F_r(t)[1 - \theta_s(t)]A_s \tag{2.7}$$

where α is the sticking probability of the reactive gas molecule to the surface at that region, F_r is the flux towards the surface as obtained from the kinetic theory of gases with a similar form to Eq. 2.4, θ is the compound coverage fraction at the surface, and A is the area of the region. In reactive magnetron sputtering, the formation of the compound determines the gettering of the reactive gas molecule as it interacts with the metallic particle [18]. The resulting flow by this phenomena is accounted for at the target and substrate surface by Eq. 2.6 and 2.7, respectively. Gettering is highly dependent on the amount of the oxide compound formed in the system as quantified by θ. At the target surface, this phenomenon is commonly referred to as target poisoning and has significant implications for the plasma process parameter hysteresis [15, 20]. The substrate area can be a measure of the uniformly deposited thin film composition that was assumed in this model. The change in θ_t is determined by:

$$n_s \frac{d\theta_t(t)}{dt} = \frac{2}{z}\alpha_t F_r(t)[1-\theta_t(t)] - J_{ion}Y_c\theta_t(t) \tag{2.8}$$

where n_s is the surface reaction site density, and z is the stoichiometric factor for the oxide, J_{ion} is the ion current density and Y_c is the sputtering yield of the oxide compound. The first term accounts for the flux-dependent formation of the compound at the metallic target surface, and this is dependent on the adsorption of a reactive gas molecule (α_t) onto a non-reacted portion of the target as described by 1-θ_t. The second term is the sputtering of the formed compound by the ion current J_{ion}. This term reduces the θ_t at the target surface, which exposes the underlying metal that can be used further as a reaction site in the first term. For the change in θ_s, it is then expressed as:

$$n_s \frac{d\theta_s(t)}{dt} = \frac{2}{z}\alpha_s F_r(t)[1-\theta_s(t)] + J_{ion}Y_c\theta_t(t)[1-\theta_s(t)]\frac{A_t}{A_s} - J_{ion}Y_m\theta_s(t)[1-\theta_t(t)]\frac{A_t}{A_s} \tag{2.9}$$

where Y_m is the sputtering yield of the metallic surface, and $\frac{A_t}{A_s}$ is the ratio of target to substrate area ratio ($\frac{A_t}{A_s}$= 0.159) . The first term also describes the flux-dependent formation from the target on the substrate region. The second and third terms correspond to contributions due to the deposition processes. By solving the equations simultaneously, Berg's model can be used to simulate the pressure behavior of the system when water vapor is used as the reactive gas and then can be fitted to experimentally time-dependent pressure plots to quantify the observed behavior.

2.4.2 Effect of adsorption-dependent parameters

The main parameters investigated in Berg's sputtering model are those highly affected by the adsorption behavior present with water vapor. Particularly, the effect of the sticking coefficient α_t and α_s, the sputtering yield ratio $\frac{Y_c}{Y_m}$, and the surface site density n_s in the form of $k(n_s)$ to account for possible multilayer formation on the surfaces. Shown in Fig. 2.8 are the effects of these parameters on the time-dependent change in pressure of the water vapor plasma.

The effect of the sticking coefficient, α, was dependent mainly on the region considered, while the magnitude determines how tightly a molecule will adhere to the surface. By varying the ratio of this parameter, we can determine its effect on the pressure plot. As seen in Fig. 2.8a, the target region affected the saturation pressure of the water vapor plasma, while the substrate region influenced the initial pressure drop immediately after discharge ignition. The difference indicated that the gettering phenomena from the consumption of the reactive gas

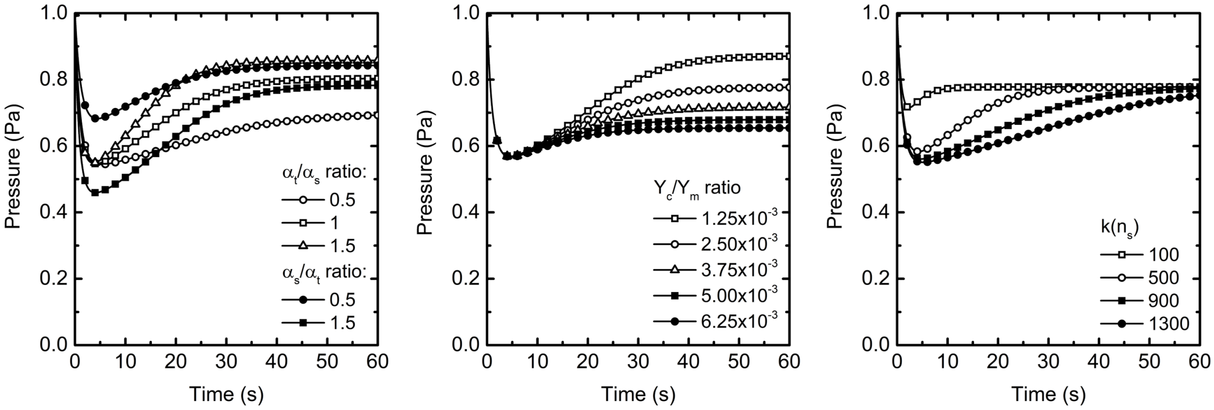

FIGURE 2.8: The effect of the α ratio, the $\frac{Y_c}{Y_m}$, and $k(n_s)$ to the pressure of the discharge for water vapor plasma. Unless specified, the typical settings were: α_t = 8x10^{-5}, α_s = 9x10^{-5}, Y_m = 1.0, Y_c = 2.5x10^{-3}, and k = 720. The discharge current (100 mA) and the working pressure (1.0 Pa) was kept throughout.

at the target surface and the saturation pressure were directly linked, while the pressure drop was correlated to the formation of the oxide at the substrate area. These phenomena supported the trend in sputtering yield ratio ($\frac{Y_c}{Y_m}$). While sputtering was accounted for at both Eqs. 2.8 and 2.9, the plasma was concentrated at the target surface, and the difference was directly accounted for by the ratio of $\frac{A_t}{A_s}$. This difference resulted in the decreased saturation pressure as more compound was formed at the target surface. On the other hand, the effect of $k(n_s)$ is much more complicated. Possible multilayer formation delays the stabilization of the pressure, which complicated the analysis of how the pressure behaves. As the equilibrium adsorption behavior of water vapor in the presence of plasma is unknown, it was difficult to assume the layer formation at the surfaces for the numerical simulation. Experimental time-resolved pressure measurements were required to elucidate this behavior.

2.5 Time-resolved pressure measurements

The pressure of the water vapor plasma was fitted to Berg's time-resolved reactive magnetron sputtering model by varying the three parameters investigated in Sec. 2.4.2. Specifically, the effect of common discharge parameters: the working pressure, the discharge current, and the use of a discharge support gas, argon (Ar), with the reactive gas in an admixture, were investigated. Shown in Fig. 2.9 is the typical fit of 1.0 Pa water vapor plasma pressure curves obtained from experiments to Berg's time-resolved reactive magnetron sputtering model. The effect of the discharge parameters was quantified through the model parameters and the predicted θ value.

The parameters in Berg's time-resolved magnetron sputtering model were obtained by fitting the experimental data with the model. The four parameters used were α_t, α_s, Y_c, and $k(n_s)$. The discharge current and working pressure were set initially depending on the discharge parameter investigated. At each given range for the parameter, the simulation datasets

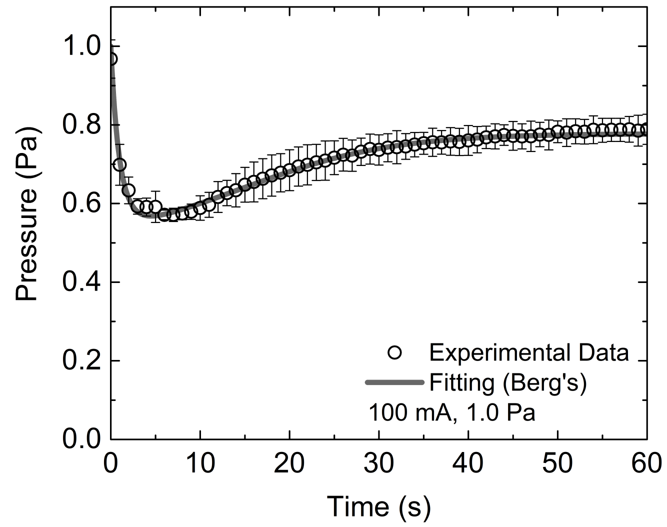

FIGURE 2.9: Fitting of the averaged pressure curves of 1.0 Pa H_2O plasma to Berg's time-resolved reactive magnetron sputtering model at 100 mA discharge current. The parameters obtained from fitting are: α_t = 8.0x10^{-5}, α_s = 9.0x10^{-5}, Y_c = 2.5x10^{-3}, $k(n_s)$ = 720 (χ^2= 1.63x10^{-4}).

were generated. The experimental data were fitted directly with the simulation dataset, and the model fit was selected and evaluated through χ^2 minimization.

2.5.1 Effect of working pressure

The effect of the working pressure on the discharge plasma was correlated directly to the flux of the reactive gas (Eq 2.4). At higher flux, more reactive gas were expected to contribute to the surface processes that lowers the discharge pressure. The effect expected was that the $k(n_s)$ would vary directly in this case, owing to multilayer formation. However, this was not the case, and no noticeable trend due to $k(n_s)$ was observed and appeared mainly affected by α and Y_c as shown in Fig. 2.10.

Initially, α_t and α_s showed an increasing trend as the pressure increased. However, after 1.1 Pa, the trend deviated. Meanwhile, Y_c consistently increased with increasing pressure. This non-linearity could be attributed to the increase in the effective areas that allow for more compound formation, such as reactive gas multilayer formation, but it is not necessarily uniform throughout the regions in the system. This non-uniformity also accounts for the lack of dependence upon $k(n_s)$ as it denotes a uniform increase in the effective area at all regions considered in the model.

In terms of the predicted compound coverage fraction, θ, increasing the working pressure lead to an increase in both θ_s and θ_t (Fig2.11). It was interesting to note that the θ_t observed was greater than 0.8 even for low working pressures. This magnitude indicated that target poisoning occurs significantly even at low pressures. θ_s also increases non-linearly and saturates to a value close to θ_t. This trend indicated that the working pressure controlled the oxide

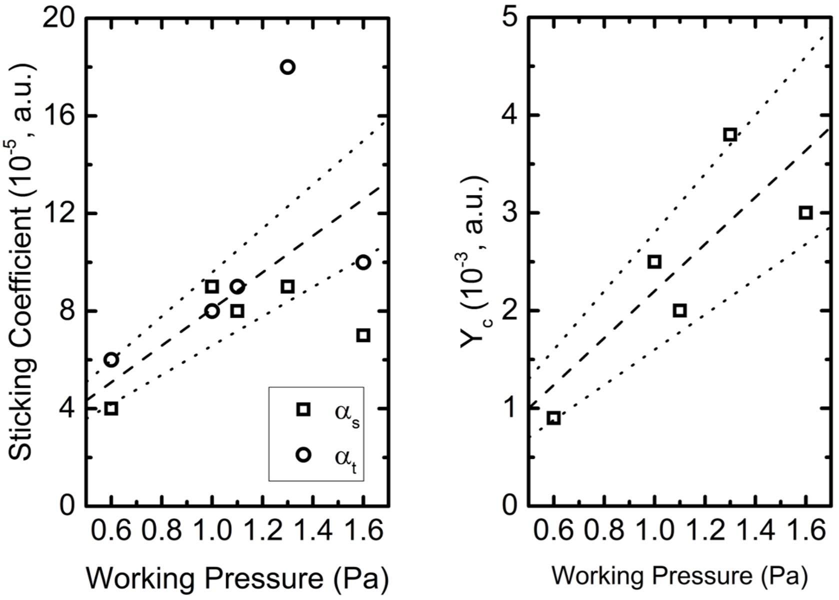

FIGURE 2.10: The effect of the water vapor working pressure to the sticking coefficient (α) at the target and substrate regions and the sputtering yield, Y_c. The dashed and the dotted lines are to guide the eyes.

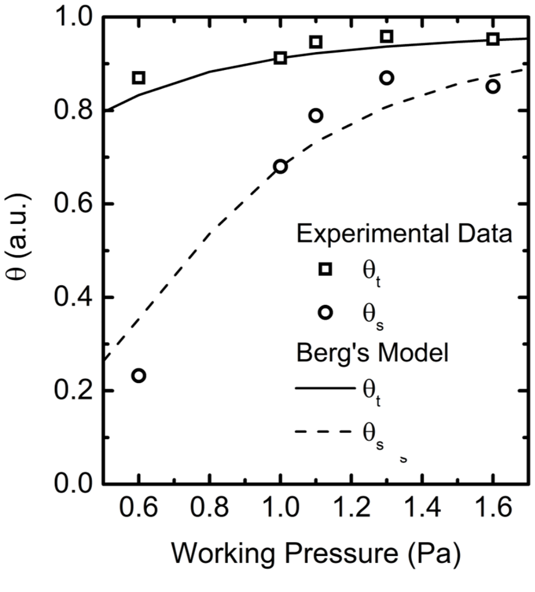

FIGURE 2.11: The effect of the water vapor working pressure to the compound fraction (θ) at the target and substrate regions as determined experimentally with the pressure curve fitted to Berg's model. The trend lines show what is theoretically predicted by varying the working pressure directly with the parameters used in Fig. 2.9.

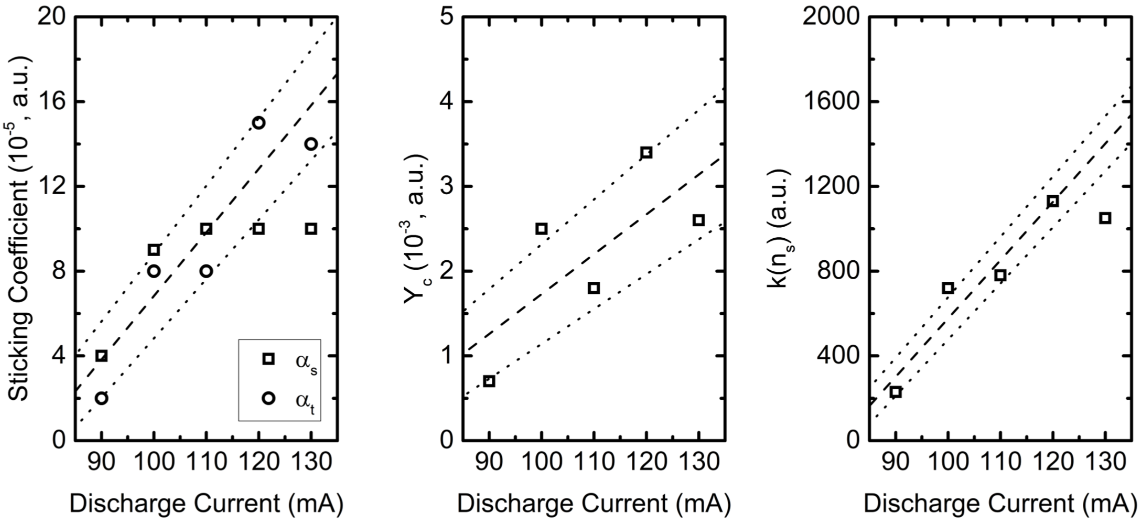

FIGURE 2.12: The effect of the water vapor plasma discharge current to the sticking coefficient (α) at the target and substrate regions, the sputtering yield, Y_c, and the surface site density $k(n_s)$. The dashed and the dotted lines are to guide the eyes.

compound formation, but it will be difficult to accomplish using the working pressure as small changes in the pressure region below 1.0 Pa lead to a disproportionately greater increase in θ_s.

2.5.2 Effect of discharge current

In conventional magnetron sputtering, the discharge current often leads to higher plasma density resulting in higher deposition rates. However, this is not necessarily the case when reactive plasma was utilized as the target composition strongly affected this parameter [23, 24]. Thus, it is important to consider this discharge parameter for water vapor plasma owing to its unique reactive behavior.

Shown in Fig. 2.12 is the effect of the discharge current on the adsorption-dependent parameters. The parameters, as compared to the working pressure, were found to increase at higher discharge currents. This behavior was attributed to a higher plasma density. The denser plasma was accounted for in the model by the higher Y_c, and this allowed for more surface reactions at both the substrate and target regions by a larger value of α and $k(n_S)$. These effects can be linked directly to the plasma density, as the discharge voltage was varied minimally across the discharge current range, as measured in the experiments (≈-331 V)

The predictions by the model, however, deviated from the experimental results during the formation of the oxide at the substrate surface as evidenced in the θ_s (Fig. 2.13). The model predicts a monotonically decreasing θ_s to account for possible resputtering at the substrate surface region. However, this is not the case, θ_s was significantly lower at 90 mA and was relatively constant at 100-130 mA (≈0.694). Meanwhile, θ_t for the range considered showed consistency between data obtained experimentally and predicted by the model. The trend indicated that the target poisoning phenomenon minimally varied against the change in discharge current.

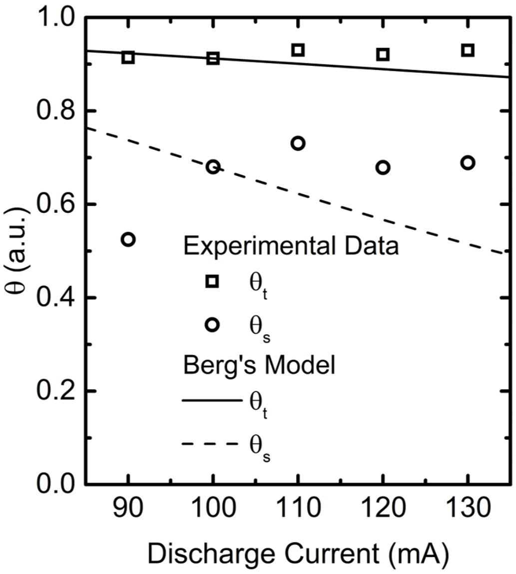

FIGURE 2.13: The effect of the discharge current to the compound fraction (θ) at the target and substrate regions as determined experimentally with the pressure curve fitted to Berg's model. The trend lines show what is theoretically predicted by varying the working pressure directly with the parameters used in Fig. 2.9.

The deviation of the experimental result for θ_s from the model results was then strongly linked with the substrate region. One probable mechanism is desorption due to energetic particle impact. The surface adsorbed species can be removed from the surface when a particle of sufficient energy, such as that from plasma, is incident upon it [4, 6]. As the plasma density at the target region is increased, a higher energetic particle flux towards the substrate could promote the desorption of the adsorbed reactive gas. This could then lead to a localized increase in ion density at the surface that contributes to the formation of the oxide. This is possible given the range of water vapor's adsorption energy for both physisorption and chemisorption. This can be differentiated from the resputtering effect, as the energy threshold is significantly greater for ZnO at 33-35 eV [25–27]

2.5.3 Effect of water vapor content

The addition of inert gas to magnetron sputtering allows for a larger degree of control over the thin film deposition process than using single-component, purely reactive gases. As the gas is inert, the deposition process becomes much more predictable, while the interaction of the inert gas with the film should be low. One of the commonly used gases in the process is argon (Ar). Argon is a relatively cheap inert gas with an atomic weight (39.948 amu) in the range that is ideal for sputtering. The sputtering yield of metals with incident inert ions is mainly dependent on the surface binding energy of the metal target and the ratio of the mass of the incident and metal atom [28]. From this, it may seem that it is beneficial if the ion is heavier, however, the glow discharge can be difficult to sustain if the inert gas is too heavy

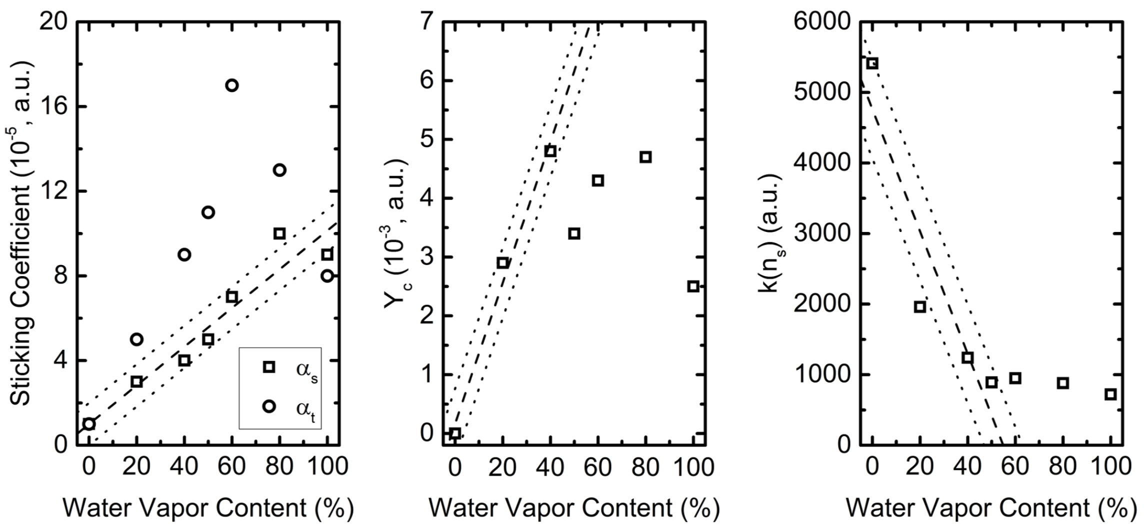

FIGURE 2.14: The effect of the water vapor plasma discharge current to the sticking coefficient (α) at the target and substrate regions, the sputtering yield, Y_c, and the surface site density $k(n_s)$. The dashed and the dotted lines are to guide the eyes.

because of the lower secondary electron coefficient at higher atomic numbers [29–31]. This behavior makes Ar an ideal candidate in the sputtering process.

Particularly for water vapor, The addition of Ar as an gas admixture enables the modification of the reactive and adsorptive behavior of the plasma as a whole. Shown in Fig. 2.14 are the parameters obtained from fitting with Berg's model. Interestingly, the α_s and α_t show varying trends. While both increased at higher water vapor content, α_t increased more rapidly than α_s. This difference was indicative that the adsorption at the target was stronger than at the substrate surface. This difference could be a consequence of a higher sputtering rate, where more fresh metal was exposed to act as a reaction site. However, the effect at the target surface is not directly linear with an increasing water vapor content. This change was supported by the non-linear variation in the Y_c, where Ar-H_2O gas admixtures had a higher Y_c than that of purely water vapor plasma, and the $k(n_s)$, which decreases to a saturation value from 60 to 100% settings. The high $k(n_s)$ measured at the 0% water vapor content could be attributed to the very low adsorption of the Ar gas [32], and was possibly reflected in the model as a large effective area.

The oxide formation at the surface was described by θ_s at higher water vapor content is much more predictable than the effect of the discharge current and the working pressure. Up to 60% water vapor content, the variation in θ_s is a direct linear dependence with the water vapor content (coefficient of determination, $r^2 = 0.98$). The values saturated to a value of θ_s=0.68 from 60% to 100% setting. On the other hand, the θ_t is significantly high even at low water vapor contents of 20%. This difference means that even at low water vapor content, the target poisoning phenomena still existed significantly. However, for the film deposition process, the strong linear dependence from 0 to 60% is promising in terms of controlling the discharge and

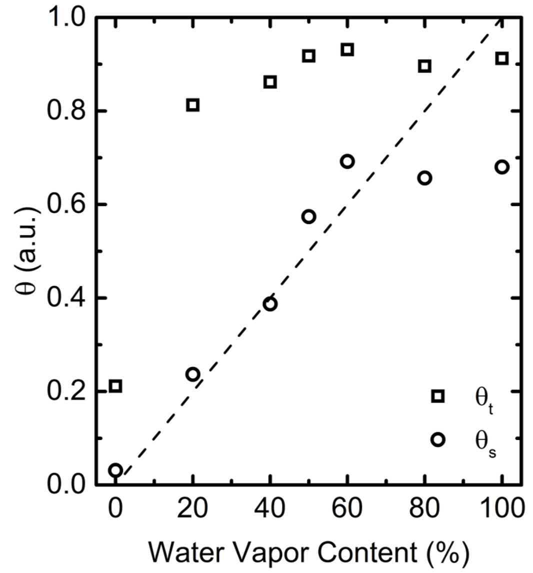

FIGURE 2.15: The effect of the gas admixture, Ar-H_2O, to the compound fraction (θ) at the target and substrate regions as determined experimentally with the pressure curve fitted to Berg's model. The dotted lines are to guide the eyes, and is proportional to a 1:1 correspondence of θ to the water vapor content.

the deposition process, as it allows us to tailor the film content estimated by θ_s primarily on the water vapor content alone.

2.6 Summary of Results

In this chapter, the stable flow of water vapor from a heated vaporization-driven reservoir was realized. Temperature control of the reservoir is a viable way to increase the responsiveness of the water vapor reservoir as a reactive gas source, particularly at higher flow rates where it has the most effect in terms of the effective pumping speed, S, and the flux, F_{sat}.

Berg's reactive magnetron sputtering model of water vapor plasma was explored in terms of the parameters expected to be highly influenced by the adsorption behavior of water vapor and the compound formation at both the target and the substrate surface. By fitting experimentally measured pressure curves with the time-resolved model, it was shown that the sticking coefficient, α, the compound sputtering yield, Y_c, and the surface site density, $k(n_s)$ significantly affected by the discharge parameters, such as the working pressure, the discharge current, and the gas admixture with an inert gas, Ar. Out of three discharge parameters, the gas admixture was the most suitable as θ_s varied linearly up to a 60% water vapor content.

References

[1] A. Berman, “Water vapor in vacuum systems,” *Vacuum*, vol. 47, 327–332, 4 1996.

[2] K. Jousten, “Thermal outgassing,” *CAS 2006 - CERN Accelerator School: Vacuum in Accelerators, Proceedings*, 87–116, 1 2007.

[3] R. Grinham and A. Chew, “A review of outgassing and methods for its reduction,” *Applied Science and Convergence Technology*, vol. 26, 95–109, 5 2017.

[4] H. Kojima, H. Sugai, and T. Okuda, “Discharge cleaning efficiency and behaviour of impurity gases,” *IEEJ Transactions on Fundamentals and Materials*, vol. 106, 557–564, 12 1986.

[5] M. Sefa, J. Šetina, and B. Erjavec, “A new method for determining water adsorption phenomena on metal surfaces in a vacuum,” *Materiali in Tehnologije*, vol. 48, 119–124, 1 2014.

[6] J. Huang, G. Liu, Z. Wang, L. Jiang, X. Yuan, Y. Liu, J. Deng, and Z. Yi, “High voltage breakdown induced by outgassing of space materials,” *AIP Advances*, vol. 5, 3 2015.

[7] A. V. Bernatskiy, V. N. Ochkin, and R. N. Bafoev, “The role of the heating of the vacuum chamber on the water content in plasma and gas,” *Journal of Physics: Conference Series*, vol. 747, 1 2016.

[8] A. Y. Nikiforov, A. Sarani, and C. Leys, “The influence of water vapor content on electrical and spectral properties of an atmospheric pressure plasma jet,” *Plasma Sources Science and Technology*, vol. 20, 1 Feb. 2011.

[9] T. Acsente, E. R. Ionita, C. Stancu, M. D. Ionita, G. Dinescu, and C. Grisolia, “Oes monitoring of sequential deposition of c/w layers by pecvd/magnetron sputtering techniques,” *Surface and Coatings Technology*, vol. 205, S402–S406, SUPPL. 2 2011.

[10] A. Mansour and N. Muller, “A review of flash evaporation phenomena and resulting shock waves,” *Experimental Thermal and Fluid Science*, vol. 107, 2019.

[11] L. Britton and R. Willey, “Avoiding water hammer and other hydraulic transients,” *Process Safety Progress*, 2023.

[12] G Burrows, “Evaporation at low pressures,” *Journal of Applied Chemistry*, vol. 7, 375–384, 1957.

[13] C. A. Ward and G. Fang, “Expression for predicting liquid evaporation flux: Statistical rate theory approach,” *Physical Review E - Statistical Physics, Plasmas, Fluids, and Related Interdisciplinary Topics*, vol. 59, 429–440, 1 1999.

[14] P. Chiggiato, “Vacuum technology for ion sources,” *CAS-CERN Accelerator School: Ion Sources - Proceedings*, 463–502, 2013.

[15] K. Strijckmans, R. Schelfhout, and D. Depla, “Tutorial: Hysteresis during the reactive magnetron sputtering process,” *Journal of Applied Physics*, vol. 124, 24 2018.

[16] P. A. Redhead, “Modeling the pump-down of a reversibly adsorbed phase. i. monolayer and submonolayer initial coverage,” *Journal of Vacuum Science and Technology A: Vacuum, Surfaces, and Films*, vol. 13, 467–475, 2 1995.

[17] P. A. Redhead, “Modeling the pump-down of a reversibly adsorbed phase. ii. multilayer coverage,” *Journal of Vacuum Science and Technology A: Vacuum, Surfaces, and Films*, vol. 13, 2791–2796, 6 1995.

[18] E. Kusano and D. M. Goulart, “Time-dependent simulation modelling of reactivesputtering,” *Thin Solid Films*, vol. 193-194, 84–91, 1 1990.

[19] S. Berg, T. Larsson, C. Nender, and H. O. Blom, “Predicting thin-film stoichiometry in reactive sputtering,” *Journal of Applied Physics*, vol. 63, 887–891, 3 1988.

[20] S. Berg and T. Nyberg, “Fundamental understanding and modeling of reactive sputtering processes,” *Thin Solid Films*, vol. 476, 215–230, 2 2005.

[21] W. D. Sproul, D. J. Christie, and D. C. Carter, “Control of reactive sputtering processes,” *Thin Solid Films*, vol. 491, 1–17, 1-2 2005.

[22] D. Depla, K. Strijckmans, A. Dulmaa, F. Cougnon, R. Dedoncker, R. Schelfhout, I. Schramm, F. Moens, and R. D. Gryse, “Modeling reactive magnetron sputtering: Opportunities and challenges,” *Thin Solid Films*, vol. 688, 137326, 2019.

[23] D. Depla, S. Mahieu, and R. D. Gryse, “Magnetron sputter deposition: Linking discharge voltage with target properties,” *Thin Solid Films*, vol. 517, 2825–2839, 9 2009.

[24] J. T. Gudmundsson, “Physics and technology of magnetron sputtering discharges,” *Plasma Sources Science and Technology*, vol. 29, 11 Nov. 2020.

[25] P. F. Carcia, R. S. McLean, M. H. Reilly, and G. Nunes, “Transparent zno thin-film transistor fabricated by rf magnetron sputtering,” *Applied Physics Letters*, vol. 82, 1117–1119, 7 2003.

[26] X. Zhang, Z. Pei, J. Gong, and C. Sun, “Investigation on the electrical properties and inhomogeneous distribution of zno:al thin films prepared by dc magnetron sputtering at low deposition temperature,” *Journal of Applied Physics*, vol. 101, 2007.

[27] A. Crovetto, T. Ottsen, E. Stamate, D. Kjaer, J. Schou, and O. Hansen, “On performance limitations and property correlations of al-doped zno deposited by radio-frequency sputtering,” *Journal of Physics D: Applied Physics*, vol. 49, 2007.

[28] Y. Yamamura and H. Tawara, “Energy dependence of ion-induced sputtering yields from monatomic solids at normal incidence,” *Atomic Data and Nuclear Data Tables*, vol. 62, 149–253, 2 1996.

[29] Y. Kusano, Z. barber, J. Evetts, and I. Hutchings, “Influence of inert gases on ionized magnetron plasma deposition of carbon nitride thin films,” *Surface and Coatings Technology*, vol. 174-175, 2003.

[30] Y. Sato, K. Ishihara, N. Oka, and Y. Shigesato, “Spatial distribution of electrical properties for al-doped zno films deposited by dc magnetron sputtering using various inert gases,” *Journal of Vacuum Science and Technology A*, vol. 28, 2010.

[31] G. West and P. Kelly, “Influence of inert gas species on the growth of silver and molybdenum films via a magnetron discharge,” *Surface and Coatings Technology*, vol. 206, 2011.

[32] M. Troy and J. Wightman, “Physisorption of ar, kr, ch4, and n2 on 304 stainless steel at very low pressures,” *Journal of Vacuum Science and Technology*, vol. 8, 1971.

Chapter 3

PLASMA SURFACE PROCESSES IN WATER VAPOR REACTIVE SPUTTERING

3.1 Introduction

The target surface in reactive magnetron sputtering is a key region that determines how the plasma behaves. The target surface processes, such as the formation of the reactive compound on the target surface, target poisoning, can significantly alter the effect of the discharge parameters to the plasma, which is known as hysteresis [1, 2]. These discharge parameters control the deposition process. Therefore, investigation of the target surface is needed, especially for unconventional chemically reactive gases such as water vapor.

As described in Chapter 2, the application of water vapor as a gas admixture with argon (Ar) showed potential for varying the formation of ZnO when water vapor plasma was used. In this chapter, the effect of the gas admixture on the target surface at the magnetron cathode was investigated experimentally.

3.2 Target Surface Characterization

The effect of the plasma on the magnetron target cathode can be determined through its surface composition and morphology. These two are of particular importance to the sputtering phenomena. Sputtering is defined to be the ejection of material from the surface due to the momentum transfer from an incident energetic particle, and the amount of atoms removed from the surface is defined as the sputtering yield [3]. The yield depends on the target material's heat of sublimation, atomic mass, and the incoming energetic particle's mass and energy [4]. In realistic scenarios such as magnetron sputtering, the sputtering process does not occur in a homogeneous way. The plasma is typically confined near a localized, high density region at the cathode surface, called the racetrack region [5]. This localization varies the angle of incidence of the energetic particle and, with the microscopic roughness of the film, can either increase or decrease the sputtering yield. The effective sputtering yield is then by the number of atoms that leave the surface and is dependent on the increase in sputtering from changes in the incidence angle, or its decrease as the removed material gets redeposited onto the target surface[6, 7]. This phenomenon also affects the ion energy distribution from the target and, together with the material itself, is a factor that determines the film formation process at the substrate region [8, 9]. These factors make the surface composition and morphology key characteristics when the target surface is investigated.

3.2.1 Target Composition using X-ray Diffraction

The target surface composition was investigated using X-ray diffraction (XRD). This technique utilizes X-ray radiation to probe the crystal's structure. On a crystalline surface, the incident X-rays diffract according to Bragg's law:

$$n_{ref}\lambda = 2d\sin(\theta_{xrd}) \tag{3.1}$$

where λ is the X-ray wavelength, n_{ref} is the order of the reflection, and θ_{xrd} is the angle of reflection. Given a fixed interatomic spacing, d, specific to the film's crystal structure, the characteristic peaks can be observed at certain values for $2\theta_{xrd}$ that correspond to a crystallographic structure and phase of the film or material [10, 11]. In this study, the XRD technique distinguished the oxide formed on the surface from the metal, specifically, ZnO on Zn.

3.2.2 Surface Morphology using Laser Microscopy

The surface morphology and roughness were measured using laser microscopy. Laser microscopy is a highly versatile technique that uses a laser as a confocal light source and a mirror to generate the image. The laser microscope can generate 3D reconstructions of the surface by scanning the area of interest and recording the axial position where the focus was maximized. The point was detected using a pinhole aperture in front of the detector, and the focal point was where the intensity of the light was maximum [12, 13]. This technique is advantageous for large, non-transparent samples, such as the target of the cathode. Multiple areas of interest are inspected simultaneously without requiring extensive sample preparation compared to scanning electron microscopy.

3.2.3 *In-situ* Laser Differential Reflectance Spectroscopy

The investigation of the surface while the plasma is present is desired, as it can be used to monitor changes on the target surface during the reactive magnetron sputtering process. However, this can be difficult to realize [14]. The cathode is at high negative voltages with high plasma density regions, which make electrostatic probe-based measurements in the vicinity of the surface difficult. The high density plasma could sufficiently damage the probe tip and form insulative films at the surface, and the applied bias can cause arc discharges between the target and the probe that can damage the measurement equipment. Optical emission spectroscopy (OES) could give us an insight, however, the changes in the target surface such as the surface composition or the roughness can be difficult to obtain directly.

In this study, the use of an *in-situ* technique, laser differential reflectance was explored. This method involves incident light onto a surface and measuring the reflected light to probe its characteristics. It has been used for surface roughness measurements [15] and *in-situ* film growth monitoring [16–18]. It has also been used for magnetron sputtering grown films [19–21]. The differential reflectance relies on the change in the reflectance and is expressed as:

$$\frac{\Delta R}{R} = \frac{I(E_\lambda, t) - I(E_\lambda, 0)}{I(E_\lambda, 0)} \tag{3.2}$$

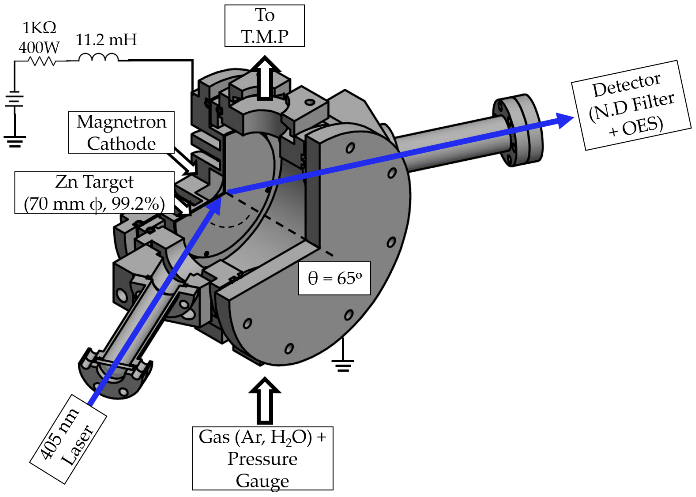

FIGURE 3.1: The reactive magnetron sputtering system with a differential reflectance spectroscopy setup. The setup was changed to realize a 65^o incidence angle for the 405 nm laser incident onto the target surface.

where R is the reflectance, $I(E_\lambda, t)$ is the intensity at a certain photon energy E, and at $t = 0$ is the initial state. By considering the initial state, the change in the surface can be estimated as a contribution from both the roughness and the surface composition. At oblique angles, the sensitivity can be increased to account for changes with the polarization of the incident and reflected light [15–18].

3.3 Experimental System

In this study, the magnetron sputtering system consisted of a similar experimental system to that in Chapter 2. As shown in Fig. 3.1, a compact, cylindrical system of 84.0 mm diameter and 60 mm length was used to realize the 65^o angle of incidence for the 405 nm laser that was incident onto the center of the magnetron target. The window used for the measurement was made of a replaceable Tempax® viewports, attached to a 75 mm length ConFlat flange nipple section to minimize deposition from the plasma and clean. The window was replaced in case the transparency was lost due to film deposition. The total path length from the between viewports was ≈ 325 mm. The pressure was maintained by a gas supply while pumping with a turbomolecular pump (Osaka Vacuum, TG50FVAB) and a rotary pump (ULVAC, GVD-100). A crystal/cold cathode gauge (Tokyo Electronics, CC-10) monitored the pressure throughout the experiment. The base and working pressure were set at 10^{-3} Pa and 1.0 Pa, respectively. The gas admixture consisted of Ar (99.9999%) and water vapor from the water reservoir. A DC power supply (Takasago Co. Ltd., HV1.0-10) sustained the discharge at a constant 100 mA discharge current.

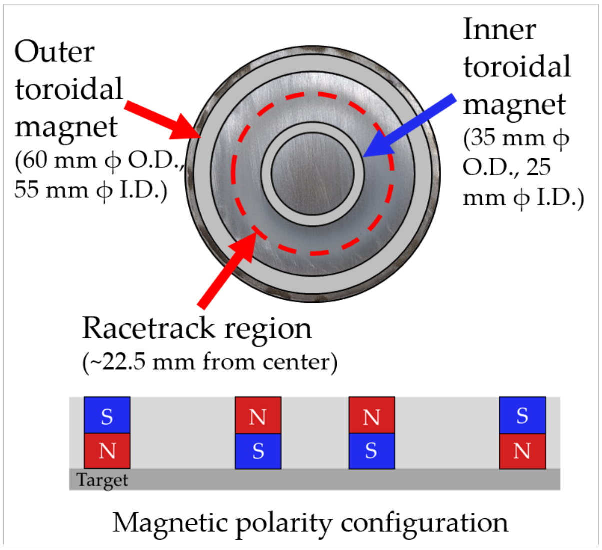

FIGURE 3.2: The cathode and the relative placement of the concentric toroidal magnets forming the magnetron sputtering cathode.

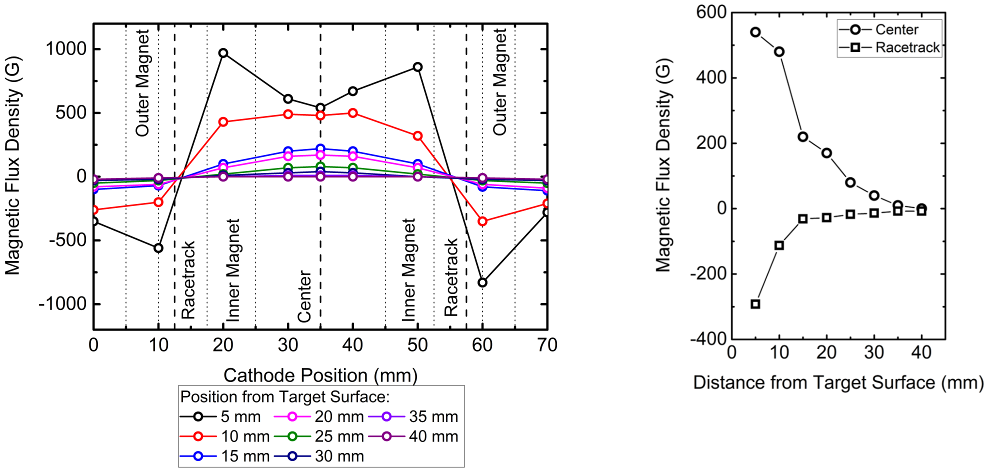

FIGURE 3.3: (Left) The magnetic flux density at different positions across the unbalanced magnetron cathode surface and (right) the magnetic flux density at varying distances from the target surface at the center and racetrack positions.

3.3.1 Target cathode configuration and Differential Reflectance Spectroscopy

The target cathode used in the study consisted of two concentric toroidal NdFeB magnets, and the relative position is shown in Fig. 3.2. The racetrack formed from this magnetic field geometry was ≈ 22.5 mm from the center of the target. The magnetic flux density was measured using a gaussmeter (Lake Shore, Model 421) with an axially oriented probe. The probe position was varied using a manual x-axis translation stage at different distances from the target surface. The concentric configuration realized an unbalanced magnetron configuration with its magnetic flux density distribution as shown in Fig. 3.3. The magnetic flux is minimized at 40 mm away from the target surface. At the racetrack region, the magnetic flux density is ≈ -300 G, while at the center, is at ≈ 540 G.

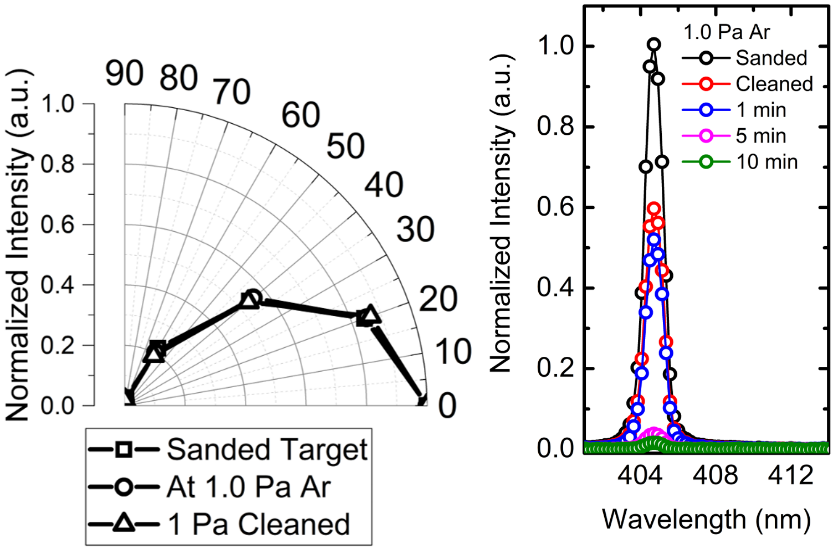

FIGURE 3.4: The intensity of the incident 405 nm laser at different polarization and the optical spectra of the reflected laser at different target conditions and 1.0 Pa Ar plasma duration

The differential reflectance spectroscopy was realized using a 405 nm laser (Lasever, LSR405NL - 100). This method typically utilizes multiple wavelengths, however, as the plasma produces time-dependent distinct peaks from excited species and positive ions, a 405 nm laser is used instead. The wavelength was selected to be as small as possible in the visible range to maximize the technique sensitivity and at a wavelength without a corresponding emission peak from probable excited species present in the plasma. Prior to measurements, the laser polarization was measured as described in Fig. 3.4a. Figure 3.4b described the peak shape and position of the incident laser. The polarization and the full width at half maximum (FWHM) were relatively constant (1.12 nm) across the settings observed. The position of the laser relative to the target surface was fixed at 0^o and parallel to the target surface to ensure a constant incident polarization at the 65^o angle of incidence. The target surface was prepared using 400 SiC paper at the same fixed parallel direction prior to attachment to the cathode surface to remove any native oxide formed and to control the initial surface roughness. The targets were cleaned using 1.0 Pa Ar for 1 minute to expose fresh metal on the surface and prevent the arc discharge formation commonly observed when a freshly prepared target was directly used for sustaining the magnetron discharge.

The reflected laser intensity was measured using a 1.8 OD neutral density filter and a USB spectrometer (Ocean Optics, USB4000). The neutral density filter prevented the oversaturation of the spectrometer detector while maintaining a laser current of 0.018-0.02A. The integration time of the spectrometer was 100 ms, averaged seven (7) times. The reflected laser intensity was measured at 1-minute intervals for a duration of 10 minutes.

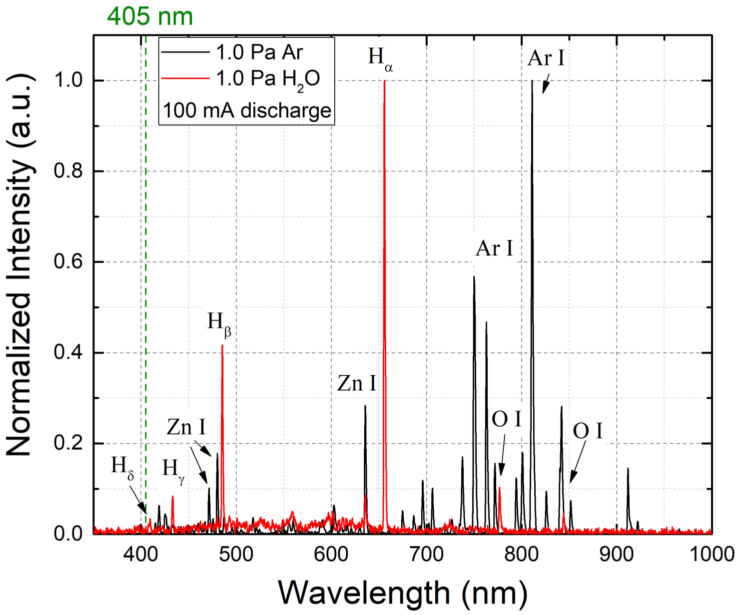

FIGURE 3.5: The optical emission spectra of the magnetron sputtering discharge at 1.0 Pa Ar and 1.0 Pa water vapor. The discharge current is at 100 mA. The peaks from the discharge support gas, Ar, the reactive gas, water vapor, and the Zn metal are indicated. The peak position for the 405 nm laser is indicated.

3.3.2 Surface Composition and Morphology

The surface morphology and composition were evaluated using X-ray diffraction and laser microscopy. The X-ray diffraction was carried out at a Bragg-Brentano configuration (PANalytical Xpert-Pro Line Scan, Cu K_α = 1.540598 Å, Scan Range: 10 - 90^o, Scan step: 0.1^o) with a PIXcel detector. The laser microscope (Keyence, VK-X210) measured the profile in a 1000x1000 μm area. Tilt correction for the sample profile was performed prior to any roughness measurement. The areas investigated were the center and the racetrack region for the composition and morphology.

3.4 Results and Discussion

Shown in Fig. 3.5 are the optical emission spectra of 1.0 Pa Ar and 1.0 Pa water vapor at a discharge current of 100 mA. From the plot, it was observed that there were no distinct high-intensity peaks located at the 405 nm position. This characteristic allows us to use the 405 nm laser wavelength for the differential reflectance measurement and confirmed the introduction of water vapor plasma into the discharge. The peaks that show the dissociation of water vapor are H_α at 656 nm and the O I peak at 777 nm and 844 nm. The presence of the Zn metal peak is also confirmed, with its most intense peak at 636 nm. The characteristic peaks of Ar I are also present, and the most intense peak intensity measured was at 811 nm [22].

Shown in Fig. 3.6 are the images of the prepared Zn metal targets after use in a reactive magnetron sputtering discharge for a 10-minute duration. For the targets exposed to a low

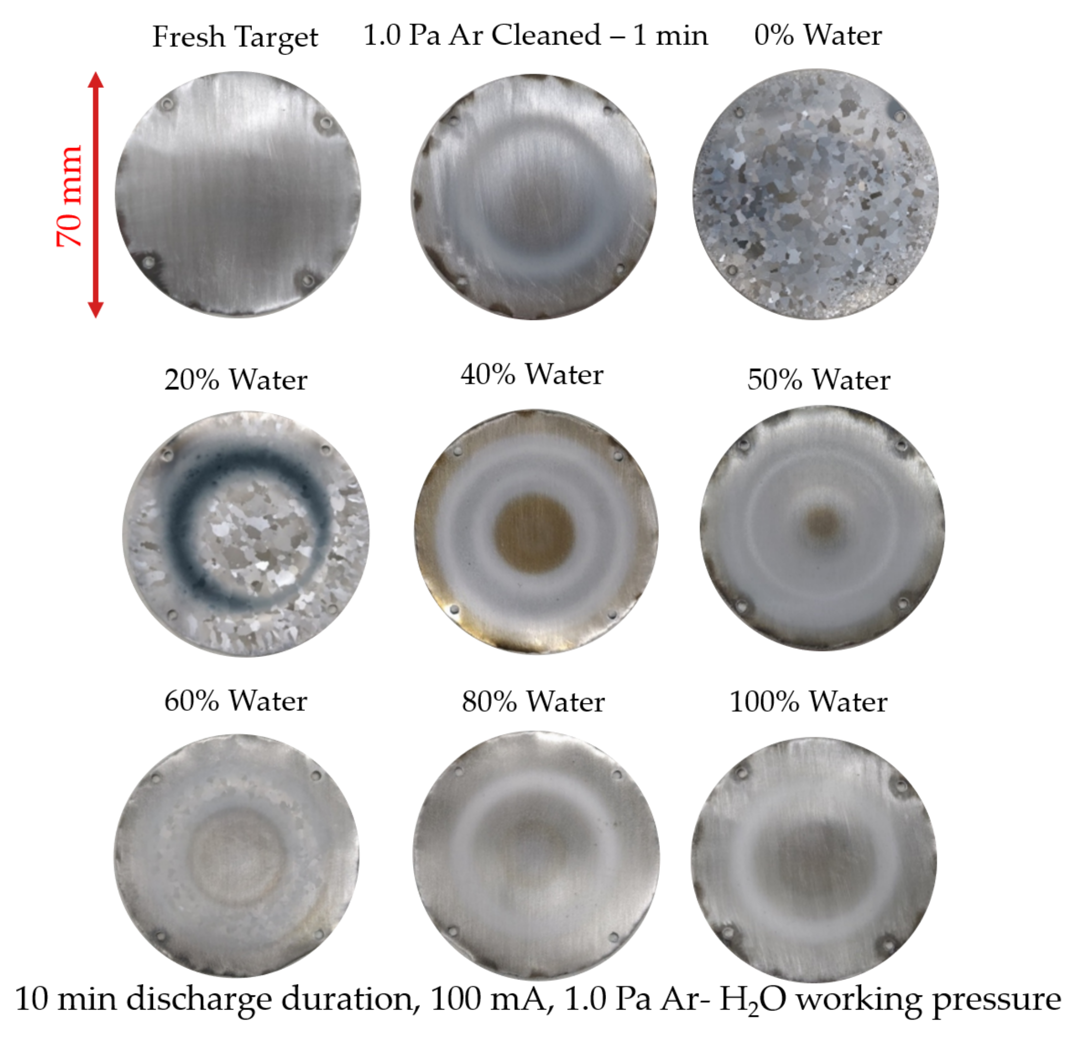

FIGURE 3.6: The 70.0 mm Zn metal target surface images at different instances: after SiC cleaning, after 1.0 Pa Ar cleaning, and after 10 minutes of reactive magnetron sputtering at varying water vapor content.

water vapor content plasma, at the 0% and 20% settings, the presence of an inhomogeneous, textured morphology was observed. This feature is less visible at the 40% settings and higher, where only the distinct discoloration at the center and racetrack can be directly distinguished. The difference between the racetrack and the center region is expected. In a magnetron configuration, the electrons are confined in cyclic trajectories by the magnetic field and repelled from the collection at the target surface towards a localized region near the racetrack by the highly negative bias at the cathode. This extended path length leads to a higher plasma density at the racetrack region [3] This phenomenon increased the sputtering of the target at the racetrack region and subsequently, the target poisoning if a reactive gas was present, as more fresh target material was exposed and the formation of the oxide at the surface is promoted. The complex trajectories from the sputtering process can then lead to the redeposition of material at the target itself. The discoloration at the center region was attributed to this redeposition phenomenon [7, 23, 24].

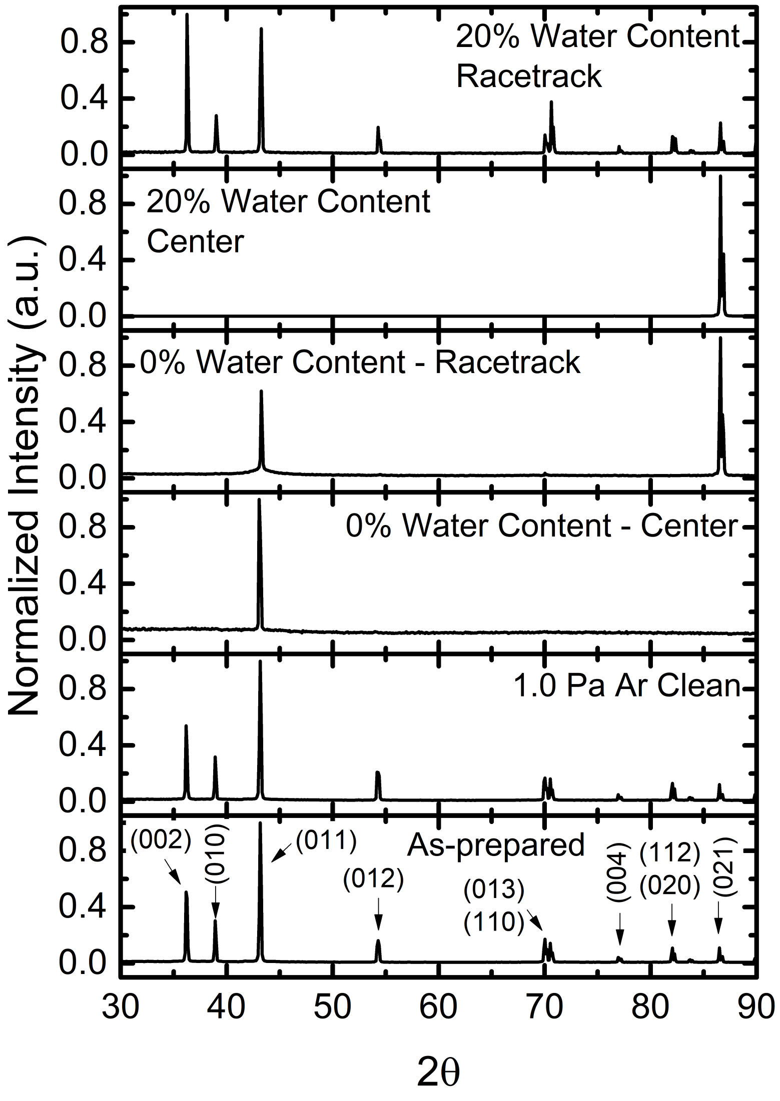

FIGURE 3.7: The target surface composition at the center and racetrack region of the as-prepared, cleaned, 0% and 20% water vapor content settings as measured by X-ray diffraction.

3.4.1 Target Composition

The visual observations were confirmed using the XRD measurements. Shown in Fig. 3.7 are the XRD results for the as-prepared sample, cleaned target, and the targets treated with low water content settings (0% and 20%). In the as-prepared and cleaned target samples, the (002), (010), (011), (012), (013), (110), (004), (112), (020), and (021) peaks for Zn metal were seen. Comparing the settings, the absence of multiple peaks at the plasma-exposed targets in comparison to the cleaned and as-prepared targets was observed. Sharper and more intense peaks corresponding to the (011) and (021) plane of Zn appeared at 43^o and 86.5^o, respectively, for the 0% and 20% water vapor content settings at both the center and racetrack. This observation indicated the formation of a layer of redeposited material at both regions, with a preferred

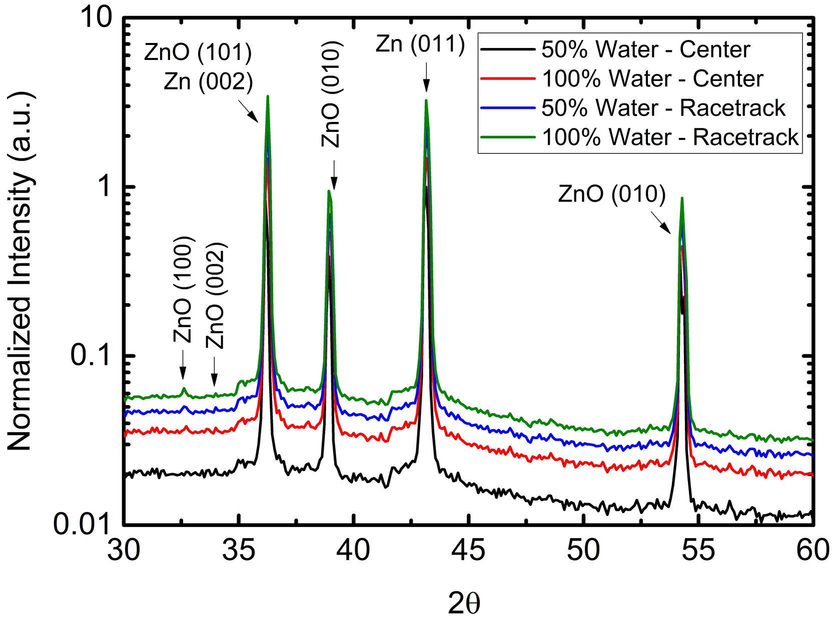

FIGURE 3.8: The target surface composition at the center and racetrack region for the 50% and 100% water vapor content as measured by X-ray diffraction and indicating the formation of the ZnO at the target surface through the (100) and (002) peaks.

crystallographic orientation different from that of the as-prepared and cleaned samples. The difference in the peak position between the 0% and 20% settings at the center position can be attributed to the difference in the mean ion energy of the plasma near the cathode surface. The addition of water affected the ionization of the discharge support gas and, at low water vapor content, could increase the ionization and density of the plasma. Water vapor has a lower ionization energy of 12.59 eV as compared to Ar at 15.7 eV. The water molecule can also dissociate into H, OH, and O ions [25, 26], as supported by the OES (Fig. 3.5). At sufficiently low water vapor partial pressures, this difference could increase the plasma ion density. However, when a higher water vapor content was used, the redeposition of the metal was sufficiently decreased because the overlayer of reactive gas and the compound formation could decrease the sputtering yield as compared to the lower reactive gas settings [27, 28].

The oxide formation on the surface was directly observed at the higher water vapor content settings, as shown in Fig. 3.8. The peaks for (100) and (002) corresponding only to ZnO were observed at 32^o and 34^o, respectively. However, peak intensities were faint compared to the (101) peak at 36^o. This peak can also indicate the (002) Zn peak, thus, the relative intensity ratio at $2\theta = 36^o$ and that of a high-intensity Zn peak at $2\theta = 43^o$ was used to indicate the amount of oxide present on the target surface.

Shown in Fig. 3.9 is the variation of this ratio with increasing water vapor content at the center and racetrack regions. At higher water vapor content, the ratio trends towards higher ratios at the racetrack and the center regions. Particularly, the ratio linearly increased until the 50% setting (Coefficient of determination, $r^2 = 0.98$) and was shifted downwards from the 60% water vapor content and greater. This trend was closer to the behavior observed at the

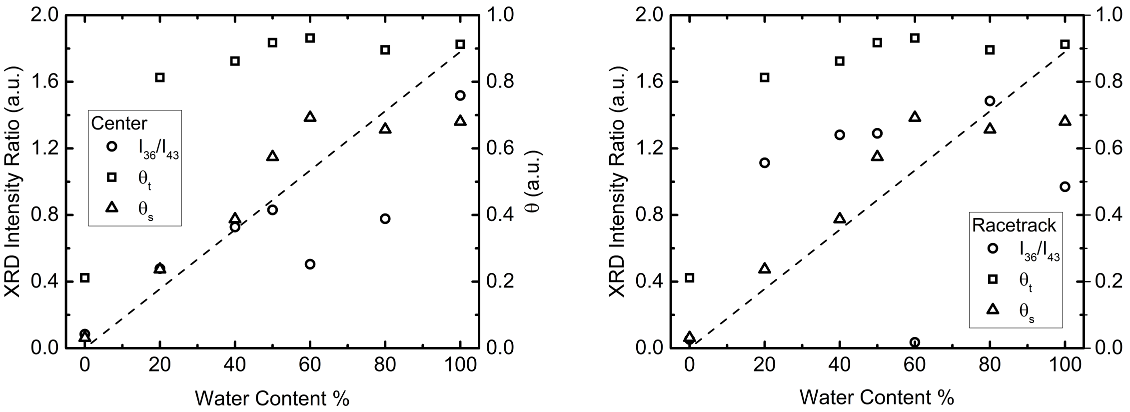

FIGURE 3.9: The ratio of the XRD peak intensity at $2\theta = 36^o$ and 43^o at increasing water vapor content. The ratio is compared with the compound target fraction at the target, θ_t, and at the substrate, θ_s, obtained from fitting discharge pressure curves to Berg's time-resolved reactive magnetron sputtering model. The dashed lines are to guide the eyes

substrate region, θ_s, than that of θ_t, which predicted that even at low water vapor content the target poisoning would be significantly present. The initial linear behavior upon adding Ar can be attributed to increasing amounts of ZnO formation at the target as more water vapor was present. However, this trend changed when the water content was sufficiently high at the 60% setting and above. The oxide formation would decrease the effective target sputtering yield leading to less Zn metal at the surface. As more oxide was sputtered compared to the metal which could subsequently redeposit on the target surface, it could lead to more ZnO at the region. This phenomenon would result in the nonlinear intensity ratio behavior at the 60% setting and greater.

On the other hand, the ratio was generally higher at the racetrack region than at the center region. It does not follow any linear trend at the 0% to 100% settings. The measured ratios indicate that the high plasma density significantly affects both sputtering and redeposition, and the sputtering rate varied substantially compared with the center region.

3.4.2 Surface Morphology

Shown in Fig. 3.10 are the laser microscope images at the center and racetrack region from 0% to 50% and at 100% water vapor content settings. At the 0% and 20% water vapor settings, the characteristic finish from the 400 SiC cleaning step was not as visible at the center and racetrack region as compared to the higher water vapor content settings. This change could be redeposited material that contained the preferential direction as observed in Fig. 3.7. Particularly in the racetrack region, the sputtering removal of the material was directly observed. This phenomenon was indicated by the small pits and rough textured morphologies at the 0 to 40% water vapor content. The formation of this textured material, however, visibly decreased as the water vapor content increased, as seen in the 50% and 100% settings. The presence of the small pits was enhanced as well, particularly for the 100% setting.

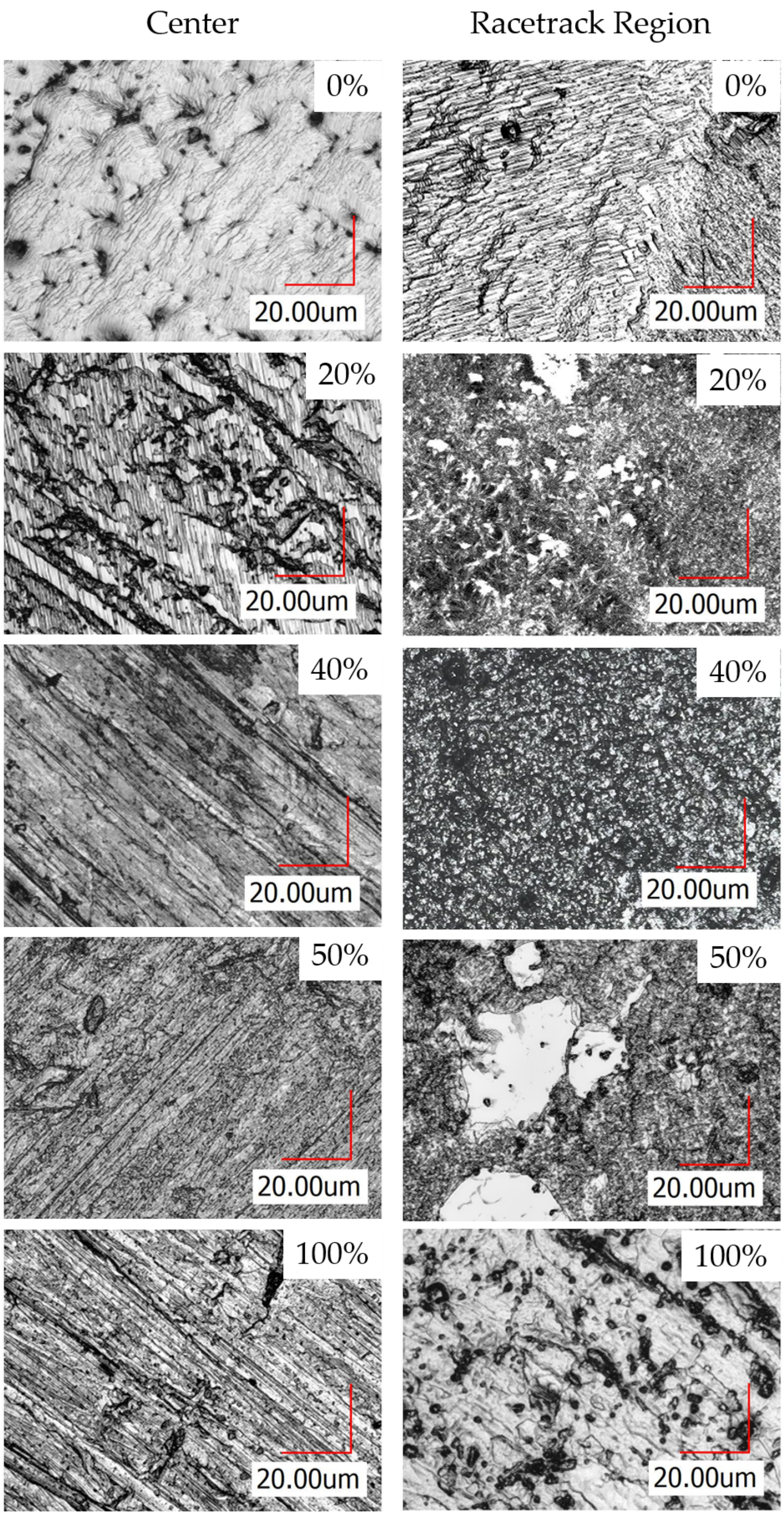

FIGURE 3.10: Target surface images under a laser microscope at varying water vapor content, at the center and the racetrack region

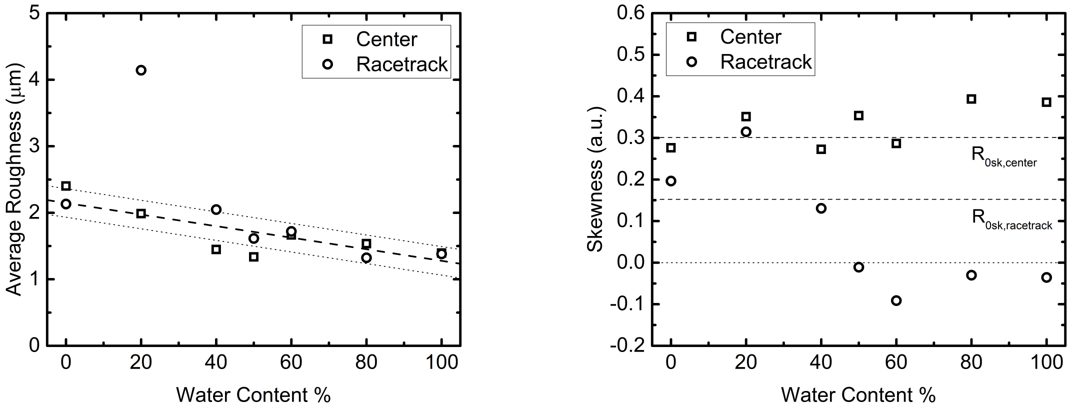

FIGURE 3.11: The effect of the water vapor content to the R_a and R_{sk} of the center and racetrack regions at an increasing water vapor content. The dashed lines are there to guide the eyes and highlight the change in the measured parameters.

To quantify the surface morphology changes, the roughness was evaluated using the average roughness, R_a, and the skewness, R_{sk}. The skewness is a parameter that describes whether the roughness was asymmetrically distributed towards values higher or lower than the R_a [29], which can indicate if there are pits or sharp peaks at the surface. Shown in Fig. 3.11 are R_a and R_{sk} at the center and racetrack regions.

The R_a decreased as the water vapor content increased. This trend occurred for both the center and racetrack regions. As shown in Fig. 3.11a, the R_a decreased to around 1.3 to 1.5 μm, which was close to the initial R_a from the initial surface preparation steps. However, comparing the center and the racetrack, it is interesting to note that a sharper decrease of R_a and larger magnitude at the 20% to 60% setting range at the racetrack was observed, especially with the sharp spike seen at the 20% setting. To explain this, the trend for R_{sk} was examined. The R_{sk} trend was distinctly different compared to R_a and was region dependent. At the center, R_{sk} remained relatively close to the initial value ($R_{sk}\approx$ 0.3) and was nearly constant at a positive value which denotes the presence of more peaks. However, at the racetrack region, R_{sk} decreased at the 20% to 60% settings and reached a negative value at the 50% to 100% water content settings. This decrease was indicative of the formation of more pitting at the higher water vapor content, which was observed in the laser microscope images in Fig. 3.10. Taking these into consideration, the formation of the redeposited material based on the morphology was favored at the center, while it is the erosion by the sputtering at the racetrack. The sputtering process is highly dependent on the roughness of the target, and as the surface roughness increases due to sputtering by the plasma at the racetrack, the formation of multiple off-normal facets on the target surface could result in the increased redeposition at the center of the target [7, 23]. This redeposited layer is easily seen in Fig. 3.10, particularly at the 0% water vapor content. This phenomenon also explained the presence of the sharp spike in R_a at the 20% water vapor content for the racetrack region. Adding the water vapor reactive gas sufficiently decreased the sputtering yield such that the redeposition was strongly minimized at the racetrack and occurred mainly at the center region. This change in the behavior was supported by

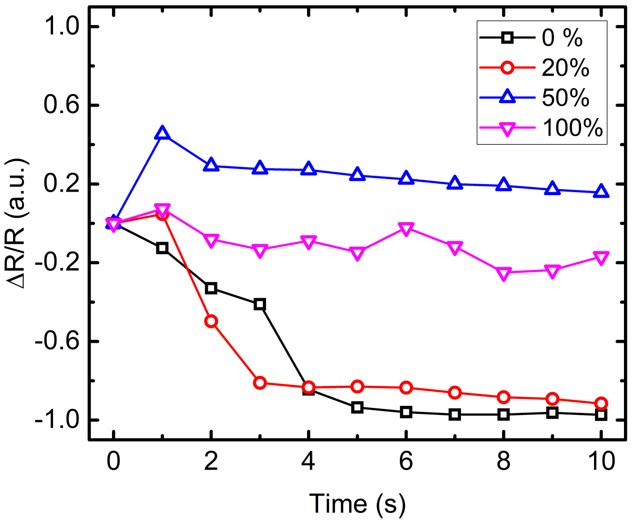

FIGURE 3.12: The differential reflectance of the 0%, 20%, 50% and 100% water vapor content settings against the discharge duration, at 1 minute intervals, for a total duration of 10 minutes.

the distinct difference in peak positions observed at the 20% setting as shown in Fig. 3.7.

3.4.3 Laser Differential Reflectance Spectroscopy

The *in-situ* characterization of the target using laser differential reflectance was proposed to determine the changes in the target surface condition during the deposition process. Shown in Fig. 3.12 is the differential reflectance of the Zn target against the duration of the plasma exposure. It was observed directly that the duration and water vapor content strongly affected the measured differential reflectance. Compared to the initial state, the magnitude of the decrease in reflectance was greater at low water vapor content. This behavior indicates a faster rate of change at the target surface by the plasma at low reactive gas settings.

To further elucidate the behavior at the surface upon reactive plasma exposure, the differential reflectance was plotted against the water vapor content, as shown in Fig. 3.13a. At 1 minute, the reflectance varied widely with the water content. However, as the duration further increased, the trend increased and saturated starting from the 50% water vapor content setting. In terms of the magnitude, the differential reflectance generally decreased as the duration of plasma exposure increased. This decrease and the trend in Fig. 3.12 could indicate that significant changes in the surface could occur as early as three minutes after running the discharge and can be used to estimate the surface condition of the target. However, while the decrease in the differential reflectance coincides with that of R_a, distinguishing the contribution of the surface composition and morphology to the differential reflectance was difficult as the formation of the oxide compound at the target surface is strongly linked with the surface roughness as established by the composition and surface morphology measurements.

It is also interesting to note the difference of the technique with that of OES. As shown in Fig. 3.13b, the trend seen with the differential reflectance was not observed. The increase in

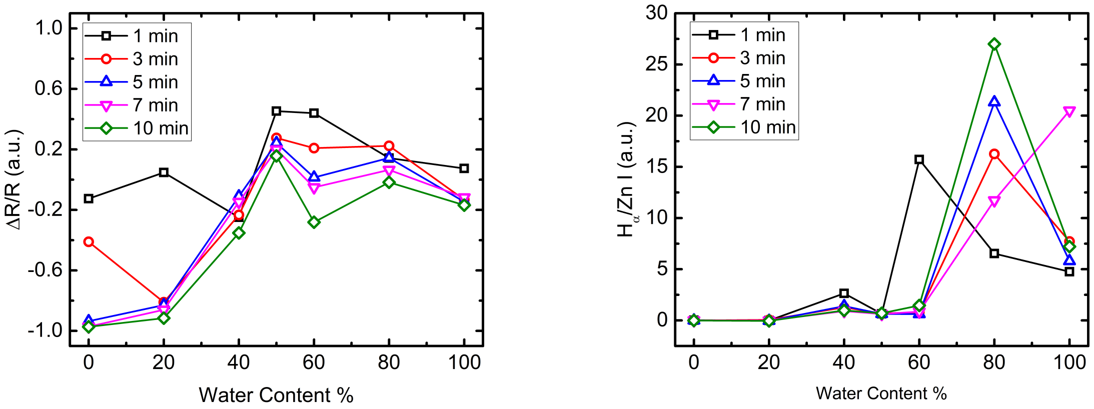

FIGURE 3.13: The differential reflectance and the H_α/Zn I ratio from the OES, at varying water vapor content and discharge duration

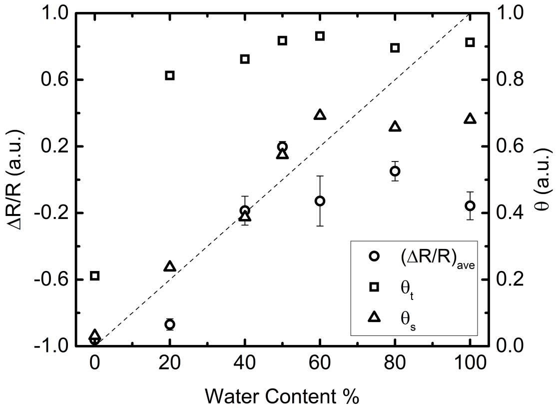

FIGURE 3.14: The averaged differential reflectance (5 to 10 minutes) at increasing water vapor content. The compound fraction θ_t and θ_s from Berg's time-resolved reactive magnetron sputtering model are shown as comparison. The dashed lines are to guide the eyes.

the H_α to Zn I ratio started at the 60% water vapor content and varied widely. This trend may suggest that the optical emission spectra alone was insufficient in directly measuring changes strongly related to the target surface.

Comparing the predictions from Berg's time-resolved magnetron sputtering model (Chapter 2), the differential reflectance showed a similar trend with that of θ_s than θ_t, particularly at the 0 to 60% water vapor content settings. This behavior reinforces the viability of the differential reflectance technique for *in-situ* monitoring of the target surface when incident onto the center region of the magnetron target surface during the reactive magnetron sputtering process.

3.5 Summary of Results

The target surface condition at varying water vapor content and the center and racetrack regions of the metallic target at the magnetron sputtering cathode were investigated through its surface composition using X-ray diffraction, surface morphology using laser microscopy, and through laser differential reflectance as an *in-situ* monitoring technique. The magnetron sputtering cathode regions showed different dominant surface processes. At the center, the redeposition of material was preferred, while the erosion of target material by sputtering was dominant at the racetrack region. This difference was confirmed through the XRD that showed the presence of redeposited layers with a preferred crystallographic orientation at the 0% and 20% water vapor content, and the presence of the oxide through the (100) and (002) peaks of ZnO at the higher water vapor content. While the R_a for both regions decreased at increasing water vapor content, the R_{sk} decreased to a negative value at the racetrack, indicated by the pitting phenomenon observed with the laser microscope images of the higher water vapor content settings. The trend for the oxide formation as estimated by the XRD, the decrease in R_a, and the differential reflectance at the center region were similar to that of the θ_s from Berg's time-resolved mode. These results elucidated what happened to the target surface during operation with water vapor plasma and show that the surface differential reflectance using a laser incident at the center region is a viable *in-situ* method for monitoring the target surface changes during reactive magnetron sputtering.

References

[1] S. Berg and T. Nyberg, "Fundamental understanding and modeling of reactive sputtering processes," *Thin Solid Films*, vol. 476, 215–230, 2 2005.

[2] K. Strijckmans, R. Schelfhout, and D. Depla, "Tutorial: Hysteresis during the reactive magnetron sputtering process," *Journal of Applied Physics*, vol. 124, 24 2018.

[3] J. T. Gudmundsson, "Physics and technology of magnetron sputtering discharges," *Plasma Sources Science and Technology*, vol. 29, 11 Nov. 2020.

[4] Y. Yamamura and H. Tawara, "Energy dependence of ion-induced sputtering yields from monatomic solids at normal incidence," *Atomic Data and Nuclear Data Tables*, vol. 62, 149–253, 2 1996.

[5] S Swann, "Magnetron sputtering," *Metal Finishing*, vol. 98, 76, 12 1988.

[6] M. Kustner, W. Eckstein, V. Dose, and J. Roth, "The influence of surface roughness on the angular dependence of the sputter yield," *Nuclear Instruments and Methods in Physics Research B*, vol. 145, 320–331, 1998.

[7] F. Boydens, W. P. Leroy, R. Persoons, and D. Depla, "The influence of target surface morphology on the deposition flux during direct-current magnetron sputtering," *Thin Solid Films*, vol. 531, 32–41, 2013.

[8] J. E. Greene, J. E. Sundgren, L. Hultman, I. Petrov, and D. B. Bergstrom, "Development of preferred orientation in polycrystalline tin layers grown by ultrahigh vacuum reactive magnetron sputtering," *Applied Physics Letters*, vol. 67, 2928, 1995.

[9] I. Petrov, P. B. Barna, L. Hultman, and J. E. Greene, "Microstructural evolution during film growth," *Journal of Vacuum Science and Technology A: Vacuum, Surfaces, and Films*, vol. 21, S117–S128, 5 2003.

[10] W. Bragg and W. Bragg, "The reflection of X-rays by crystals," *Proceedings of the Royal Society A*, vol. 88, 428–438, 605 1913.

[11] E. S. Ameh, "A review of basic crystallography and x-ray diffraction applications," *International Journal of Advanced Manufacturing Technology*, vol. 105, 3289–3302, 7-8 Dec. 2019.

[12] T. Mueller, M. Jordan, T. Schneider, A. Poesch, and E. Reithmeier, "Measurement of steep edges and undercuts in confocal microscopy," *Micron*, vol. 84, 79–95, 2016.

[13] X. Teng, F. Li, and C. Lu, "Visualization of materials using the confocal laser scanning microscopy technique," *Chemical Society Reviews*, vol. 8, 2020.

[14] M. Arif and C. Eisenmenger-Sittner, "In situ assessment of target poisoning evolution in magnetron sputtering," *Surface and Coatings Technology*, vol. 324, 345–352, 2017.

[15] H. Kwon and J. J. Yoh, "Polarized reflectance of aluminum and nickel to 532, 355 and 266 nm nd:yag laser beams for varying surface finish," *Optics and Laser Technology*, vol. 44, 1823–1828, 6 2012.

[16] M. Palummo, N. Witkowski, O. Pluchery, R. D. Sole, and Y. Borensztein, "Reflectance-anisotropy spectroscopy and surface differential reflectance spectra at the si(100) surface: Combined experimental and theoretical study," *Physical Review B - Condensed Matter and Materials Physics*, vol. 79, 3 2009.

[17] R. Forker, M. Gruenewald, and T. Fritz, "Optical differential reflectance spectroscopy on thin molecular films," *Annual Reports on the Progress of Chemistry - Section C*, vol. 108, 34–68, 2012.

[18] A. Navarro-Quezada, M. Aiglinger, E. Ghanbari, T. Wagner, and P. Zeppenfeld, "Polarization-dependent differential reflectance spectroscopy for real-time monitoring of organic thin film growth," *Review of Scientific Instruments*, vol. 86, 11 Nov. 2015.

[19] L. Simonot, D. Babonneau, S. Camelio, D. Lantiat, P. Guérin, B. Lamongie, and V. Antad, "In situ optical spectroscopy during deposition of ag:si3n4 nanocomposite films by magnetron sputtering," *Thin Solid Films*, vol. 518, 2637–2643, 10 Mar. 2010.

[20] A. L. Priol, L. Simonot, G. Abadias, P. Guérin, P. O. Renault, and E. L. Bourhis, "Real-time curvature and optical spectroscopy monitoring of magnetron-sputtered wti alloy thin films," *Surface and Coatings Technology*, vol. 237, 112–117, Dec. 2013.

[21] I. Gozhyk, L. Dai, Q. Herault, R. Lazzari, and S. Grachev, "Plasma emission correction in reflectivity spectroscopy during sputtering deposition," *Journal of Physics D: Applied Physics*, vol. 52, 2019.

[22] A. Kramida, Yu. Ralchenko, J. Reader, and and NIST ASD Team, NIST Atomic Spectra Database (ver. 5.10), [Online]. Available:https://physics.nist.gov/asd. National Institute of Standards and Technology, Gaithersburg, MD. 2022.

[23] Y. Abe, K. Takamura, M. Kawamura, and K. Sasaki, "Target surface oxide layer formed by reactive sputtering of ti target in ar+o2 mixed gas," *Journal of Vacuum Science and Technology A: Vacuum, Surfaces, and Films*, vol. 23, 1371–1374, 5 Sep. 2005.

[24] R. Schelfhout, K. Strijckmans, F. Boydens, and D. Depla, "On the target surface cleanness during magnetron sputtering," *Applied Surface Science*, vol. 355, 743–747, Nov. 2015.

[25] N. S. J. Braithwaite, "Introduction to gas discharges," *Plasma Sources Science and Technology*, vol. 9, 517–527, 4 2000.

[26] A. Sarani, A. Nikiforov, and C. Leys, "Atmospheric pressure plasma jet in Ar and Ar/H2O mixtures: Optical emission spectroscopy and temperature measurements," *Physics of Plasmas*, vol. 17, 1–8, 6 2010.

[27] S. E. Long and R. F. Browner, "Influence of water on conditions in the inductively coupled argon plasma," *Spectrochimica Acta Part B: Atomic Spectroscopy*, vol. 43, 1461–1471, 12 1988.

[28] P. H. Ratliff and W. W. Harrison, "The effects of water vapor in glow discharge mass spectrometry," *Spectrochimica Acta Part B: Atomic Spectroscopy*, vol. 49, 1747–1757, 12-14 1994.

[29] H. Webb, V. Truong, J. Hasan, C. Fluke, R. Crawford, and E. Ivanova, "Roughness parameters for standard description of surface nanoarchitecture," *Scanning*, vol. 34, 257–263, 2012.

Chapter 4

DEPOSITION OF ZNO THIN FILMS USING WATER VAPOR PLASMA

4.1 Introduction

In this chapter, the effect of water vapor plasma on the reactive magnetron sputtering process is investigated experimentally at the substrate region during the deposition process. In line with Chapter 3, the effect of the argon (Ar) and water vapor gas admixture was investigated at varying water vapor content, and the effect of commonly employed methods in thin film deposition, such as the application of a substrate bias and substrate heating was explored.

4.2 Thin Film Deposition

The reactive magnetron sputtering process is often utilized for the deposition of thin films. One of the applications of films deposited using this method is as transparent conductive electrodes, using oxides such as zinc oxide (ZnO). Using a reactive gas with ZnO film deposition allows for the formation of film structures that are not realized typically with inert gas sputtering involving compound targets. The film properties can also be easily modified using this technique, either through thin film doping with heavy or light ions or through modification of the deposition process, such as the heating of the substrate surface or applying a substrate bias.

Water vapor plasma is not used conventionally as a reactive gas for the reactive magnetron sputtering thin film deposition process. Particularly for ZnO, using water vapor is advantageous mainly because of the addition of hydrogen (H) ions into the plasma. H ions are a known shallow donor dopant for ZnO and have been demonstrated to improve the conductivity of the film and reduce lattice stresses without excessive modification of the film's band structure [1, 2]. This modification is crucial for transparent conductive oxide applications, where a high conductivity and good film adhesion to the surface are desired [3]. However, an important consideration is that water vapor is highly adsorptive, including at the substrate region. The film formation is strongly affected by the adsorption phenomenon, which includes multi-layer formation through physisorption or chemisorption [4–6]. This behavior can result in the inhomogeneity of the plasma in the bulk and the near-surface regions, which can significantly affect the film's properties. Thus, in this chapter, the ZnO film formation process using water vapor plasma was investigated to identify the effect of the adsorption properties and the plasma parameters on the grown film. The near-substrate surface plasma characteristics were measured using a single Langmuir probe. The deposition condition effect was also determined by varying the substrate bias and temperature. The film properties were evaluated from the film structure

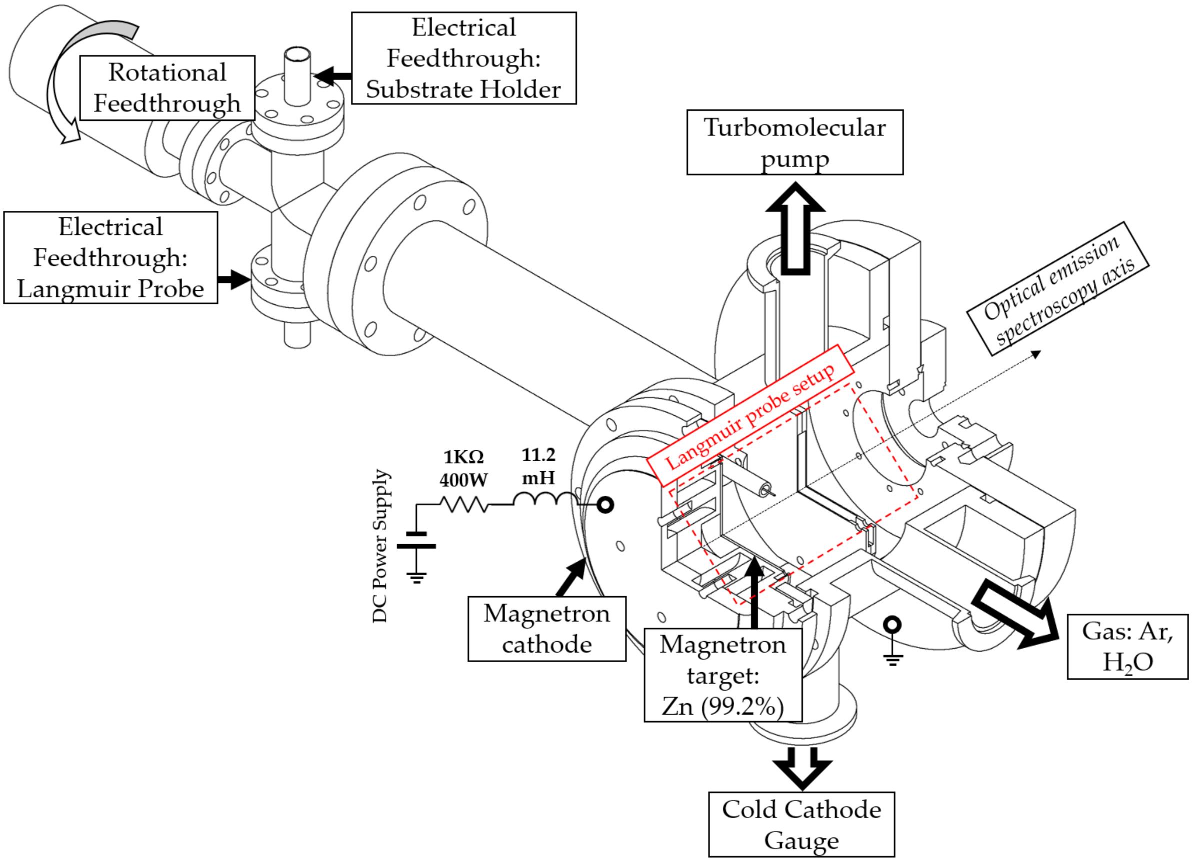

FIGURE 4.1: The reactive magnetron sputtering system with the substrate holder-Langmuir probe configuration for the near substrate surface measurements. The optical emission spectroscopy was performed at an axial axis without the substrate holder.

(X-ray diffraction), surface morphology (X-ray reflectivity or laser microscopy), and its opto-electronic properties (optical transmission spectroscopy, 4-point probe measurements, optical band gap measurement).

4.3 Experimental System

The experimental system, as shown in Fig. 4.1, consisted of the reactive magnetron sputtering system previously described in Chapter 2 and the magnetron cathode described in Chapter 3. The water vapor reservoir was kept at ≈60°C. The discharge current and working pressure were kept constant at 100 mA and 1.0 Pa, respectively. The optical emission spectroscopy (OES) was taken at the central axis of the chamber using a USB spectrometer (400-900 nm: Ocean Optics, USB4000; 200-400 nm: Ocean Optics, Flame) at an integration time of 100 ms and averaged 7 times.

4.3.1 Substrate Holder Design

Positioned 40 mm away from the substrate surface is the stainless steel substrate holder utilized in the deposition process (Fig. 4.3). The deposition area of the holder was approximately

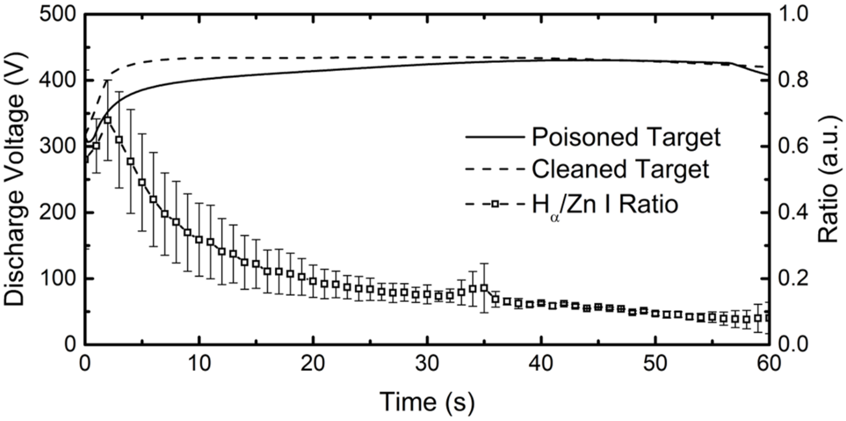

FIGURE 4.2: The effect of 1.0 Pa Ar cleaning on the measured discharge voltage and the H_α to Zn I ratio obtained using optical emission spectroscopy (OES) at the central axis as indicated in Fig. 4.1. The target was exposed to a 1.0 Pa water vapor plasma prior to the cleaning step.

38.5 cm^2, and this realized a 1:1 substrate-to-target area ratio. The holder was mounted on a rotational feedthrough to allow for target cleaning using 1.0 Pa Ar at 100 mA discharge current without contamination onto the substrates. Borosilicate glass (Matsunami Glass, S1111) was used as the substrate (10x20 mm^2 size, 10x10 mm^2 for 4-point probe resistivity). The substrates were cleaned through ultrasonication in acetone, ethanol, and distilled water separately for 10 minutes and dried before introduction into the vacuum system.

As shown in Fig. 4.2, the target cleaning using 1.0 Pa Ar at 100 mA discharge current for a 1-minute duration was sufficient to clean up the target surface. After the 1 minute discharge, the discharge voltage approached that of a clean target, and the H_α to Zn I, which estimated the introduction of reactive gas from the target surface to the bulk plasma due to the target poisoning, had minimized to a saturation level after 1-minute duration.

In the Ar-H_2O gas admixture experiments and substrate heating experiments, the substrate was at a floating potential. The substrate bias used a DC power supply (Kikusui Electric, PAS160-2S) at a range of -50 to 50 V. The substrate heating utilized a resistive space heater (Sakaguchi Electric Heating, SH1060LT 60W-120V) sandwiched between the SUS plates of the substrate holder. A variable autotransformer (Yamabishi Co. Ltd., V-130-3) controlled the temperature. The temperature was investigated from 20^{o}C to 140^{o}C. Sufficient outgassing to the initial base pressure was performed prior to experiments to minimize the presence of adsorbed species at the substrate surface. The electric potential variations arising from the substrate heater during its operation were assumed to be minimal. The ambient heating from the plasma for the whole deposition duration and temperature at the substrate surface was measured using a shielded, 2.0 mm diameter K-type thermocouple with an exposed tip of 10 mm at the substrate surface position. The 1.0 Pa water vapor setting was used for the substrate bias and heating experiments. This setting kept constant the adsorptive and reactive behavior of water vapor as the substrate deposition conditions varied.

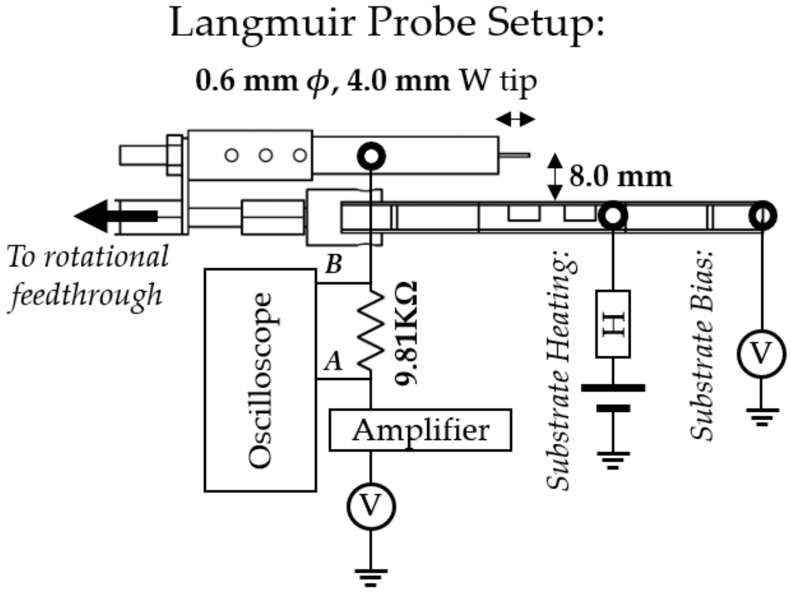

FIGURE 4.3: The near substrate Langmuir probe setup with the substrate heating and bias configuration utilized. The heating was realized using a resistive substrate heater and the bias was powered using a DC power supply. The whole configuration is mounted on a rotational feedthrough

4.3.2 Near Surface Single Langmuir Probe

The single Langmuir probe measured the plasma parameters near the substrate surface. The transport of ions and electrons to the surface in the presence of plasma will allow us to identify key plasma parameters, however, a fundamental understanding of its theory is required. This involves the formation of sheaths near the surface, which is one of the fundamental characteristics of plasma.

4.3.2.1 Langmuir Probe Theory

When a surface is immersed in plasma, the sheath forms at the edge of the surface. This behavior is a consequence of the varying mobilities of ions and electrons with a finite temperature and is described by the Debye shielding length λ_D:

$$\lambda_D = \sqrt{\frac{\epsilon_o k_B T_e}{n_e q^2}} \tag{4.1}$$

where ϵ_o is the permittivity of vacuum, k_B is Boltzmann's constant, T_e is the electron temperature, n_e is the electron density, and q is the charge of an electron. As the electrons were collected at the surface, a positive potential ϕ exists at the bulk of the plasma and the wall would be at a negative potential with respect to the plasma. Considering the surface is planar and is sufficiently larger than the λ_D, the current collected normal to the surface (z direction) can be described through the current density, j_e, as shown:

$$j_e = q\int\int\int v_z f(x,v,t)dv_x dv_y dv_z \tag{4.2}$$

where $f(x,v,t)$ is the electron distribution considered at the volume near the surface. As the surface is negatively biased, the minimum velocity required for electron collection in the z direction is:

$$v_{min} = \sqrt{\frac{2e(V_p - V_{bias}))}{m_e}} \tag{4.3}$$

where V_p is the potential at the bulk plasma, V_{bias} is the potential at the surface, and m_e is the electron mass. Assuming that the electrons are in a Maxwellian distribution, the electron current, $I_{electron}$, collected by the probe of surface area, A, can then be determined by multiplying the collection area to j_e in Eq. 4.2:

$$I_{electron} = Aqn_e(\frac{m_e}{2\pi k_B T_e})^{\frac{3}{2}}\int_{v_{min}}^{\infty}\int_{-\infty}^{+\infty}\int_{-\infty}^{+\infty} v_z e^{-\frac{m_e v^2}{2k_B T_e}} dv_x dv_y dv_z \tag{4.4}$$

Integrating Eq. 4.4 will yield the theoretical electron current measured at the surface. Accounting for the limit when the surface is positive with respect to the plasma, $I_{electron}$ is described as:

$$I_{electron} = \begin{cases} Aqn_e\sqrt{\frac{T_e}{2\pi m_e}}e^{\frac{-q(V_p - V_{bias})}{k_B T_e}} & \text{if } V_{bias} \leq V_p \\ Aqn_e\sqrt{\frac{T_e}{2\pi m_e}} & \text{if } V_{bias} > V_p \end{cases} \tag{4.5}$$

which indicates that $I_{electron}$ varies exponentially in the bias range more negative than the plasma potential, and afterward, the current will saturate and is related to the electron thermal speed. For the ion contribution, the case is different. Given that the ion mass is significantly greater than that of an electron, at the sheath edge, the density of the ions n_i is greater than that of electrons, n_e. The potential change at the sheath region is expressed using the one-dimensional Poisson's equation:

$$\frac{d^2\phi}{dx^2} = -\frac{q}{\epsilon_o}(n_i(x) - n_e(x)) = \frac{q}{\epsilon_o}n_o[e^{\frac{q\phi}{k_B T_e}} - (1 - \frac{2q\phi}{m_{ion}v_{ion}^2})^{-\frac{1}{2}}] \tag{4.6}$$

where ϕ is the potential, n_e is described by the Boltzmann relation, and n_i is obtained from the ion continuity equation ($n_0 v_o = n_i(x)v_i(x)$) and the conservation of energy ($\frac{1}{2}m_{ion}v_{ion}^2 = \frac{1}{2}m_{ion}v_o^2$ - $q\phi(x)$). By solving Eq. 4.6, the minimum speed required to reach the surface from the sheath edge, the ion acoustic speed or the Bohm sheath criterion, can be defined as:

$$v_{ion} \geq \sqrt{\frac{k_B Te}{m_{ion}}} \tag{4.7}$$

The ion current, I_{ion}, collected by the probe can then be expressed using this minimum speed requirement as:

$$I_{ion} = Aqn_{o,i}\sqrt{\frac{k_B T_e}{m_{ion}}} \tag{4.8}$$

Combining the current contributions towards the surface can then be full described as [7–10]:

$$I_{probe} = I_{ion} - I_{electron} = Aq(n_{o,i}\sqrt{\frac{k_B T_e}{m_{ion}}} + n_{o,e}\sqrt{\frac{T_e}{2\pi m_e}}e^{\frac{-q(V_p - V_{bias})}{k_B T_e}}) \tag{4.9}$$

Considering these equations, the theoretical Langmuir probe trace will consist of three distinct regions. First is the ion saturation region at negative biases, where the current is constant. Next is the transition region, where the electron current increases exponentially as the electrons start collecting at the probe surface. Then, the electron saturation region, where the current again becomes constant after crossing V_p.

4.3.2.2 Experimental Configuration

The plasma characteristics were measured using a cylindrical single Langmuir probe with a tungsten (W) probe tip of 0.6 mm diameter and 4.0 mm exposed length. Alumina tube sleeves for the insulation and copper tube electrostatic shielding for spurious noise pickup prevention were employed (Fig. 4.4). The probe was positioned as shown in Fig. 4.3 and was 8.0 mm away from the center of the substrate holder surface. The position was chosen to be within the range of several Debye shielding lengths (>$10\lambda_D$, at $T_e \approx 5$ eV, $n_e \approx 5\text{x}10^{14}$ m^{-3} using Eq. 4.1). Measurements were taken after running the discharge for 1 minute. The probe bias was swept from -40 to 12 V in a 1.0 Hz ramp waveform, using a function generator (EZ Digital Co. Ltd., Model DFG-6020) connected to an amplifier ((Turtle Industry Co. Ltd., Model T-AMP03HC). The probe current, I_{probe}, was measured from the voltage drop across the resistor (R_{res}=9.81 kΩ), shown in Eq. 4.10, as measured on the oscilloscope (Pico Technology, Model Picoscope 4223).

$$I_{probe} = \frac{V_{Ch.B} - V_{Ch.A}}{R_{res}} \tag{4.10}$$

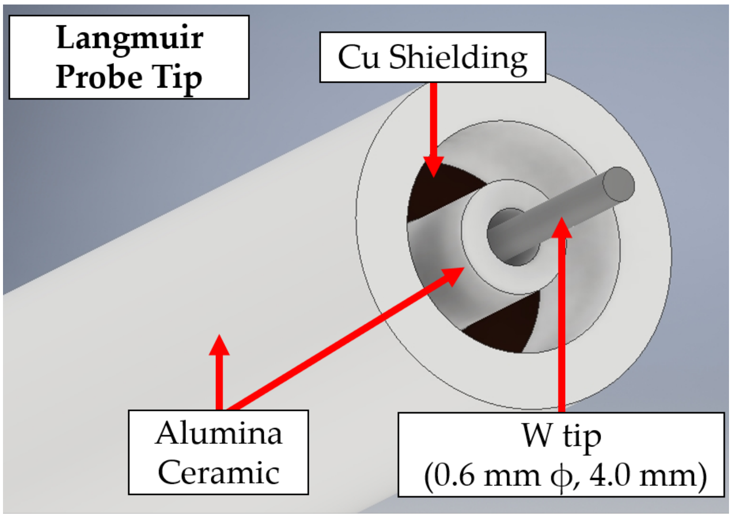

FIGURE 4.4: The single Langmuir probe tip configuration used for the near surface measurements.

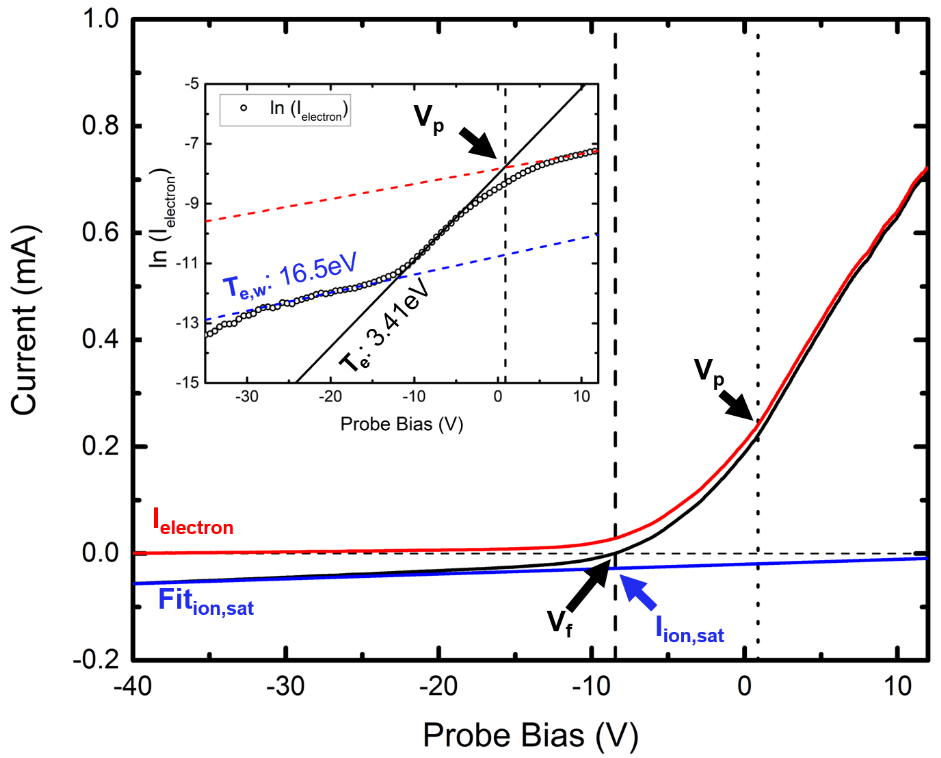

FIGURE 4.5: The typical single Langmuir probe trace and how the plasma parameters (V_f, $I_{ion,sat}$, T_e, V_p) were measured. The blue trace indicates the probe current, and the red trace indicates the electron current, $I_{electron}$, at a 1.0 Pa Ar plasma, at a 100 mA discharge current. The inset graph shows the fitting of the two T_e typically observed for magnetron sputtering plasmas.

The bias range was selected to minimize damage to the probe tip and improve measurement accuracy. Possible causes are electron-induced heating and an excessive increase in the probe area resulting in a large current drain from the plasma according to the electron orbital motion limit theory. This increase in the area also modifies the local plasma and affects the accuracy of the parameters from the probe characteristic, thus, it is beneficial to select the ideal bias range for measurement [11–14]. The film formation on the surface of the Langmuir probe can significantly affect the probe trace [15–18], therefore, a replaceable tip configuration was employed to reduce this.

4.3.2.3 Analysis of Langmuir Probe Trace

For experimentally measured single Langmuir probe traces, the behavior is different from what is described in Eq. 4.9. Figure 4.5 shows the typical single Langmuir probe trace measured in experiments. The ion and electron saturation regions predicted by the theory are not constant values, and the distinct change from the transition to the electron saturation region that denotes V_p is not distinct. As such, the analysis of the probe trace is as follows [7–9, 19].

From Eq. 4.8, the ion saturation current is directly related to the n_i at the bulk of the plasma. However, this can be difficult as I_{ion} varies with an increasing V_{probe}, and there are multiple ion species in the deposition plasma. The effective ion mass is difficult to determine, as changes in discharge parameters could significantly affect the ratio of the ion species present. Thus, the ion saturation current, $I_{ion,sat}$ was used as a measure for the n_i and is taken at the floating potential, V_f, where the contributions of the ions and electrons to the probe current are equal (n_i = n_e). V_f can be seen in Fig. 4.5 as the voltage at the point of zero current crossing of the Langmuir probe trace. $I_{ion,sat}$ was obtained by taking a linear fit of the ion saturation region and is the current of the fit at V_f. This linear fit was subtracted from I_{probe} to obtain $I_{electron}$. In the transition region, the $I_{electron}$ from Eq. 4.5 can also be expressed as:

$$I_{electron} = I_{e,sat}e^{\frac{-q(V_p - V_{bias})}{k_B T_e}} \tag{4.11}$$

where $I_{e,sat}$ is the electron saturation current. From Eq. 4.11 and Fig. 4.5, it can be seen that T_e can be obtained from the slope of the $\ln(I_{electron})$ against V_{probe} (slope = $\frac{1}{k_B T_e}$). V_p can be measured in different ways. The common methods are the first derivative method and the intersection of the linear T_e fit with the linear extrapolation from the electron saturation region in $\ln(I_{electron})$-V_{probe} plot. Particularly for magnetized plasma, using the derivative method can lead to inaccurate measurements of V_p if the transition region range is small and the electron saturation region is non-distinct. This phenomenon can be attributed to the electron collection of the probe, the presence of a magnetic field, collisions in the sheath, or a high noise level [11, 13]. V_p was measured using the intersection method. From the parameters obtained, the effective energy of the ions in the plasma, E_p, at the Langmuir probe position can then be obtained as:

$$E_p = q(V_p - V_{surface}) \tag{4.12}$$

where $V_{surface}$ is equal to V_f if there is no bias, or V_{bias} if the surface is held at a specific potential such as when adding a substrate bias [20–23]

Consider the presence of the second linear portion of the $\ln(I_{electron})$ plot in Fig. 4.5. This portion indicates a higher temperature electron tail, $T_{e,w}$. Thus, the plasma is non-Maxwellian, which has been observed for magnetron sputtering plasmas [24, 25]. Considering this and the multi-species nature of the plasma, the electron density, n_e, was calculated using the Druyvesteyn method instead of Eq. 4.5. The electron energy distribution function (EEDF) can be related to the second derivative of $I_{electron}$ trace by:

$$f(E) = (\frac{2m_e}{q^2 A})\sqrt{\frac{2q}{m_e}}(\sqrt{E_{p-probe}})\frac{d^2 I_{electron}}{dV_{probe}^2} \tag{4.13}$$

where $E_{p-probe}$ = V_p - V_{probe}. The electron density, n_e, was obtained by integrating $f(E)$ for the given energy range [8, 26–28]. Given the dependence of the distribution and the Langmuir probe trace in general, smoothing techniques to remove the significant noise was employed throughout the analysis [29–31]. Shown in Fig. 4.6 are the typical EEDF that can be obtained using the Druyvesteyn method at three different water vapor content settings.

4.3.3 Materials Characterization Techniques

The effect of the near-surface plasma on the deposition process was investigated through the deposited thin film. In this study, the properties were measured using X-ray diffraction and

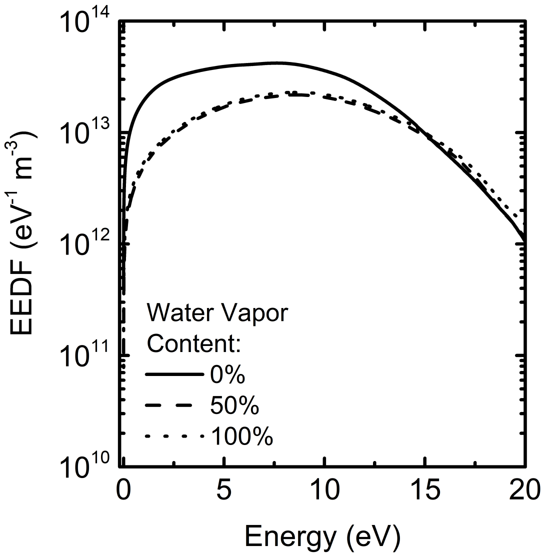

FIGURE 4.6: The electron energy distribution obtained using the Druyvesteyn method for 0%, 50%, and 100% water vapor content settings.

reflectivity (crystal structure, roughness, and thickness), optical transmittance spectroscopy (optical transmittance and band gap), and 4-point probe measurements (resistivity).

4.3.3.1 X-ray Diffraction and Reflectivity

Aside from material identification as described in Chapter 3, the crystallite size and the quality of the thin film can be measured using X-ray diffraction (PANalytical X'Pert Pro, Cu K$_\alpha$ = 1.540598 Å, Bragg Brentano configuration). The broadening of the peaks in XRD is a measure for the crystallite size, D, according to the Debye-Scherrer equation:

$$D = \frac{k_{DS}\lambda}{\beta cos\theta_{xrd}} \tag{4.14}$$

where λ is the X-ray wavelength, k_{DS} is a material constant (k_{DS} = 0.94), and β is the full width at half maximum (FWHM) of the peak [32, 33]. β and the peak area were measured through the fitting with a Gaussian peak distribution as shown in Fig. 4.7. The peak was normalized, and the amorphous background contribution from the glass substrate was subtracted before fitting the single most intense Zn or ZnO peak. This method was applied to quantify the effect of the reactive water vapor plasma to the crystal structure of the produced singly oriented ZnO.

The film's thickness and roughness were measured via the X-ray reflectivity technique (Fig. 4.8, where compared to the Bragg Brentano configuration, the X-rays are injected at a low incidence angle with respect to the film surface. At angles greater than θ_C, the reflected and refracted radiation produces an interference pattern called Kiessig's fringes. The difference in the maxima or minima, θ_M, is related to the thin film thickness, t_{film}, according to Eq. 4.15:

$$t_{film} = \frac{\lambda}{2\Delta\theta_M} \tag{4.15}$$

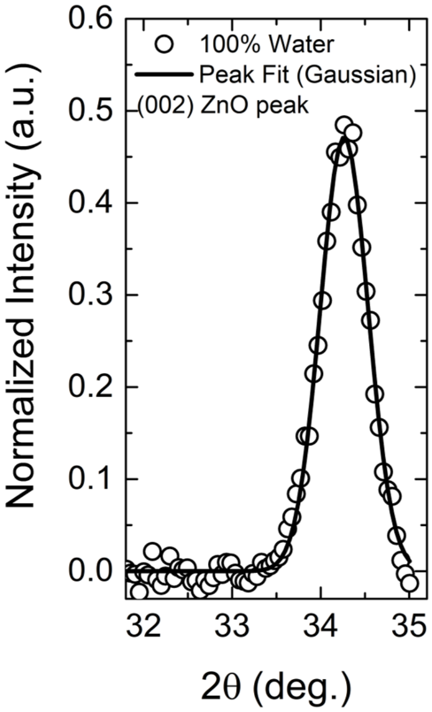

FIGURE 4.7: The Gaussian peak fitting of the XRD peak for the β and peak area

This technique is effective for a thickness range of 2 to 200 nm. Laser microscopy measured the thickness and roughness of thicker, non-transparent films. Laser microscopy was limited for transparent thin films as the surface morphology can be difficult to detect. From the XRR results, the slope of the reflectivity yields the roughness. In a simple Gaussian case for the surface roughness, R_a determined from the square root of the normalized reflectivity against the square of the scattering vector, K (where $K = \frac{4\pi \sin\theta_{XRR}}{\lambda}$) [34–36].

4.3.3.2 Optoelectronic Properties

The film's transmittance (T_{tr}) gauged the film's optical transparency from 360 to 900 nm. The light source was a Xe flash lamp, with a USB spectrometer (Ocean Optics, USB4000) as the detector. The light was focused onto the sample using a synthetic quartz condenser lens (OptoSigma, SLSQ-25.4-100P). The effective measurement area consists of a 2.4 mm diameter aperture with an integration time of 250 ms and a 7x average. The average transparency was from the visible range (400 to 750 nm).

The resistivity of the thin films was measured using a custom-built 4-point probe with a linear configuration. A source-measure unit (Keysight, B2901) in the 4-wire configuration acted as the current source and voltmeter. The *I*-*V* trace was obtained from 0 to 100 nA on films deposited on 10x10 mm glass substrates. The resistivity ρ was obtained using Eq. 4.16

$$\rho = \frac{\pi}{\ln(2)}(\frac{V_{measured}}{I_{source}})K_o t_{film} \tag{4.16}$$

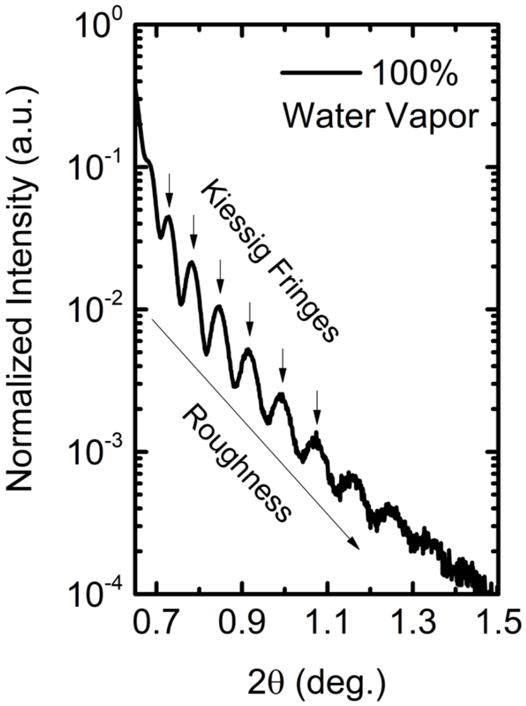

FIGURE 4.8: The typical normalized X-ray reflectivity (XRR) of ZnO deposited using 1.0 Pa water vapor plasma. The Kiessig fringes and the component correlated with the roughness in the XRR data are shown.

where $V_{measured}$ is the voltage as I_{source} is varied and K_o is a correction factor from the probe geometry (K_o = 4.0095) [37]. The band gap, E_g, of the ZnO thin films was measured using Tauc's method. From the transmittance of the thin films, T_{tr}, the absorption coefficient α_{tauc} was calculated as shown in Eq. 4.17:

$$\alpha_{tauc} = \frac{1}{t_{film}} \ln \frac{1}{T_{tr}} \tag{4.17}$$

From α_{tauc}, the direct band gap of ZnO was obtained by fitting the linear portion of $(\alpha_{tauc} h\nu_{\lambda})$ vs $h\nu_{\lambda}$, where $h\nu_{\lambda}$ is the photon energy as shown in Fig. 4.9. The band gap is the x-intercept of the linear fit [38–40].

4.4 Effect of Water Vapor

The XRD peaks measured from the films deposited at increasing water vapor content are shown in Fig. 4.10. As the water vapor content increased, the peak positions shifted from predominantly Zn ((002),(100), and (101)) to singly oriented ZnO ((002)). At the 20% water vapor content, both Zn and ZnO ((002), (101)) are present.

Shown in Fig. 4.11 are the X-ray reflectivity curves of the films deposited at varying water vapor content, substrate temperature, and substrate bias conditions. As the water vapor

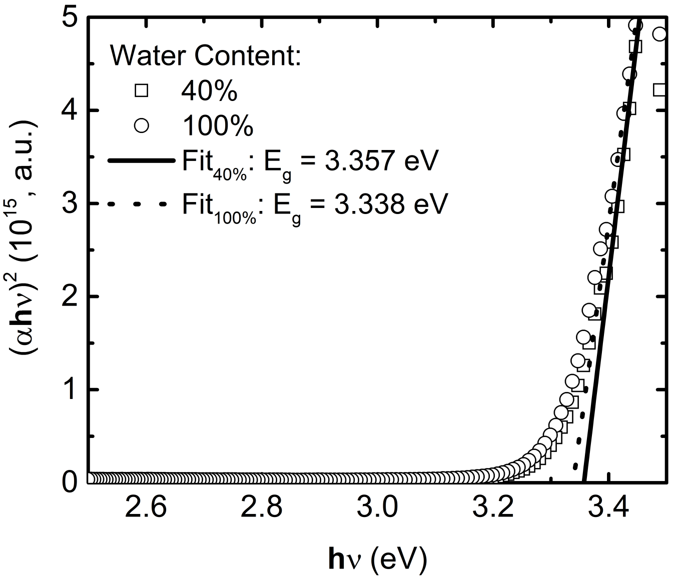

FIGURE 4.9: The Tauc plot for the measurement of the deposited thin film's band gap. The x-interecept of the linear portion of the plot denotes the film's band gap.

content increased, the Kiessig fringes were present from the 40% water vapor content. Variations in θ_c were minimal, typically ranging from 0.6325 to 0.6475. The lack of Kiessig fringes in the 0-20% water content indicates a film thickness and surface roughness greater than the suitable range for the XRR technique (2 to 200nm)[34]. Thus, the thickness was determined using laser microscopy for films without the Kiessig fringes because these films were not transparent. For the 40% to 100% water vapor content settings, the difference in the reflectivity curves was quantified through the surface thickness and the roughness.

Shown in Fig. 4.12 are the transmittance (T_{tr}) for films deposited at varying water vapor content. The 0-20% water content settings were not transparent, as it is predominantly Zn. From the 40 to 100% water content, T_{tr} increased sharply in the 360-400 nm range. Interference wave-like patterns called the Swanepoel fringes are present. Thus, the film's T_{tr} is the average transmittance from 400 to 750 nm. Shown in the inset are the actual images of the deposited thin films.

4.4.1 Plasma Parameters

From the Langmuir probe traces, the magnitude of $I_{electron}$ in the transition to electron saturation region decreased at increasing water vapor content. To clarify the effect, these changes were then quantified using the plasma parameters to explain what happens at the near-substrate region of the plasma. Shown in Fig. 4.13 are the plasma parameters obtained. Initially, at low water vapor content, V_p, $(V_p - V_f)$, T_e, n_e and $I_{ion,sat}$ increased as compared to a pure Ar discharge. As is shown in Fig. 4.5, adding water vapor reduces the low energy electrons in the plasma. This is partly due to the lower ionization energy for water vapor (12.59 eV)

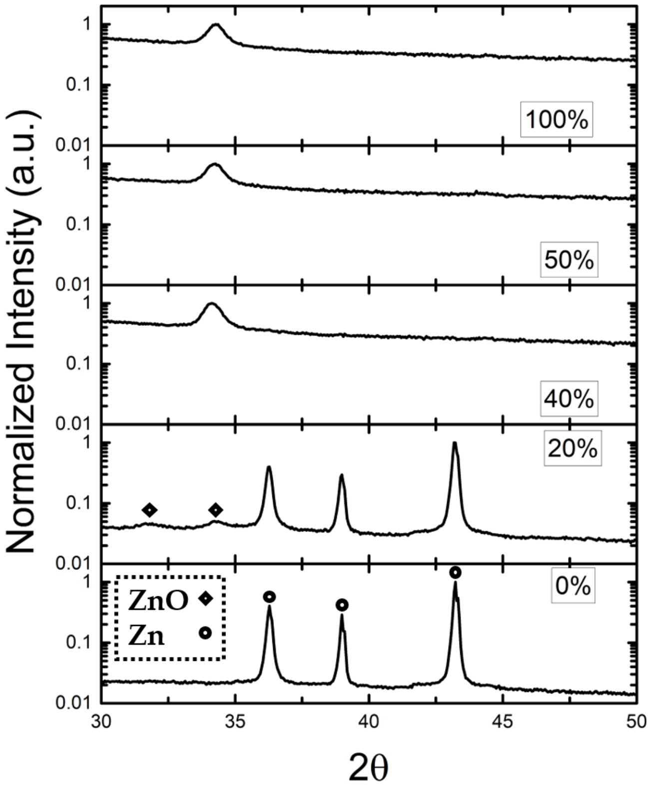

FIGURE 4.10: The XRD peaks obtained from the deposited film samples at varying Ar-H_2O content

as compared to Ar (15.7 eV)[41], and low energy electron reactions with water molecules leading to vibrational and rotational excitations. However, as the water vapor content increased further, a shift to a much more electronegative plasma was observed, which was attributed to sufficient negative ion formation and the depletion of low energy electrons for sustaining the stable discharge. Given that the Zn metal ion has a negative electron affinity, the possible negative ions present in the plasma can be inferred from the reactive species that are confirmed present, such as H, O, and OH[42, 43] with their electron affinities of 0.754 eV, 1.461 eV, and 1.827 eV, respectively[44–46]. While not directly measured, the atomic spectral lines and molecular band spectra of their positive ion counterparts were observed to be present in the discharge together with their parent molecules using OES (Fig. 4.14). It is highly probable that several reactive species in the plasma serve as sources of negative ions. Specifically for the case of a water molecule, dissociative electron attachment is known to produce the negative ions of H^-, O^-, OH^-, and H_2O^- [47]. It has also been reported in reactive magnetron sputtering of oxides that use O_2 as the reactive gas are capable of forming negative ions through the dissociative electron attachment to O_2[48–50], or the negative oxide ions that are sputtered and accelerated from the target surface[51]. This mechanism explains the shift in the initial trend, and T_e reached an increased saturation level while n_e, V_p, $(V_p - V_f)$ and $I_{ion,sat}$ decreased. This change in the reactive behavior also resulted in the increased production of oxide material, which causes the target poisoning phenomenon on the magnetron sputtering target surface. Target poisoning modifies the target chemical composition and particle reflection properties

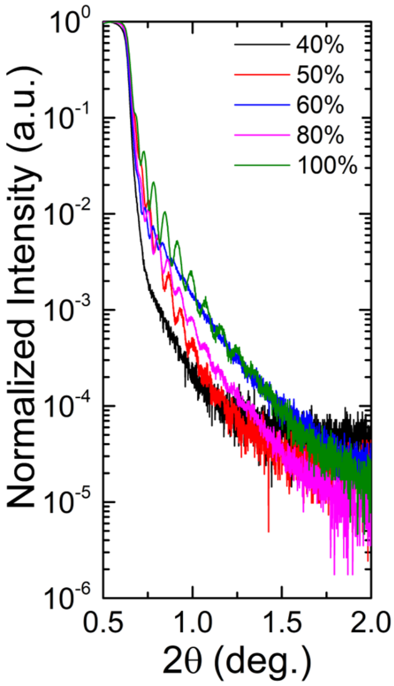

FIGURE 4.11: The X-ray reflectivity curve of the thin films deposited at varying Ar-H_2O content.

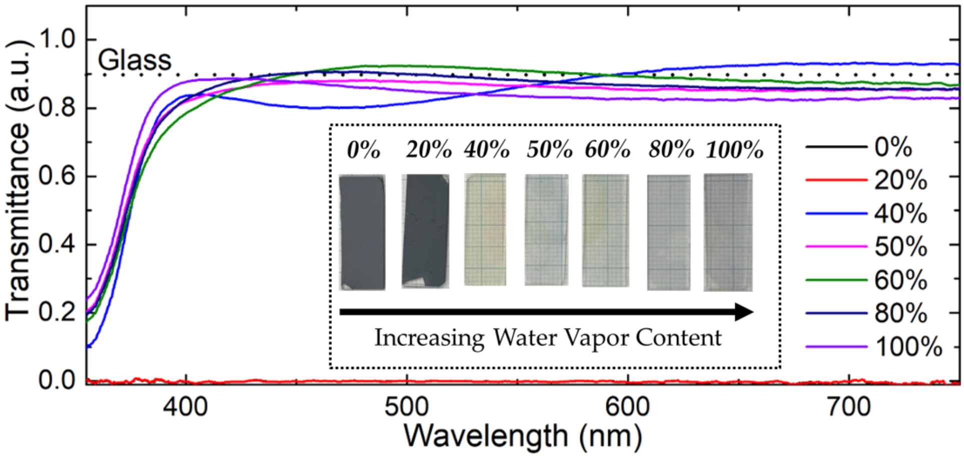

FIGURE 4.12: The transmittance of the deposited thin films at varying Ar-H_2O content. The inset images show the actual images of the deposited films on the glass substrate.

because of the deposition of the oxide material. The presence of the oxide formed on the magnetron target surface specific to water vapor has been reported, and the reduced sputtering efficiency and yield were quantified through the difference in the target surface roughness and differential reflectance (Chapter 3). The longer the discharge operates with water vapor, the more difficult it is to maintain a discharge. This phenomenon can be attributable to a lower density of secondary electrons generated from the sputtering target with the lower efficiency

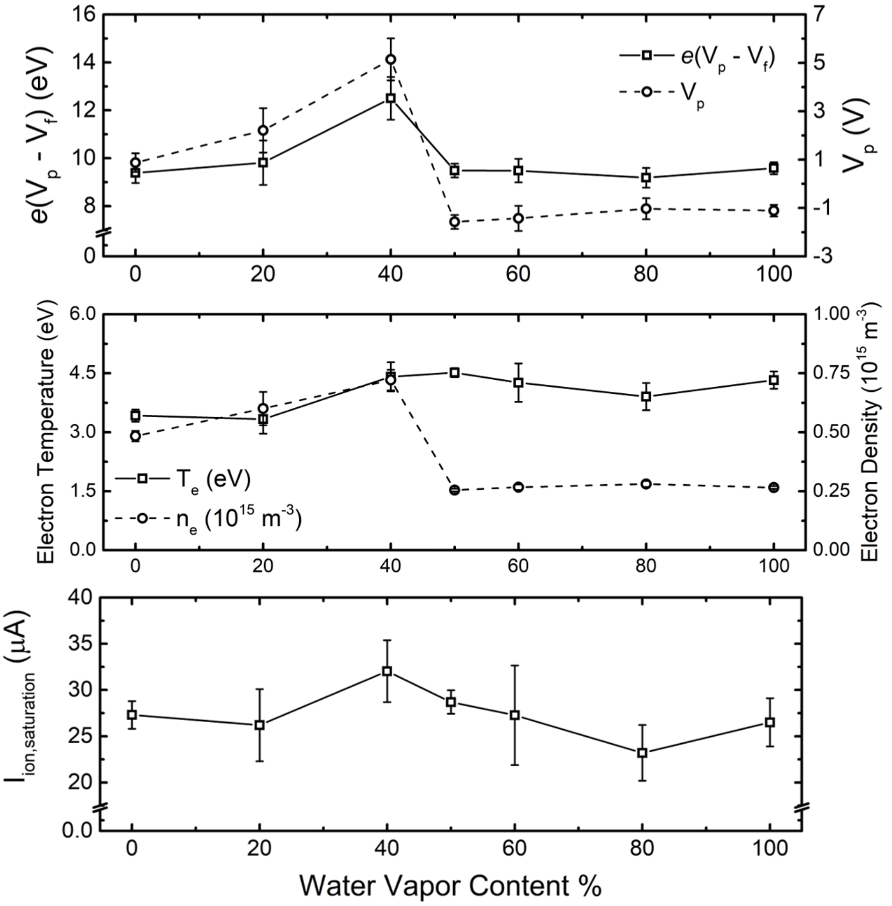

FIGURE 4.13: The effect of water content on the plasma parameters, as measured by a single Langmuir probe.

of the oxide compared to fresh metallic surfaces[52]. The discharge voltage measurements confirm the target poisoning effect. In Fig. 4.15, $V_{ignition}$ is the discharge voltage right after the plasma ignition, and V_{eq} is the voltage after a discharge period of 1 minute. The increase in discharge voltage by plasma operation was observed at the 20% water content, where $V_{ignition}$ is greater than V_{eq}. The difference between $V_{ignition}$ and V_{eq} was the smallest at 40% water content for water vapor containing plasma, and could indicate the threshold water vapor content for sufficient ZnO formation.

4.4.2 Film Properties

The effect of the water vapor content during the plasma deposition process was observed in the film's properties. Shown in Fig. 4.16 is the formed film properties. The peak area corresponding to (002) of ZnO increased at increasing water content, exhibiting a saturation level of around 40% water content. This trend was expected as more reactive gas leads to the formation of more ZnO at the substrate. At the same time as the peak area, the crystallite size evaluated from the highest peak intensity obtained from the XRD was found to decrease, with a saturation value of around 25.6-27.4 nm, from the 93.1 nm obtained for the purely Zn film at the 0% water content. The thickness of the film was obtained from the XRR only for the 40 to 100%

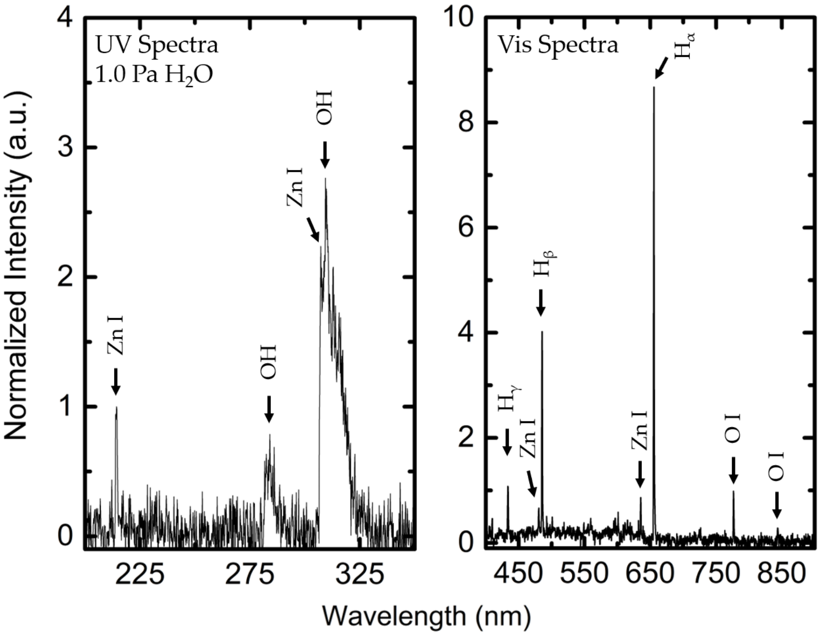

FIGURE 4.14: Optical emission spectra of 1.0 Pa water vapor at the UV (200-400 nm) and visible (400-900 nm) region. The atomic and molecular spectra for H, O, OH, and Zn are highlighted

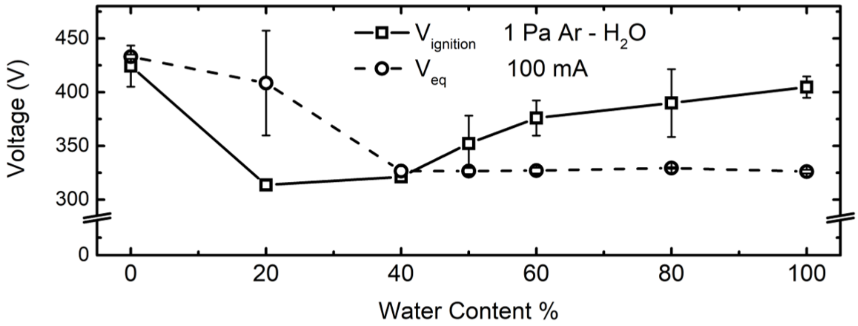

FIGURE 4.15: Discharge voltage measurements at varying water vapor content

water vapor content, due to the lack of Kiessig fringes in films with low ZnO content (0% and 20% water content). As the water content increased, the thickness and roughness decreased and were attributed to a decreased sputtering yield from target poisoning[20, 52].

The film growth mechanism changes to deposition in a reactive plasma at higher water content. This mechanism depends on the surface energy of the planes in the crystal structure for metallic films. Then, the growth mechanism changes depending on the reactive species gas content and the amount of flux as these modify the energy and the surface reaction rate. For the 20% water content, Ar sputtering of Zn at the target surface is dominant (Chapter 3), which results in a high Zn ion flux towards the surface. The oxide formation then depends on the metal surface orientations where oxide nucleation is favored. This behavior was reflected by the lower intensities for multiple ZnO planes compared to a pure Ar discharge Zn film at 20% water vapor content. When the water content is then increased to 40%, more reactive ion and neutral fluxes were realized. This increase coincides with the observed shift to an electronegative plasma as seen in the plasma parameters from the Langmuir probe. The thin

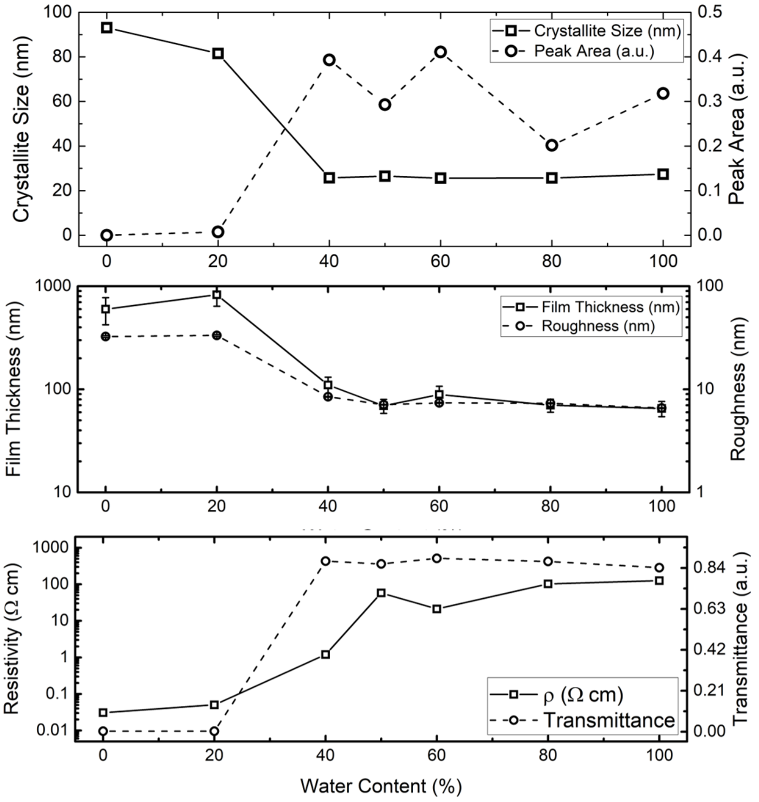

FIGURE 4.16: The effect of water content on the film's properties

film growth mechanism changed to one dominated by the oxide, and for ZnO, the preferred orientation is at (002). The transition to this mechanism decreases the film deposition rate and the roughness due to the selective growth orientation. These result in the single peak spectra observed at 40 to 100% water vapor content. The preferred XRD peak positions strongly correlate to the incident ion energy from the bulk plasma[53, 54]. For the case of water vapor, the experimental results indicate the Zn film deposition transition to (002) ZnO film deposition takes place between 20 to 40% water content.

The electrical resistivity, ρ, and the optical transmittance, T_{tr}, increased similarly with the peak area of (002). The transition started at 40% water vapor content, where the transmittance is at 87.5% and ρ=1.20 Ωcm. These figures represent a 2.6% decrease as compared to the substrate transparency and are in the lower range for typical ρ for ZnO thin films without metallic doping (1-100 Ωcm)[55]. As more oxygen was generated at higher water vapor content, the expected low ρ would be at the transition from the metallic to oxide film, which coincides with the experimental result at the 40% water content. The ρ then steadily increased as more oxygen was present in the plasma as the water content increased. Lower oxygen content during film deposition for ZnO has been strongly correlated to a decrease in resistivity as the oxygen vacancies act as an n-type dopant for ZnO[56, 57].

The measured band gap for the 40 to 100% water content ranged from 3.36 to 3.34 eV, corresponding to a 0.9 to 0.4% difference respectively from the theoretical band gap of pure ZnO at 3.37 eV [58]. Thus, by utilizing water vapor plasma as the reactive gas, the shallow donor doping of H onto the ZnO occurs as supported by the low difference in E_g.

4.5 Effect of Substrate Bias

In magnetron sputtering, the energetic species present in the plasma are mainly released from the target surface and produced by ionization or excitation of the gas admixture. Specifically for oxides, highly energetic particles in the plasma can damage the film during deposition. This is detrimental to thin film properties, such as conductivity[21]. One method that prevents film damage and controls the incident ion energy is applying a substrate bias during deposition. By changing the incident ion energy, the film's structure and surface morphology can be controlled, and the damage to the film surface can be minimized [53, 54, 59]. Thus, the effect of the substrate bias on the near surface plasma characteristics, and its correlation to the film properties, were investigated for water vapor plasma.

4.5.1 Plasma Parameters

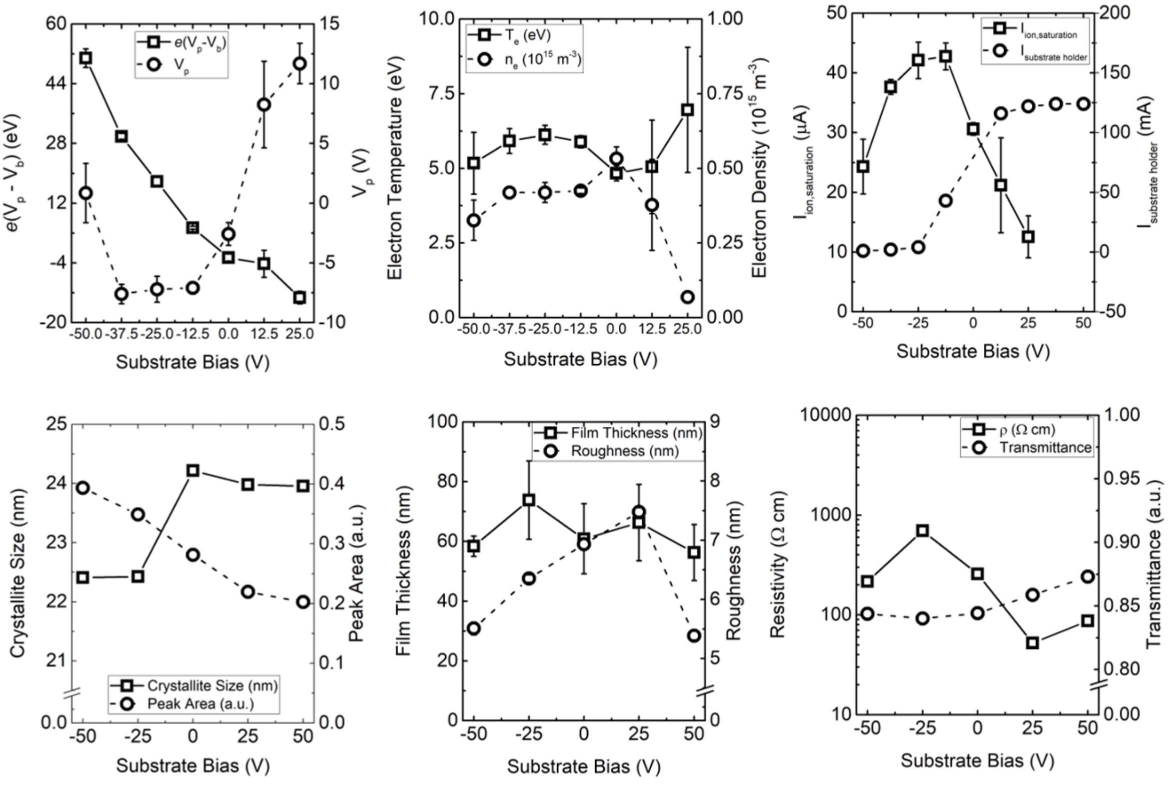

FIGURE 4.17: Effect of the substrate bias (-50 to 50 V) to the measured near surface plasma characteristics and the deposited film's properties.

As shown in Fig. 4.17, the trends in the plasma parameters are significantly affected by the polarity of the substrate bias. The substrate bias act as a potential barrier near the surface and this barrier is estimated by the difference of the plasma potential and substrate bias, $(V_p - V_b)$ [21, 23]. As shown in Fig. 4.17, a negative bias limits the electron flux to the surface, while a positive bias promotes the electron collection. This phenomenon is supported by the current measured at the substrate holder by the DC power supply. This behavior shifted V_p to a more negative potential at negative bias, which increased to positive values as the substrate bias became positive. As for the electron temperature, T_e, and the ion saturation current, $I_{ion,sat}$, a peak was observed at -25V and -12.5V, respectively. The electron density, n_e, increased as the substrate bias increased from -50V to 0V. These trends indicated that the electron confinement by the bias was effective at moderately negative substrate biases. Shifting to a higher negative bias would then reduce the electron populations and elevate the T_e, as more ion-electron interactions occur because the energy of electrons is sufficient to realize more ion-electron interactions and through the general repulsion from the substrate area due to the negative bias [23, 60]. The ions produced in these interactions measured were then collected through the negatively biased substrate or neutralization in the plasma and were reflected by the decreased $I_{ion,sat}$ at higher negative biases.

Conversely, at a positive bias, the electron collection realizes the electron bombardment on the growing film surface [61, 62]. As more electrons accelerate to the substrate, V_p increases to satisfy the current balance at the surface. This phenomenon shifted the Langmuir probe characteristic to higher potentials, particularly for the 37.5 and 50 V settings, and limited the analysis of plasma parameters up until the 25 V setting. This phenomenon also caused an increased T_e and lowered n_e, as the highly mobile electrons were accelerated and then collected at the substrate surface. Consequently, the formation of thin electron sheaths was not expected as the substrate holder size in the experiments was sufficiently large compared to the chamber walls [63].

4.5.2 Film Properties

Modifying the incident species towards the growing film will then change the film's primary growth mechanism. The negative bias increased the incident ion flux, which resulted in a higher peak area for (002) ZnO and the formation of more nucleation sites. Competing nucleation sites restrict the crystallite growth, causing a smaller crystallite size and a lower roughness [54, 64]. The resistivity, ρ, increased as well, as the oxygen vacancies in the ZnO structure decreased because of the higher incident reactive ion flux. Oxygen vacancies are linked with lower resistivities in ZnO films [56]. For positive biases, electron bombardment on the film decreased the (002) peak area and increased the crystallite size (Fig. 4.17). The effect of the impinging electrons was similar to allowing crystallite growth through additional thermal energy [65]. Together with the reduced ion flux, this increases the defect density in the deposited ZnO thin film. However, when a highly positive bias is applied, the excessive electron and negative ion bombardment can smooth the film surface or damage the film. This phenomenon reverses the trend for the ρ, as the damage decreases the film's ρ from 25 to 50 V. Irrespective of the bias, the transmittance of the film was relatively constant ($\approx$85%), and the band gap of the film was at 3.32 eV. The minimal change indicates that the bias can sufficiently change the film morphology and properties, but the shallow donor doping of H and the transparency are unaffected.

4.6 Effect of Substrate Heating

Another method for modifying the film's growth mechanism is substrate heating. By changing the temperature, the energy required for surface processes changes. This change is important for water vapor, as the molecule can sequentially adsorb and react with species present at the surface. By changing the temperature, the desorption from the surface and the energy required for the surface process are affected simultaneously. Thus, the effect of due to substrate heating on the deposition process involving water vapor needs investigation.

4.6.1 Ambient Heating from the Plasma

A K-type thermocouple measured the temperature at the substrate position (Fig. 4.18) to identify the effect of the ambient heating from the plasma with that of substrate heating. The substrate heating was quantified by fitting the heating curve to Eq. 4.18:

$$T(t) = T_{\infty}(1 - e^{\alpha^{+}(j(t))} \tag{4.18}$$

where T_{∞} is the saturation temperature, $j(t)$ is the current density collected at the area, and α^{+} is an arbitrary measure of the heating rate [66]. The α^{+} obtained varied from 0.0045 to 0.005, which indicates a similar heating rate irrespective of the plasma species. This trend indicates that the substrate region experiences a constant heat flux from the plasma at a given working pressure and discharge current. Thus, the effect of substrate heating is directly seen if the discharge parameters are kept constant.

4.6.2 Plasma Parameters

Shown in Fig. 4.19 are the plasma parameters and film properties of the deposited film at varying substrate temperatures. $(V_p - V_f)$ consistently decreases at higher substrate temperatures, while T_e decreased. V_p, n_e and $I_{ion,sat}$ peaked at 88^{o}C. By increasing the substrate temperature, the thickness of the adsorbed layer at the surface changed. Particularly for oxides, the energy requirements are balanced by ion recombination and the adsorption energy [67]. Initially, at temperatures below 88^{o}C, increased substrate heating promoted the desorption of water at the surface. The desorption produced a localized increase in ions near the surface. This layer interacts with the incident energetic particle flux and broadens the incident ion energy distribution at the surface [67]. These interactions increased the ions present near the surface, which elevated V_p, produced lower energy electrons reflected by n_e, and effectively lowered T_e. However, after a threshold temperature, the adsorption of water vapor at the surface was sufficiently inhibited, where further increasing the temperature now translated to film growth instead. This change is evidenced by the growth of other ZnO peaks after 88^{o}C (Fig. 4.20). The additional ions and electrons are now consumed for the film's growth, as seen with the decrease in n_e and $I_{ion,sat}$.

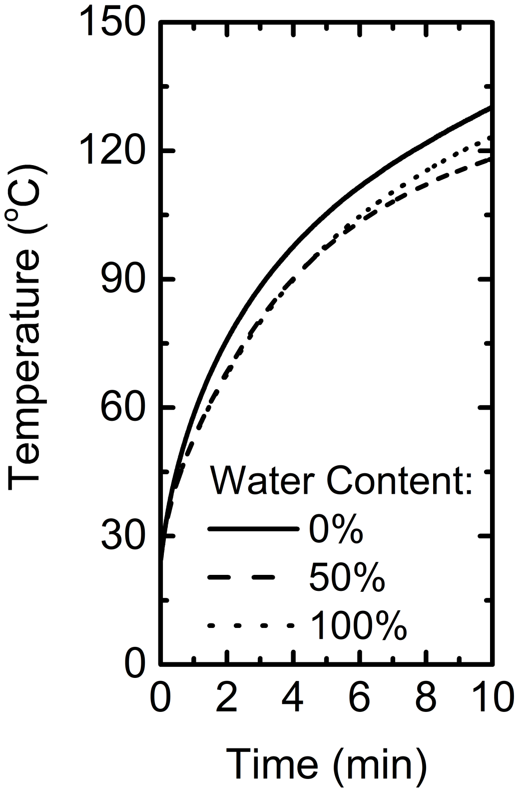

FIGURE 4.18: Ambient heating from the plasma as measured by a K-type thermocouple for a duration of 10 minutes, at varying water vapor content (0%, 50% and 100% water vapor content).

4.6.3 Film Properties

The effect of substrate heating was observed in the film's properties. The film thickness remained relatively constant and did not coincide with the increased ion density caused by the desorption of water vapor near the surface. The additional energy from substrate heating was converted instead into the evolution of other crystallographic orientations as shown in Fig. 4.20. The changes were highlighted by the trend of the (002) peak area and the crystallite size, where it directly coincided with the threshold temperature of 88^{o}C. Typically, higher substrate temperatures increase the peak area as surface atoms move smoothly with the larger mobility [68]. However, the evolution of other peak orientations were observed in Fig. 4.20 instead. The added peak orientations also increased the film's roughness. Accounting for the difference, the consistently decreasing ρ are attributed to the desorption of the reactive species at the film surface, such as oxygen from the surface of the growing ZnO film [69], instead of a diffusion-based annealing effect. This phenomenon means that the desorption behavior during deposition using water vapor plasma was linked to the resistivity of the deposited films. The transmittance (≈83.4%) and band gap (3.33 eV)of the film, however, were found to change minimally, which indicated that the shallow donor doping of the ZnO and its transparency were not affected and were stable at the temperature range investigated.

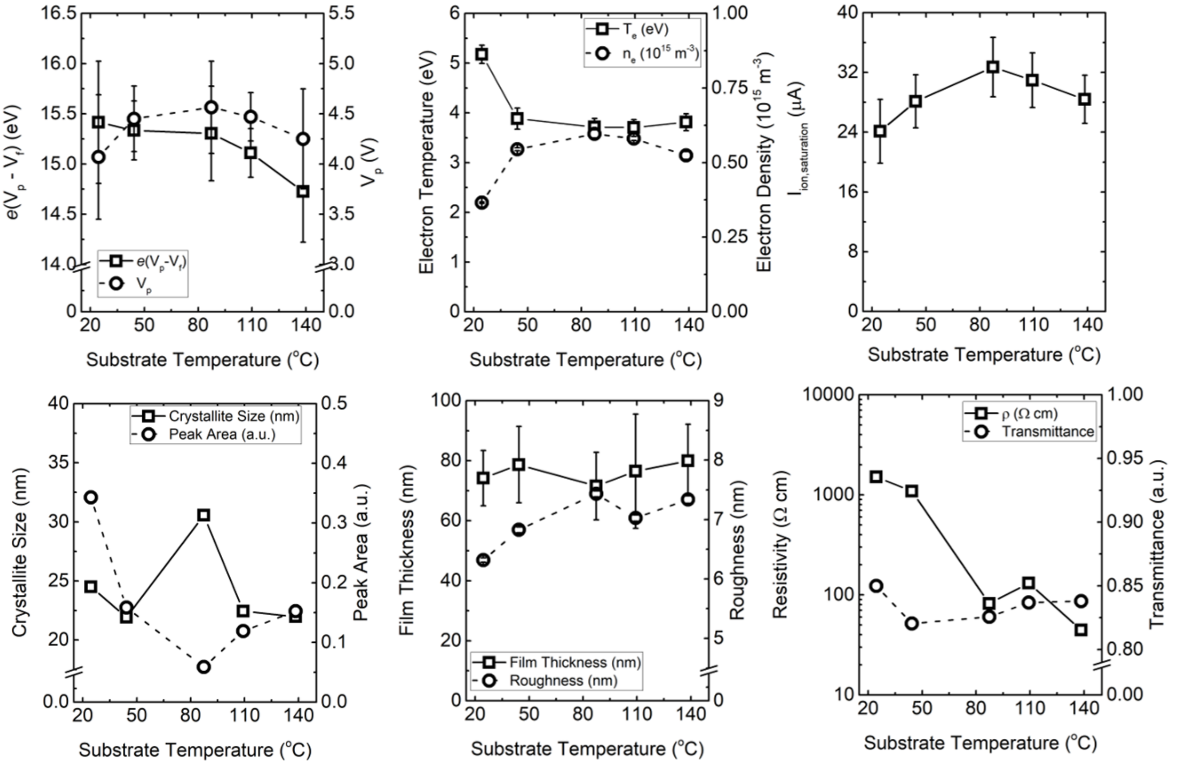

FIGURE 4.19: Effect of substrate temperature (20^o to 140^o C) to the measured near surface plasma characteristics and the deposited film's properties.

4.7 Summary of Results

ZnO thin films were deposited at varying water vapor content. The change in film properties related to transparent conductive electrodes was correlated to changes in the bulk and the near substrate surface plasma parameters obtained from a single Langmuir probe. The addition of water significantly changes the behavior of the plasma and can cause target poisoning which altered the dominant growth mechanism of the film. The transition between a mainly metallic Zn film to ZnO was observed at a water vapor content of 40% and coincided with a shift in the plasma parameters V_p, $(V_p - V_f)$, n_e, T_e, and $I_{ion,sat}$. Deposition at the 40% water content resulted to 1.20 Ωcm ρ, 87.5% T_{tr}, and 3.36 eV E_g. The measured E_g decreased 0.4% when compared with the theoretical value, confirming the shallow H donor doping phenomenon when water vapor plasma was utilized. As the shift in film properties was closely related to changes in the trend of the plasma parameters as the water vapor content increased, monitoring the plasma parameters during the deposition can also allow us to estimate the quality of the formed film

The ZnO deposition at varying substrate bias and substrate temperatures was investigated. The polarity of the substrate bias changed the incident charged species, while the bias magnitude affected the energy. The film characteristics were linked directly to the ion and electron flux to the surface. The shallow donor doping (3.32 eV) and optical transparency of the films (≈85%) were unaffected by the substrate bias. When substrate heating is employed, the

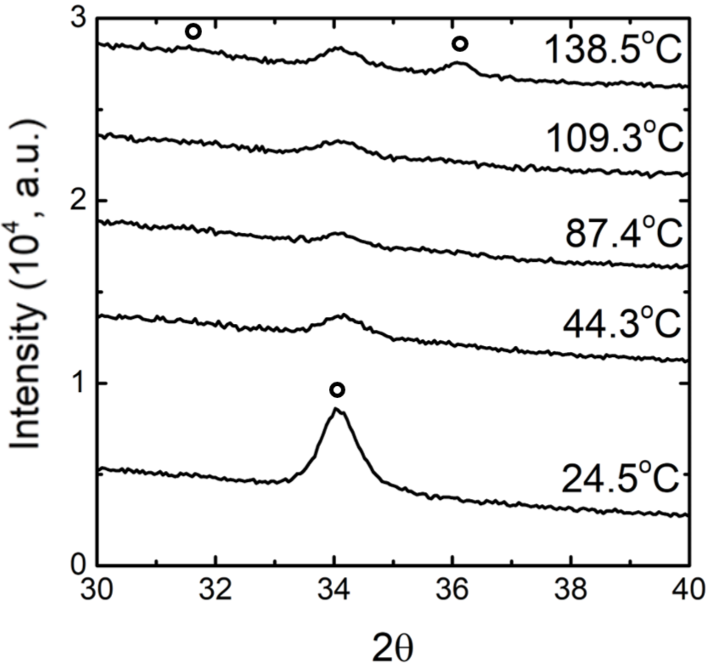

FIGURE 4.20: The XRD peaks ((100), (002) and (101)) of ZnO films deposited at varying substrate temperatures. The working pressure is kept at 1.0 Pa of water vapor, and 100 mA discharge.

adsorption behavior of water becomes an important consideration. Increasing the substrate temperature resulted in a localized increase in ions near the surface, and crossing a threshold temperature resulted in the promotion of film growth as observed at both the plasma and film characteristics. The peak growth other than at (002) was preferred with higher temperatures, while ρ consistently decreased. The trend was attributed to the desorption from the film surface. The band gap (3.33 eV) and transparency were relatively constant as the deposition temperature increased, which indicated that the shallow donor doping of ZnO for films deposited using water vapor plasma was stable for the 20^o to 140^{o}C range.

References

[1] C. G. V. D. Walle, "Hydrogen as a cause of doping in zinc oxide," *Physical Review Letters*, vol. 85, 1012–1015, 5 2000.

[2] C. G. V. de Walle, "Hydrogen as a shallow center in semiconductors and oxides," *Physica Status Solidi (B) Basic Research*, vol. 235, 89–95, 1 Jan. 2003.

[3] H. Lee, W. Jin, M. Ovhal, N. Kumar, and J. Kang, "Flexible transparent conducting electrodes based on metal meshes for organic optoelectronic device applications: A review," *Journal of Materials Chemistry C*, vol. 7, 1087–1110, 5 2019.

[4] A. Berman, "Water vapor in vacuum systems," *Vacuum*, vol. 47, 327–332, 4 1996.

[5] K. Jousten, "Thermal outgassing," *CAS 2006 - CERN Accelerator School: Vacuum in Accelerators, Proceedings*, 87–116, 1 2007.

[6] R. Grinham and A. Chew, "A review of outgassing and methods for its reduction," *Applied Science and Convergence Technology*, vol. 26, 95–109, 5 2017.

[7] N. Hershkowitz, "How langmuir probes work," in *Plasma Diagnostics*, O. Auciello and D. Flamm, Eds., Elsevier, 1989, 113–183.

[8] M. A. Lieberman and A. J. Lichtenberg, *Principles of Plasma Discharges and Materials Processing*, Second Edition. Wiley-Interscience, 2005.

[9] F. F. Chen, *Introduction to Plasma Physics and Controlled Fusion*, Third Edition. Springer International Publishing, 2016.

[10] P. M. Bellan, *Fundamentals of plasma physics*. 2006, vol. 9780521821, 1–609.

[11] F. F. Chen, "Lecture notes on langmuir probe diagnostics," 2003, 42.

[12] H. Mott-Smith and I. Langmuir, "The theory of collectors in gaseous discharges," *Physical Review*, vol. 28, 727–763, 1926.

[13] M. Usoltceva, E. Faudot, S. Devaux, S. Heuraux, J. Ledig, G. V. Zadvitskiy, R. Ochoukov, K. Crombé, and J. M. Noterdaeme, "Effective collecting area of a cylindrical langmuir probe in magnetized plasma," *Physics of Plasmas*, vol. 25, 6 2018.

[14] X. Wang, Q. Li, Z. Chen, W. Wang, C. Xie, J. Wang, Q. Gao, W. Peng, X. Geng, and G. Luo, "A newly designed actively water-cooled langmuir probe for tokomak devices," *Review of Scientific Instruments*, vol. 90, 10 2019.

[15] T. L. Thomas and E. L. Battle, "Effects of contamination on langmuir probe measurements in glow discharge plasmas," *Journal of Applied Physics*, vol. 41, 3428–3432, 8 1970.

[16] E. P. Szuszczewicz and J. C. Holmes, "Surface contamination of active electrodes in plasmas: Distortion of conventional langmuir probe measurements," *Journal of Applied Physics*, vol. 46, 5134–5139, 12 1975.

[17] K. I. Oyama and K. Hirao, "Inaccuracies in electron density estimates due to surface contamination of langmuir probes," *Planetary and Space Science*, vol. 24, 87–89, 1 1976.

[18] E. V. Shun'ko, "Influence of different langmuir probe surface cleaning procedures on its i-v characteristics," *Review of Scientific Instruments*, vol. 63, 2330–2331, 4 1992.

[19] R. Merlino, “Understanding langmuir probe current-voltage characteristics,” *American Journal of Physics*, vol. 75, 1078–1085, 12 2007.

[20] K. Ellmer and R. Wendt, “D.c. and r.f.(reactive) magnetron sputtering of zno:al films from metallic and ceramic targets: A comparative study,” *Surface and Coatings Technology*, vol. 93, 21–26, 1997.

[21] K. Ellmer and T. Welzel, “Reactive magnetron sputtering of transparent conductive oxide thin films: Role of energetic particle (ion) bombardment,” *Journal of Materials Research*, vol. 27, 765–779, 5 2012.

[22] J. R. Conrad, “Sheath thickness and potential profiles of ion-matrix sheaths for cylindrical and spherical electrodes,” *Journal of Applied Physics*, vol. 62, 777–779, 3 1987.

[23] S. H. Seo and H. Y. Chang, “Electron transport in the downstream region of planar unbalanced magnetron discharge,” *Journal of Applied Physics*, vol. 96, 1310–1317, 3 2004.

[24] T. E. Sheridan, M. J. Goeckner, and J. Goree, “Observation of two-temperature electrons in a sputtering magnetron plasma,” *Journal of Vacuum Science and Technology A: Vacuum, Surfaces, and Films*, vol. 9, 688–690, 3 May 1991.

[25] B. B. Sahu, J. G. Han, H. R. Kim, K. Ishikawa, and M. Hori, “Experimental evidence of warm electron populations in magnetron sputtering plasmas,” *Journal of Applied Physics*, vol. 117, 0–9, 3 2015.

[26] V. Godyak and V. Demidov, “Probe measurements of electron-energy distributions in plasmas: What can we measure and how can we achieve reliable results?” *Journal of Physics D: Applied Physics*, vol. 44, 233001–1–233001–30, 2011.

[27] B. B. Sahu, J. G. Han, M. Hori, and K. Takeda, “Langmuir probe and optical emission spectroscopy studies in magnetron sputtering plasmas for al-doped zno film deposition,” *Journal of Applied Physics*, vol. 117, 2 2015.

[28] G. Yin, S. Gao, Z. Liu, and Q. Yuan, “The discharge characteristics of low-pressure capacitively coupled argon plasma with langmuir probe,” *Physics Letters, Section A: General, Atomic and Solid State Physics*, vol. 426, 2022.

[29] H. Andrei, V. Covlea, V. V. Covlea, and E. Barna, “The smoothing and the digital processing of langmuir probe characteristic,” *Romanian Reports in Physics*, vol. 55, 51–56, 2 2003.

[30] J. F. Palop, J. Ballesteros, V. Colomer, and M. Hernandez, “A new smoothing method for obtaining the electron energy distribution function in plasmas by the numerical differentiation of the IV probe characteristic,” *Review of Scientific Instruments*, vol. 66, 4625–4636, 1995.

[31] A. Caldarelli, F. Filleul, R. W. Boswell, C. Charles, N. J. Rattenbury, and J. E. Cater, “Data processing techniques for ion and electron-energy distribution functions,” *Physics of Plasmas*, vol. 30, 4 Apr. 2023.

[32] E. S. Ameh, “A review of basic crystallography and x-ray diffraction applications,” *International Journal of Advanced Manufacturing Technology*, vol. 105, 3289–3302, 7-8 Dec. 2019.

[33] A. Ali, Y. W. Chiang, and R. M. Santos, "X-ray diffraction techniques for mineral characterization: A review for engineers of the fundamentals, applications, and research directions," *Minerals*, vol. 12, 2 Feb. 2022.

[34] E. Chason and T. M. Mayer, "Thin film and surface characterization by specular x-ray reflectivity," *Critical Reviews in Solid State and Materials Sciences*, vol. 22, 1–67, 1 1997.

[35] M. Yasaka, "X-ray thin-film measurement techniques v. x-ray reflectivity measurement," *The Rigaku Journal*, vol. 26, 1–9, 2010.

[36] V. Mandic, S. Kurajica, I. Panzic, A. Bafti, J. Sipusic, K. Muzina, F. Brlekovic, L. Gigli, and M. Gaboardi, "Utilization of conventional pxrd apparatus for characterization of thin-films using reconsidered equations for xrr," *Surfaces and Interfaces*, vol. 36, 2023.

[37] M. Smits, "Measurement of sheet resistivities with the four-point probe," *The Bell System Technical Journal*, vol. 37, 711–718, 3 1958.

[38] J Tauc, R Grigorovici, and A Vancu, "Optical properties and electronic structure of ge optical properties and electronic structure of amorphous germanium," *phys. stat. sol*, vol. 15, 627, 1966.

[39] S. T. Tan, B. J. Chen, X. W. Sun, W. J. Fan, H. S. Kwok, X. H. Zhang, and S. J. Chua, "Blueshift of optical band gap in zno thin films grown by metal-organic chemical-vapor deposition," *Journal of Applied Physics*, vol. 98, 1 2005.

[40] A. Faramawy, H. Elsayed, C. Scian, and G. Mattei, "Structural, optical, magnetic and electrical properties of sputtered zno and zno:fe thin films: The role of deposition power," *Ceramics*, vol. 5, 1128–1153, 4 2022.

[41] N. S. J. Braithwaite, "Introduction to gas discharges," *Plasma Sources Science and Technology*, vol. 9, 517–527, 4 2000.

[42] E. Muschlitz and T. Bailey, "Negative ion formation in hydrogen peroxide and water vapor. the perhydroxide ion," *Journal of Physical Chemistry*, vol. 60, 681–684, 5 1956.

[43] M. Zeuner, H. Neumann, J. Zalman, and H. Biederman, "Sputter process diagnostics by negative ions," *Journal of Applied Physics*, vol. 83, 5083–5086, 10 1998.

[44] K. Lykke, K. Murray, and W. Lineberger, "Threshold photodetachment of h," *Physical Review A*, vol. 43, 6104–6107, 1991.

[45] D. Neumark, K. Lykke, T. Andersen, and W. Lineberger, "Laser photodetachment measurement of electron affinity of atomic oxygen," *Physical Review A*, vol. 32, 1890–1892, 1985.

[46] F. Goldfarb, C. Draf, W. Chaibi, S. Kroger, C. Blondel, and C. Delsart, "Photodetachment microscopy of the p, q, and r branches of the oh to oh detachment threshold," *The Journal of Chemical Physics*, vol. 122, 2004.

[47] C. Melton, "Cross sections and interpretation of dissociative attachment reactions producing oh, o, and h in h2o," *The Journal of Chemical Physics*, vol. 57, 4218–4225, 2003.

[48] R. Dodd, S. You, P. Bryant, and J. Bradley, "Negative ion density measurements in reactive magnetron sputtering," *Plasma Processes and Polymers*, vol. 6, S615–S619, 2009.

[49] P. Pokorny, M. Misina, J. Bulir, J. Lancok, P. Fitl, J. Musil, and M. Novotny, "Investigation of the negative ions in ar o2 plasma of magnetron sputtering discharge with al:zn target by ion mass spectrometry," *Plasma Processes and Polymers*, vol. 8, 459–464, 2011.

[50] P. Poolcharuansin, A. Chingsungnoen, N. Pasaja, M. Horprathum, and J. Bradley, "Measurement of negative ion fluxes during dc reactive magnetron sputtering of ti in ar/o2 atmosphere using a magnetic-filtering probe," *Vacuum*, vol. 194, 110549, 2021.

[51] T. Welzel and K. Ellmer, "Comparison of ion energies and fluxes at the substrate during magnetron sputtering of zno: Al for dc and rf discharges," *Journal of Physics D: Applied Physics*, vol. 46, 31 2013.

[52] K. Strijckmans, R. Schelfhout, and D. Depla, "Tutorial: Hysteresis during the reactive magnetron sputtering process," *Journal of Applied Physics*, vol. 124, 24 2018.

[53] J. E. Greene, J. E. Sundgren, L. Hultman, I. Petrov, and D. B. Bergstrom, "Development of preferred orientation in polycrystalline tin layers grown by ultrahigh vacuum reactive magnetron sputtering," *Applied Physics Letters*, vol. 67, 2928, 1995.

[54] I. Petrov, P. B. Barna, L. Hultman, and J. E. Greene, "Microstructural evolution during film growth," *Journal of Vacuum Science and Technology A: Vacuum, Surfaces, and Films*, vol. 21, S117–S128, 5 2003.

[55] D. L. Raimondi and E. Kay, "High resistivity transparent zno thin films," *Journal of Vacuum Science and Technology*, vol. 7, 96–99, 1 1970.

[56] A. Janotti and C. V. D. Walle, "Oxygen vacancies in zno," *Applied Physics Letters*, vol. 87, 1–3, 12 2005.

[57] K. Ellmer, A. Klein, and B. Rech, *Transparent conductive zinc oxide : basics and applications in thin film solar cells*. Springer, 2008.

[58] A. Janotti and C. V. D. Walle, "Fundamentals of zinc oxide as a semiconductor," *Reports on Progress in Physics*, vol. 72, 12 2009.

[59] J. Williams, H. Furukawa, Y. Adachi, S. Grachev, E. Sondergard, and N. Ohashi, "Polarity control of intrinsic zno films using substrate bias," *Applied Physics Letters*, vol. 103, 4 2013.

[60] K. Bobzin, T. Brögelmann, N. C. Kruppe, and M. Engels, "Investigations on the substrate bias influence on reactive hppms plasmas," *Thin Solid Films*, vol. 663, 62–72, Oct. 2018.

[61] H. Nadhom, D. Lundin, P. Rouf, and H. Pedersen, "Chemical vapor deposition of metallic films using plasma electrons as reducing agents," *Journal of Vacuum Science and Technology A*, vol. 38, 033402, 3 May 2020.

[62] L. Schiesko, M. Carrère, G. Cartry, and J. M. Layet, "Positive sheath behaviour in low pressure argon plasma," *Journal of Nuclear Materials*, vol. 363-365, 1016–1020, 1-3 Jun. 2007.

[63] B. T. Yee, B. Scheiner, S. D. Baalrud, E. V. Barnat, and M. M. Hopkins, "Electron presheaths: The outsized influence of positive boundaries on plasmas," *Plasma Sources Science and Technology*, vol. 26, 2 2017.

[64] W. Tillmann, D. Kokalj, D. Stangier, Q. Fu, and F. Kruis, "Bias-voltage effect on the tin nanoparticle injection into magnetron sputtered crn thin films towards nc-tin/nc-crn composites," *Applied Surface Science Advances*, vol. 6, 2021.

[65] A. Karuppasamy and A. Subrahmanyam, “Effect of electron bombardment on the properties of zno thin films,” *Materials Letters*, vol. 61, 1256–1259, 4-5 Feb. 2007.

[66] V. Shapovalov, A. Komlev, A. Bondarenko, P. Baykov, and V. Karzin, “Substrate heating and cooling during magnetron sputtering of copper target,” *Physics Letters, Section A: General, Atomic and Solid State Physics*, vol. 380, 882–885, 7-8 2016.

[67] H. Kersten, H. Deutsch, H. Steffen, G. M. Kroesen, and R. Hippler, “The energy balance at substrate surfaces during plasma processing,” *Vacuum*, vol. 63, 385–431, 3 2001.

[68] N. W. Schmidt, T. S. Totushek, W. A. Kimes, D. R. Callender, and J. R. Doyle, “Effects of substrate temperature and near-substrate plasma density on the properties of dc magnetron sputtered aluminum doped zinc oxide,” *Journal of Applied Physics*, vol. 94, 5514–5521, 9 Nov. 2003.

[69] H. Watanabe, M. Wada, and T. Takahashi, “The activation energy for oxygen desorption from zinc oxide surfaces,” *Japanese Journal of Applied Physics*, vol. 4, 1965.

Chapter 5

ION FORMATION OF WATER VAPOR PLASMA IN REACTIVE MAGNETRON SPUTTERING

5.1 Introduction

The generation of positive and negative species in the plasma has significant implications for its behavior at both the substrate and target regions. The amount of reactive ions determines the target poisoning phenomena at the target surface [1]. In the film formation process, controlling the positive ion species and energy incident on the film allows for the modification of the film structure [2]. On the other hand, the negative ions in the plasma are detrimental to the film formation process because ions can be accelerated by the target cathode voltage to sufficiently high energies that damage the film [3, 4]. In this chapter, the bulk plasma characteristics were explored with water vapor as the reactive gas in a reactive magnetron sputtering process. The positive species were identified using optical emission spectroscopy, and the positive and negative ion energies incident onto the substrate region were measured using a retarding potential analyzer.

5.1.1 Reactive Characteristics of Water Vapor Plasma

The water molecule can interact with energetic species in the plasma and produce multiple reaction products. Shown in Fig. 5.1 are the cross-sections of the water molecule with electrons as the incident particle [5–7]. The two major reaction pathways for the water are electron impact ionization and electron attachment. Electron impact ionization produces positive ions in the plasma, as shown in Fig. 5.1a, while electron attachment produces negative ions, as shown in Fig. 5.1b. The reaction mechanisms are detailed in Table 5.1

TABLE 5.1: The electron impact ionization and electron attachment reactions for the water molecule. Argon is shown for comparison. [5–7]

Electron Impact Ionization	Dissociative Electron Attachment
$e^- + H_2O \rightarrow 2e^- + H_2O^+$	$e^- + H_2O \rightarrow H_2O^-$
$e^- + H_2O \rightarrow 2e^- + H^+ + OH$	$e^- + H_2O \rightarrow H^- + OH$
$e^- + H_2O \rightarrow 2e^- + H + OH^+$	$e^- + H_2O \rightarrow H + OH^-$
$e^- + H_2O \rightarrow 2e^- + 2H + O^+$	$e^- + H_2O \rightarrow 2H + O^-$
$e^- + H_2O \rightarrow 2e^- + O + H_2^+$	
(Ar): $e^- + Ar \rightarrow 2e^- + Ar^+$	

These cross-sections indicate that using water vapor can simultaneously realize the production of positive and negative ions in the plasma. The energy requirements for positive and negative ion formation are sufficiently close to the ionization of Ar, which was used as the discharge support gas in the admixtures. Thus, it is highly probable that these ions are formed

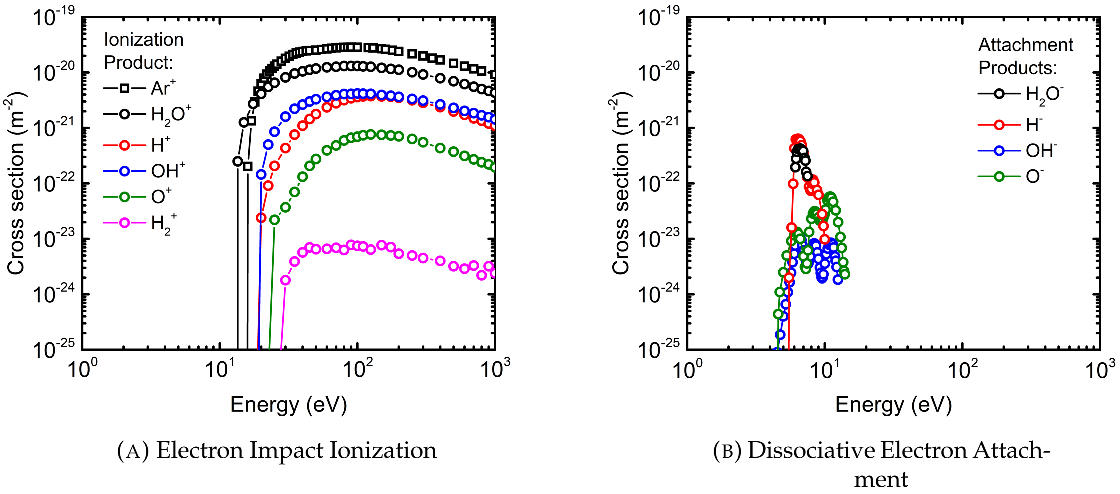

(A) Electron Impact Ionization

(B) Dissociative Electron Attachment

FIGURE 5.1: The electron impact ionization and dissociative electron attachment cross sections for the H_2O molecule and Ar [5–7]. The dissociative electron attachment for H_2O^- does not account for rotovibrational states.

in the bulk plasma at appreciable densities. This chapter details the detection of these positive and negative ions in the bulk plasma.

5.2 Experimental System

As shown in Fig. 5.2, the experiments were performed using DC reactive magnetron sputtering system similar to what was discussed previously in Chapter 4. The positive ions were identified using optical emission spectroscopy, and the energy of positive and negative ions in the plasma was measured using a retarding potential analyzer.

5.2.1 Optical Emission Spectroscopy

Optical emission spectroscopy (OES) is a common characterization technique for low-temperature plasma suitable for film deposition. For reactive plasma, the method allows for the identification of the excited species present based on its unique spectra, as well as measure the local plasma parameters and relative concentrations with minimal disturbance of the plasma [8–10].

The atomic spectra of a specific element are determined by the electronic transition of the excited state to the ground state. The emitted wavelength (λ) is dependent on the energy difference of the transition through the relation:

$$E_\lambda = \frac{hc}{\lambda} \tag{5.1}$$

where h is Planck's constant and c is the speed of light. As only certain transitions are allowed, the wavelength of the emitted photons determines the excited species. The intensity of emitted wavelength can be used to determine the plasma parameters if the plasma is considered to be in local thermal equilibrium. The intensity of each transition I_j, assuming a Boltzmann

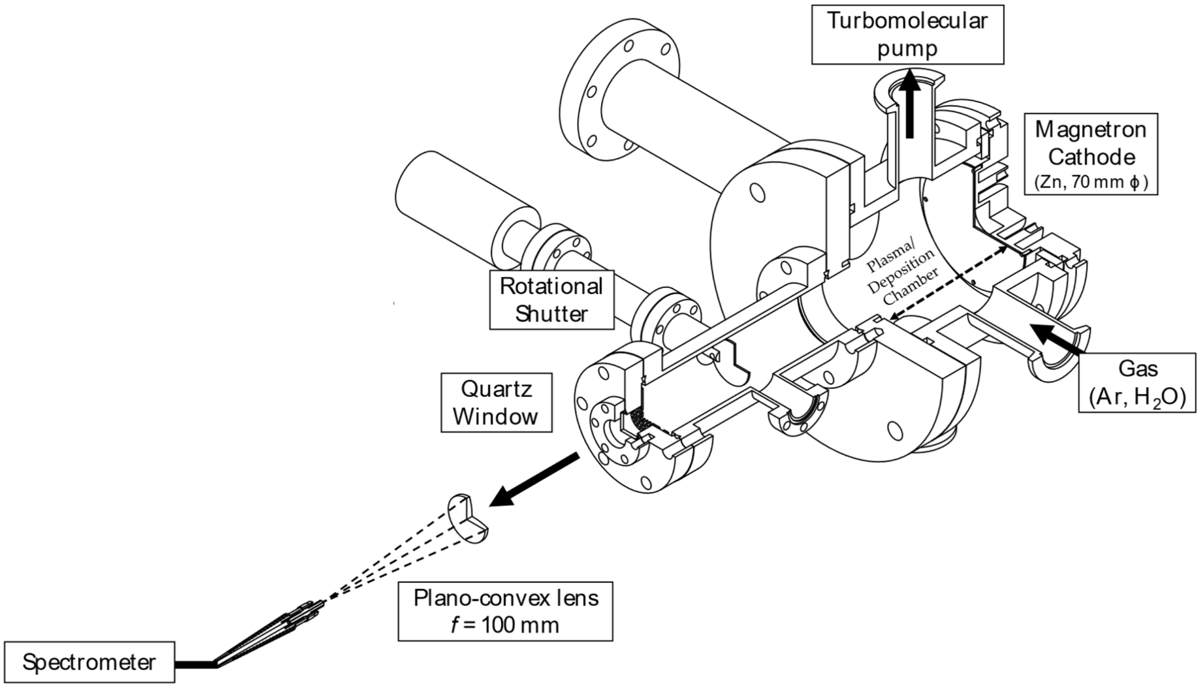

FIGURE 5.2: The experimental system in the optical emission spectroscopy measurement configuration

distribution for the possible states:

$$I_j = N_0 \frac{A_j g_j \mathrm{e}^{\frac{-E_j}{k_B T_e}}}{\sum_{j=0}^{\infty} g_j \mathrm{e}^{\frac{-E_j}{k_b T_e}}} \tag{5.2}$$

where N_0 is the total number of atoms considered, g_j is the degeneracy of the upper levels, A_j is the Einstein coefficient and E_j is the upper energy level. The denominator is the partition function which normalizes throughout the population of states [11, 12]. When a molecule is considered, the transition becomes more complex, as described by the Born-Oppenheimer approximation:

$$E_j = E_{elec} + E_{rot} + E_{vib} \tag{5.3}$$

This relation is a consequence of the possible molecular rotational and vibrational excitation modes. These excitation modes result in the formation of band spectra, where multiple fine lines of excitation are grouped [11, 13, 14]. At low spectrometer resolution, these band spectra are convoluted peaks consisting of rotational-vibrational bands.

5.2.1.1 Experimental Configuration and Analysis

Optical emission spectroscopy (OES) of the plasma was carried out using a USB spectrometer (400-1000 nm: OceanOptics, USB4000, 200nm-500nm: OceanOptics, Flame) at a normal incidence from the magnetron cathode axis (Fig. 5.2). A fused silica window and a plano-convex lens (focal length = 100 mm) were used and positioned 240 mm away from the target surface. A shutter mechanism mounted onto a rotational flange was employed to minimize

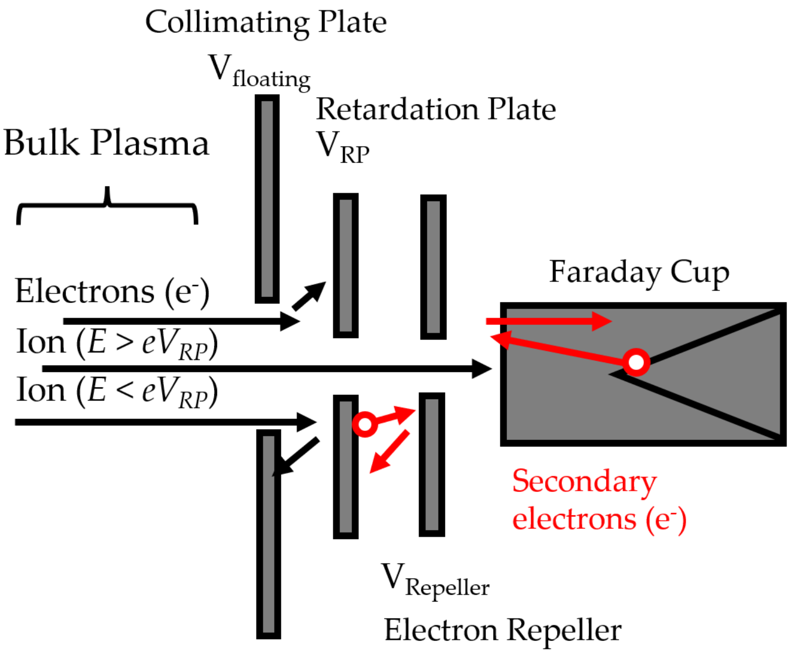

FIGURE 5.3: The mechanism for a triple-plate retarding potential analyzer to measure the ion energy distribution of plasma

and prevent the deposition of a film onto the window surface. The spectra were taken with a 200 ms integration time after sustaining the discharge for a 1-minute duration. The discharge current and pressure were fixed at 100 mA and 1.0 Pa, respectively, for the measurements.

5.2.2 Retarding Potential Analyzer

The ion energies in the bulk plasma were measured using a retarding potential analyzer (RPA). Shown in Fig. 5.3 is the mechanism of the RPA. In its most basic form, the RPA filters the incoming ions based on their energy using the potential of a retardation plate or grid. The current at the detector of the RPA can be expressed as in Eq. 5.4:

$$I = qnA \int_{v_{min}}^{\infty} v f(v) dv \tag{5.4}$$

where v_{min} is the minimum velocity required to pass through the retardation plate voltage. The ion velocity was transformed into the voltage applied on the plate ($\frac{1}{2}mv^2 = qE$), and taking the derivative will yield the Eq. 5.5:

$$\frac{dI}{dV} = -nq^2 A \sqrt{\frac{2qV}{m}} f(E) \tag{5.5}$$

For multiple species plasma, the shape of the first derivative is directly proportional to the energy distribution in the plasma ($-\frac{dI}{dV} \propto f(E)$) [15–17]. The detailed derivation of the relation of the energy distribution to the derivative of the RPA current is shown in App. B.

5.2.2.1 Experimental Configuration and Analysis

The experimental configuration and measurement circuit is shown in Fig. 5.4. A triple plate configuration consisting of a grounded collimating mesh plate, retardation plate, and electron repeller plate over a fully grounded Faraday cup was used for the positive and negative ion measurements. The mesh (Nilaco, SUS304 (100 mesh, 154 μm)) decreased the aperture opening to lengths sufficiently lower than that of the Debye shielding length and prevented the bleeding in of the plasma towards the retardation plate electrode as the configuration was immersed in the deposition plasma. The retardation voltage was powered by a high-speed power amplifier (-40 V to 40 V sweep: NF Electronic Instruments, NF4020, -450 V to -50 V sweep: Kepco, BOP 1000 M) driven by a 10 Hz ramp waveform from a function generator (EZ Digital DFG6020).

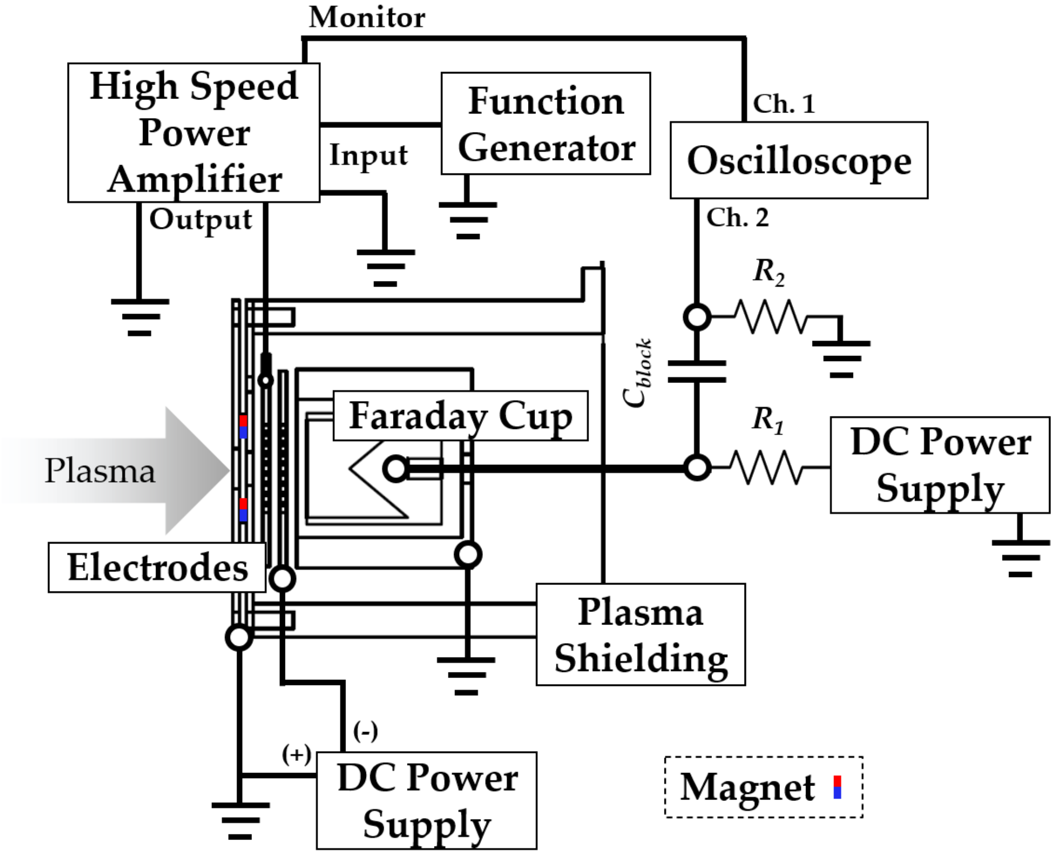

FIGURE 5.4: The retarding potential analyzer (RPA) schematic used for ion energy distribution measurements of the reactive magnetron sputtering plasma containing water vapor.

The electron current contribution was significantly high at the substrate region as directly measured by a Faraday cup. Three filters were added to the conventional triple plate configuration to minimize this and improve the sensitivity to the ion current. A magnet filter ($\approx$ 500 G) at the collimating mesh-plate aperture minimized the penetration of low-energy electrons guided by the magnetron magnetic field. Then, an electron repeller bias of -10 V decreased the secondary electrons collected from the energetic species that hit the retardation plate. The voltage was selected from the onset of the linear behavior of the RPA current when the repeller voltage was swept while the retardation voltage was at the ground potential. By choosing the onset point, the acceleration of the ions between the plates was minimized. Lastly, to prevent the reflection of the incident species and minimize the production of secondary electrons from the Faraday cup surface, a bias voltage was directly applied to the Faraday cup. This voltage was at -50 V for positive ions and +50 V for negative ion measurements. These voltages were selected such that the electron contribution to the Faraday cup was minimized and did not significantly alter the shape of the current distribution.

The detection circuit for measurement of the ion current consisted of a blocking capacitor as shown in Fig. 5.4, and was similar to the measurement circuit used in laser photodetachment measurements [18]. This configuration allowed for high sensitivity detection even at sufficiently high Faraday cup bias voltages. R_1, R_2 and C_{block} were 100 kΩ, 200 Ω, and 500 nF, respectively. The sweep frequency was chosen such that the attenuation and phase shift were both minimal. The attenuation and phase shift (2.05 μs, $\approx$-4.1 dBM at 10 Hz) by the circuit was considered for all ion current measurements. The ion current was measured using a low noise preamplifier (NF Instruments, LI75A, 200x gain)-oscilloscope (Iwatsu, DS-5424, 500 kS 1 MΩ - DC) and oscilloscope (Iwatsu, DS-5424, 500 kS 1 MΩ - DC) for the positive and negative ion measurements, respectively. Smoothing of the current data using a Savitzky-Golay filter for both positive and negative ion measurements were performed to improve the signal-to-noise ratio [19].

5.3 Optical Emission Spectroscopy of Water Vapor Plasma

Shown in Fig. 5.5 are the spectra obtained at varying water vapor content at the visible and UV regions, respectively. In the visible region, the species directly observed were from a reactive gas, H^+ (H_α, H_β, and H_γ) and O I (777 nm and 844 nm), the sputtered metal, Zn I (481 nm and 632 nm), and from the discharge support gas, the characteristic Ar I peaks (Three highest intensities: 750 nm, 763 nm, and 811 nm) [20]. The O I peaks were significantly weak in intensity and could be distinctly seen only at sufficiently high water vapor content (80 to 100% settings). In contrast, the H peak intensities can be easily observed even at the 20% water vapor content setting.

In the UV region, the main peaks are from the reactive gas, OH (OH ($A^2\Sigma^+ \rightarrow X^2\Pi$, 286 nm, and 310 nm) and H (H_β), and from the metal, Zn I (213 nm and 307 nm) [20, 21]. As the band spectra of OH is significantly broad, the atomic line of Zn I at 307 nm becomes obscure in the spectrum starting from the 20% water vapor content setting. The specific transitions of OH are difficult to identify, as the spectrometer resolution ($\approx$ 0.18 nm) was too low to detect the fine structure of the OH ($A^2\Sigma^+ \rightarrow X^2\Pi$) band.

5.3.1 The Effect of Water Vapor Content

Given the reactive nature of the plasma and the strong magnetic field present at the target surface, the assumption of the local thermal equilibrium to obtain the plasma parameters is erroneous. Thus, the ion intensity ratio to a fixed species, Zn I in this case, was used to identify the behavior of the positive ion species that were detected.

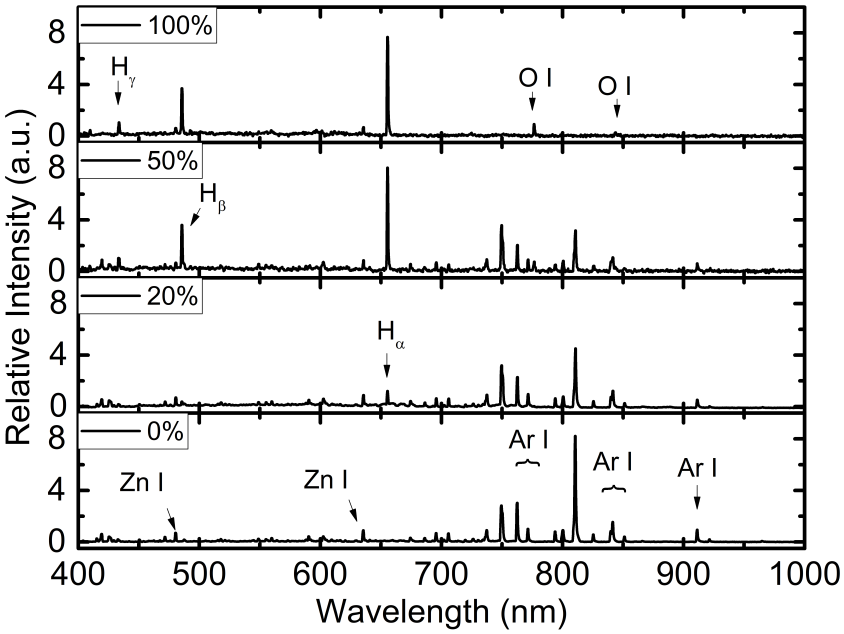

(A) Visible Range (400-1000 nm)

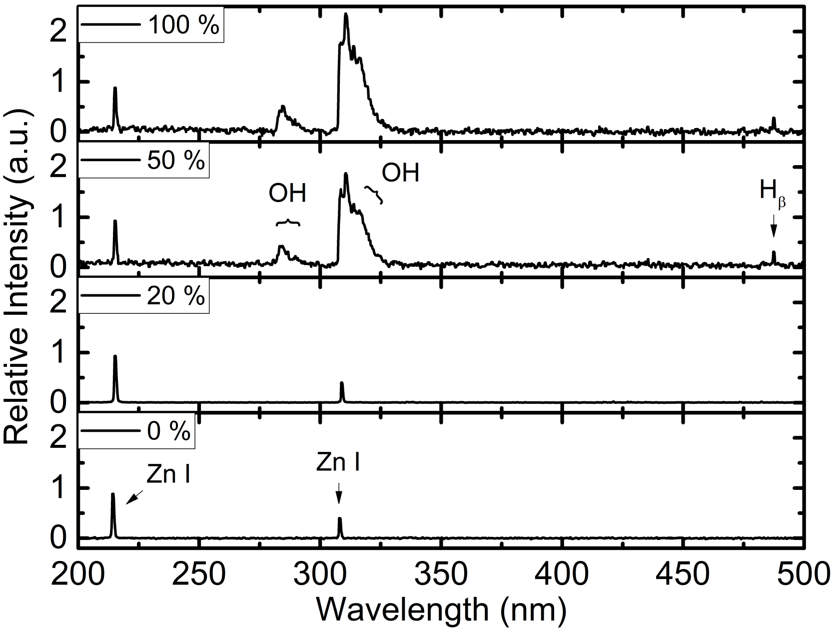

(B) UV Range (200-500 nm)

FIGURE 5.5: The optical emission spectra at the visible range (400-1000 nm) and UV range (200-500 nm) at varying water vapor content

From the peak ratios in Fig. 5.6a and 5.6b, a shift in the relative intensity trend at the 40% setting was observed. For the Ar I peaks, the decrease was nonlinear. The minima for Ar-containing plasma occurred at 40%, while for the H ions, the increase was nonlinear and the 40% setting corresponded to a sharp increase in the intensity followed by a saturation level as the water content was further increased. This change could indicate the water vapor content

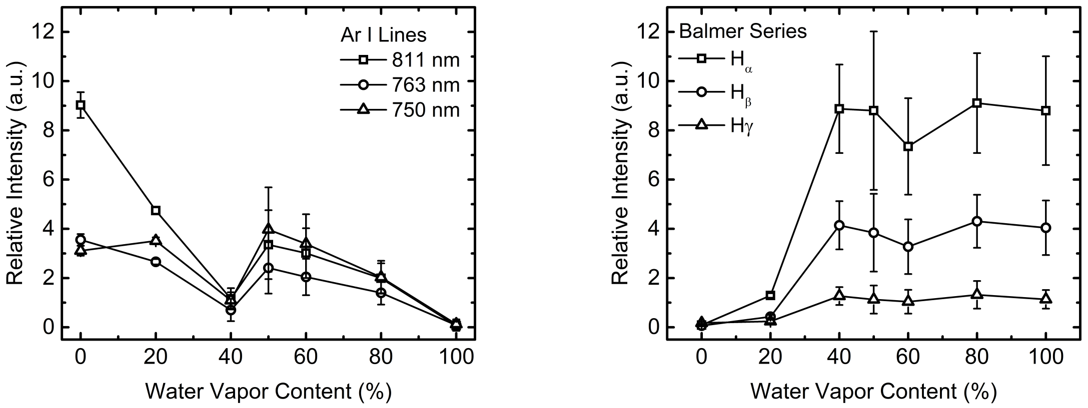

(A) Ar I Peaks

(B) H (Balmer Series) Peaks

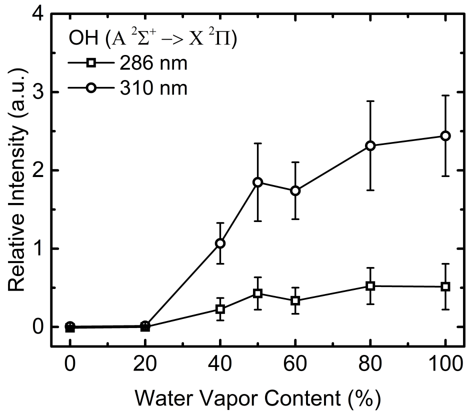

(C) OH ($A^2\Sigma^+ \rightarrow X^2\Pi$)

FIGURE 5.6: The OES peak intensity ratios of Ar I, H (Balmer Series), and OH ($A^2\Sigma^+ \rightarrow X^2\Pi$) at varying water vapor content. The Ar I and H intensity ratios were taken at the visible wavelength region (400-1000 nm) and the OH band spectra was taken at the UV wavelength region (200-500 nm).

where the ZnO formation rate was the highest, as the discharge support gas was utilized sufficiently to ionize the reactive gas and form the compound. This observation was supported by the trend for the OH band spectra, as the 40% setting was the onset of the increasing trend of the relative intensity ratio.

5.4 Ion Energy Measurements of Water Vapor Plasma

The ion energy was measured to see if there were any fundamental shifts in the energy balance and fundamental processes in the bulk plasma similar to what was measured in the relative intensities obtained using OES. The energy distribution was measured using the RPA for both the negative and positive ions in the plasma.

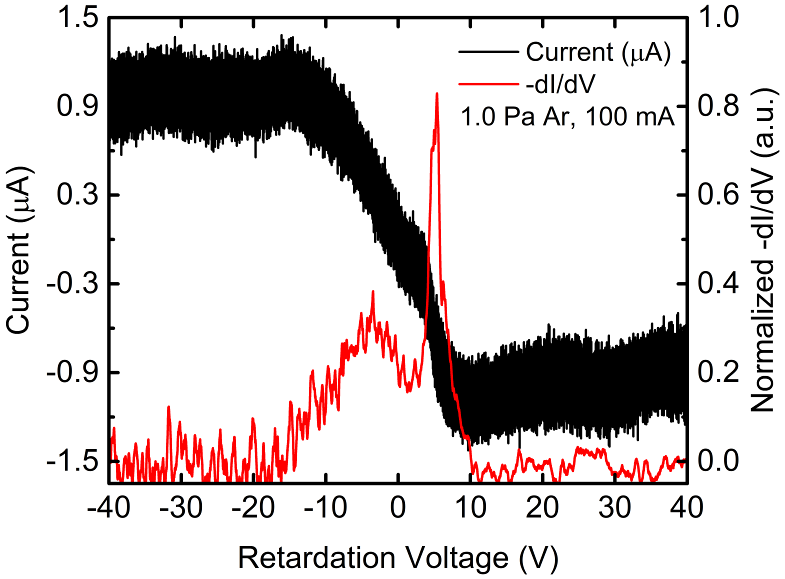

FIGURE 5.7: The typical Faraday cup current and the positive ion energy distribution obtained from the RPA using the biased Faraday cup detection circuit. This measurement was taken at 1.0 Pa, 100 mA discharge current.

5.4.1 Positive Ion Energy Measurements.

Shown in Fig. 5.7 is the typical ion energy distribution obtained using a retardation voltage range of -40 to 40 V in the positive ion measurement configuration of the RPA. At negative retardation plate voltages, a broad electron peak was observed. This peak can be attributed to the high energy electron tail in magnetron sputtering plasmas [22] that had sufficient energies needed to reach the Faraday cup. While this may seem that the methods for minimizing the electron flux to the Faraday cup were insufficient, the exclusion of the low energy electrons significantly decreased the electron contribution to the current signal such that the adequate detection of the ion peaks at positive retardation voltages was realized using the RPA.

The normalized energy distributions obtained using Eq. 5.5 are shown in Fig. 5.8 for the 0 to 50% and 100% water vapor content settings. An ion peak at the 0 to 10 V range was measured. The broad peak initially seen for the 0% setting (1.0 Pa Ar discharge) decreased to a smaller width as the water vapor content increased. The presence of a second peak overlapping peak was observed consistently across the settings.

The effect of the water vapor content on the ion energy distributions was quantified as shown in Fig. 5.9. The peak position (Fig. 5.9a of the most intense peak was found to vary minimally and was centered at $\approx$ 5.4 eV, assuming a singly charged positive ion. The change in the ion current (ΔCurrent) was taken as a measure of the peak intensity. The maximum ΔCurrent was found at the 40% setting, however, further increasing the water vapor content decreased ΔCurrent by a factor of 4 to a saturation level of $\approx$1.28 μA. This observed behavior was consistent with the trend seen with the relative intensity of OES peaks (Fig. 5.6, and is indicative of the setting where the ion generation in the bulk plasma was maximum.

To elucidate where this increased ion density originated from, the shape of the ion energy

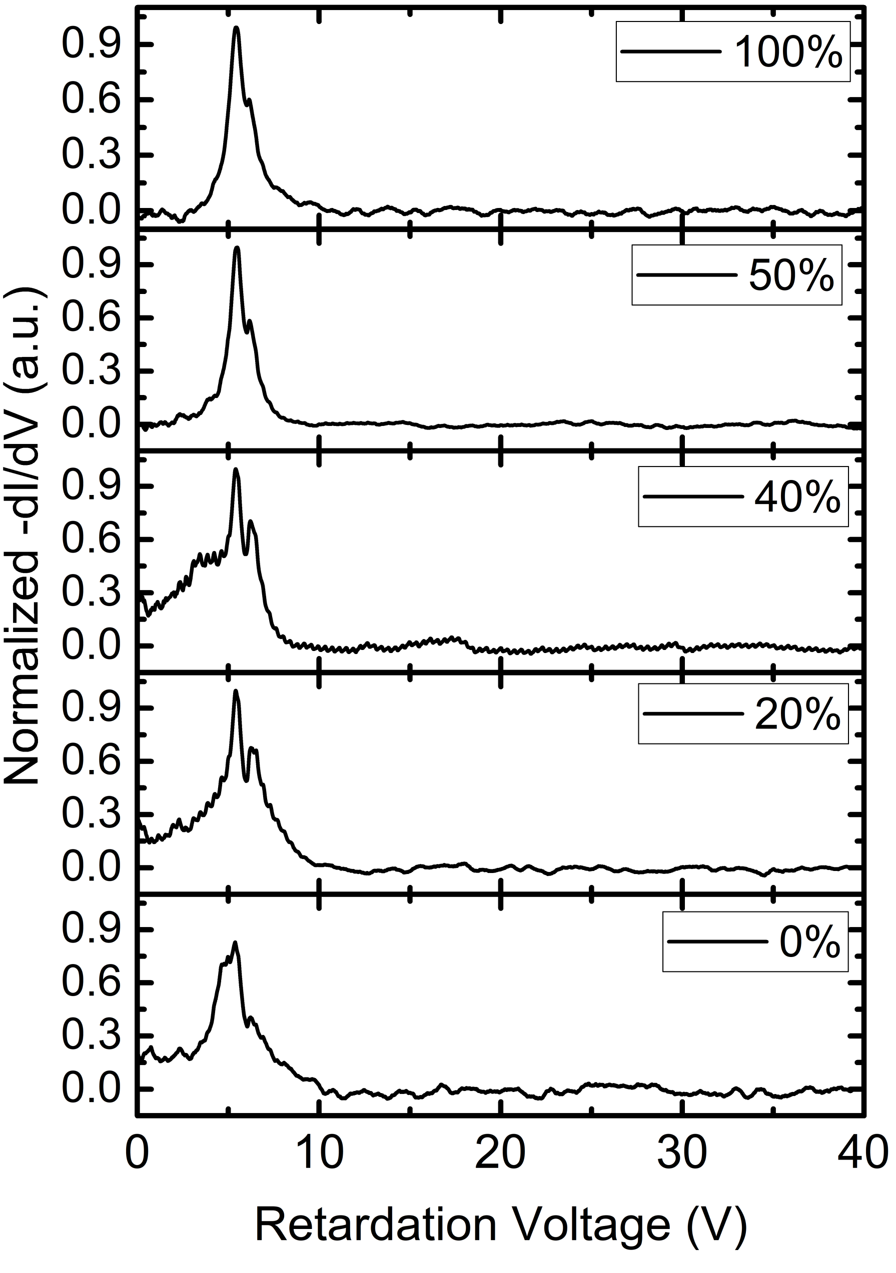

FIGURE 5.8: The positive ion energy distributions measured by the RPA at 0 to 50% and 100% water vapor content.

distribution was analyzed. The energy distribution of the metal ions in a magnetron sputtering plasma can be described using Thompson's random cascade model, as shown in Eq. 5.6:

$$f(E) \propto \frac{E}{(E+E_{sb})^{3-2m_k}} \tag{5.6}$$

where E_{sb} is the surface binding energy of the target surface, and m_k is the exponent of the interaction potential. The typically used value of m_k is 0.2, and the peak energy distribution

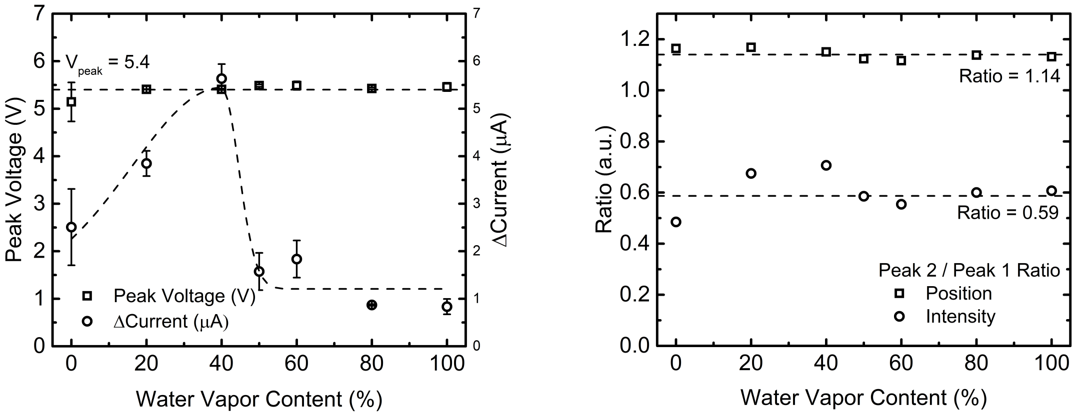

(A) Peak Position and ΔCurrent

(B) Peak Characteristic Ratios

FIGURE 5.9: The (a) peak position and the change in current, ΔCurrent, and (b) the peak characteristic ratios ($Peak_2/Peak_1$) at varying water vapor content. The lines are added to guide the eyes.

was expected to be a single peak at $\frac{1}{2}E_{sb}$[23–25]. Across the water vapor content settings, the average peak energy was at $\approx$ 5.4 eV, and the formation of the oxide at the target surface was indicated by a 0.26 eV increase in peak voltage when water vapor was added to the magnetron sputtering plasma. This shift in energy was attributed to the positive oxide ion sputtered from the target surface[26]. The presence of an overlapping, lower intensity peak in the distribution was attributed to the ionization by the sputtered species as it is transported towards the substrate region and measured using RPA. It was shown that a significant contribution to this peak was from the discharge support or reactive gas [3, 26–28]. Thus, to quantify the peak characteristic changes, the ratio of the peak positions and their intensity were taken, as shown in Fig. 5.9b. The peak position ratio across was $\approx$1.14 irrespective of the water vapor content. This trend was not the case for the intensity ratio and was similar to that of the ΔCurrent, which confirmed that the production of ions in the bulk plasma compared with the sputtered species density was maximum at the 40% water vapor setting. The cause for the amplification of the ion production compared to Ar sputtering could be attributed to the differences in the energy requirements of their respective ionization cross-section.

5.4.2 Negative Ion Energy Measurements

Shown in Fig. 5.10 are the normalized ion energy distribution for the negative ions as measured using the RPA. Compared to the positive ion energy measurements, the energy distribution of the negative ions was significantly broader with peak energy positions greater than -200 V. While the pure 1.0 Pa Ar plasma was not expected to form negative ions [29], a peak was observed centered at $\approx$-350 V. The source of these negative ions in the Ar plasma is attributed to the previously deposited oxide films at the chamber walls near the target cathode. The dense plasma at the cathode region could sputter out these oxides from the wall and would constitute the negative ion signal detected by the RPA. The density of these negative ions was

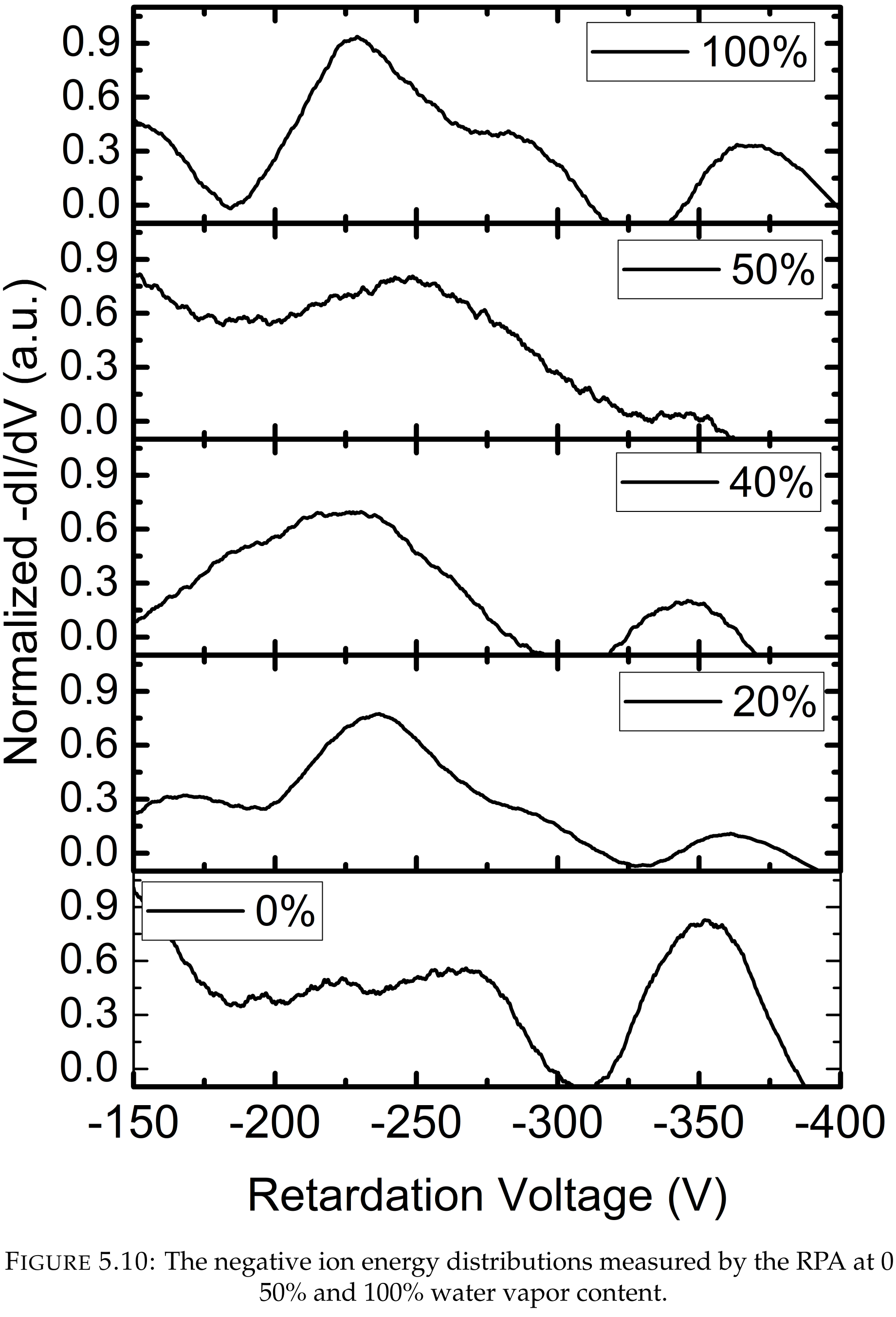

FIGURE 5.10: The negative ion energy distributions measured by the RPA at 0 to 50% and 100% water vapor content.

low, however, as evidenced by the low signal-to-noise ratio and large standard deviation of measurements at the 0% setting.

The peak characteristics of the negative ion measurements were quantified using the peak position, and the ratio with the discharge voltage is shown in Fig. 5.11. For water vapor-containing plasma, the negative ion peak energy was ≈ -274 eV for the 20 to 100% water vapor content settings (5.11a). This value means that using water vapor plasma as the reactive gas in the deposition results in the formation of negative ions, even at low water vapor content.

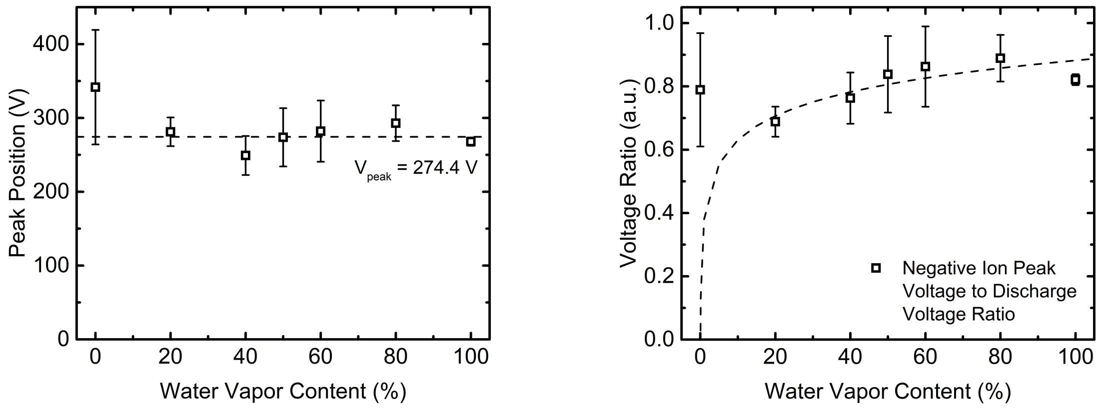

(A) Peak Position

(B) Peak to Cathode Voltage Ratio

FIGURE 5.11: The peak position and the peak-to-cathode voltage ratio of the negative ion energy distributions measured using the RPA. The lines were added to guide the eyes.

The peak energy with respect to the target cathode voltage was measured (Fig. 5.11b) to identify where these negative ions were generated. The peak energy ranged from 69 % to 89% of the cathode voltage, which indicated that the negative ions were generated near the target surface and was accelerated to the measured ion energy by the negative target bias. The negative ion energy indicated that these ions are not from the bulk plasma, as the target bias would act as a potential barrier that prevents the collection and subsequent acceleration of the low energy negative ions at the target surface [3]. However, the exact negative ion species are difficult to determine based on the ion energy distribution alone. As both reactive gas and oxide at the target surface can be accelerated by the target bias, a broad peak distribution was measured. Identifying which species were responsible would require mass-resolved energy measurements.

5.5 Summary of Results

The production of positive and negative ions in water vapor plasma was confirmed using OES and RPA measurements. From the OES results, the production of Ar^+, H^+, Zn^+, and O^+ ions was confirmed from the atomic spectra at the visible region (400-1000), while the production of OH^+ ($A^2\Sigma^+ \rightarrow X^2\Pi$) was confirmed using the band spectra at the UV region (200-500 nm). The relative intensities of the reactive gas peaks exhibited a non-linear dependence on the water vapor content. The trend of the relative intensities indicated that the maximum ion formation rate was realized at 40% water vapor content.

The energy distributions for positive and negative ions produced using water vapor plasma showed significantly different behavior. The positive ion energy distribution across the water vapor settings had an average peak ion energy at ≈5.4 eV, and the addition of water vapor to the plasma shifted the peak by ≈0.26 eV. The overlap of two peaks was observed. The initial, higher intensity peak corresponded to the sputtered species, while the lower intensity peak was attributed to the ionized species from the bulk plasma. The intensity ratio of these two peaks confirmed that the maximum ion formation was at the 40% water vapor content setting. For negative ions, the negative ion energy distribution was significantly broader and was at higher energies (≈274 eV for the 20 to 100% water vapor content). These results indicated that water vapor plasma use resulted in the formation of energetic negative ions and that the ions were generated at the target region. The negatively-biased target surface accelerated the negative ions by ≈69 to 89% of the cathode discharge voltage

References

[1] K. Strijckmans, R. Schelfhout, and D. Depla, "Tutorial: Hysteresis during the reactive magnetron sputtering process," *Journal of Applied Physics*, vol. 124, 24 2018.

[2] J. E. Greene, J. E. Sundgren, L. Hultman, I. Petrov, and D. B. Bergstrom, "Development of preferred orientation in polycrystalline tin layers grown by ultrahigh vacuum reactive magnetron sputtering," *Applied Physics Letters*, vol. 67, 2928, 1995.

[3] K. Ellmer and T. Welzel, "Reactive magnetron sputtering of transparent conductive oxide thin films: Role of energetic particle (ion) bombardment," *Journal of Materials Research*, vol. 27, 765–779, 5 2012.

[4] T. Welzel and K. Ellmer, "Comparison of ion energies and fluxes at the substrate during magnetron sputtering of zno: Al for dc and rf discharges," *Journal of Physics D: Applied Physics*, vol. 46, 31 2013.

[5] Y. Itikawa and N. Mason, "Cross sections for electron collisions with water molecules," *Journal of Physical and Chemical Reference Data*, vol. 34, 1–22, 1 2005.

[6] M. Hayashi, "Bibliography of electron and photon cross sections with atoms and molecules published in the 20th century. argon," 2003.

[7] M. Hayashi, "Electron collision cross-sections for molecules determined from beam and swarm data," in *Swarm studies and inelastic electron-molecule collisions*, L. Pitchford, B. McKoy, A. Chutjian, and S. Trajrnar, Eds., Springer New York, 1987.

[8] M. F. Dony, A. Ricard, J. P. Dauchot, M. Hecq, and M. Wautelet, "Optical diagnostics of d.c. and r.f. argon magnetron discharges," *Surface and Coatings Technology*, vol. 74-75, 479–484, PART 1 1995.

[9] S. A. Moshkalyov, M. Machida, D. O. Campos, and A. Dulkin, "Spatially resolved optical emission study of sputtering in reactive plasmas," *Journal of Vacuum Science and Technology A: Vacuum, Surfaces, and Films*, vol. 16, 514–523, 2 Mar. 1998.

[10] S. How, N. Nayan, J. Lias, M. Ahmad, M. Sahdan, M. Mamat, M. Mahmood, and A. Aldalbahi, "Plasma diagnostic by optical emission spectroscopy on reactive magnetron sputtering plasma -a brief introduction," *Journal of Physics: Conference Series*, vol. 1027, 1 2018.

[11] A. P. Thorne, *Spectrophysics*. Springer Netherlands, 1988.

[12] A. Fierro, G. Laity, and A. Neuber, "Optical emission spectroscopy study in the vuv-vis regimes of a developing low-temperature plasma in nitrogen gas," *Journal of Physics D: Applied Physics*, vol. 45, 49 Dec. 2012.

[13] D. M. Phillips, "Determination of gas temperature from unresolved bands in the spectrum from a nitrogen discharge," 1975.

[14] J. Vorac, L. Kusyn, and P. Synek, "Deducing rotational quantum-state distributions from overlapping molecular spectra," *Review of Scientific Instruments*, vol. 90, 12 2019.

[15] C. Böhm and J. Perrin, "Retarding-field analyzer for measurements of ion energy distributions and secondary electron emission coefficients in low-pressure radio frequency discharges," *Review of Scientific Instruments*, vol. 64, 31–44, 1 1993.

[16] S. D. Johnson, M. M. El-Gomati, and L. Enloe, "High-resolution retarding field analyzer," *Journal of Vacuum Science and Technology B: Microelectronics and Nanometer Structures*, vol. 21, 350, 1 2003.

[17] S. Sharma, D. Gahan, S. Kechkar, S. Daniels, and M. B. Hopkins, "A spatially resolved retarding field energy analyzer design suitable for uniformity analysis across the surface of a semiconductor wafer," *Review of Scientific Instruments*, vol. 85, 4 2014.

[18] P. M. Bryant and J. W. Bradley, "Optimum circuit design for the detection of laser photodetachment signals," *Plasma Sources Science and Technology*, vol. 22, 1 2013.

[19] A. Caldarelli, F. Filleul, R. W. Boswell, C. Charles, N. J. Rattenbury, and J. E. Cater, "Data processing techniques for ion and electron-energy distribution functions," *Physics of Plasmas*, vol. 30, 4 Apr. 2023.

[20] A. Kramida, Yu. Ralchenko, J. Reader, and and NIST ASD Team, NIST Atomic Spectra Database (ver. 5.10), [Online]. Available:https://physics.nist.gov/asd. National Institute of Standards and Technology, Gaithersburg, MD. 2022.

[21] A. Sarani, A. Nikiforov, and C. Leys, "Atmospheric pressure plasma jet in Ar and Ar/H2O mixtures: Optical emission spectroscopy and temperature measurements," *Physics of Plasmas*, vol. 17, 1–8, 6 2010.

[22] T. E. Sheridan, M. J. Goeckner, and J. Goree, "Observation of two-temperature electrons in a sputtering magnetron plasma," *Journal of Vacuum Science and Technology A: Vacuum, Surfaces, and Films*, vol. 9, 688–690, 3 May 1991.

[23] M. W. Thompson, "Ii. the energy spectrum of ejected atoms during the high energy sputtering of gold," *Philosophical Magazine*, vol. 18, 377–414, 152 1968.

[24] W. Hofer, "Angular, energy, and mass distribution of sputtered particles," in *Sputtering by Particle Bombardment III: Characteristics of Sputtered Particles, Technical Applications*, R. Behrisch, Ed., Springer Berlin Heidelberg, 1991, 15–90.

[25] J. T. Gudmundsson, "Physics and technology of magnetron sputtering discharges," *Plasma Sources Science and Technology*, vol. 29, 11 Nov. 2020.

[26] D. Güttler and W. Möller, “The influence of non-uniform target poisoning on the energy distributions of atoms sputtered in a reactive dc magnetron discharge,” *Plasma Sources Science and Technology*, vol. 17, 2 2008.

[27] E Kusano, K Fukushima, T Saitoh, S Saiki, N Kikuchi, H Nanto, and A Kinbara, “Effects of ar pressure on ion flux energy distribution and ion fraction in r.f.-plasma-assisted magnetron sputtering,” 1999, 189–193.

[28] J. M. Andersson, E. Wallin, E. P. Münger, and U. Helmersson, “Energy distributions of positive and negative ions during magnetron sputtering of an al target in ar/o2 mixtures,” *Journal of Applied Physics*, vol. 100, 3 2006.

[29] S. Bratsch and J. Lagowsiu, “Predicted stabilities of monoatomic anions in water and liquid ammonia at 298.15 k,” *Polyhedron*, vol. 5, 1763–1770, 11 1986.

Chapter 6

ION TRANSPORT CONTROL USING A PULSED CONDUIT-TYPE EXTRACTION ELECTRODE

6.1 Introduction

In this chapter, the potential application of water vapor plasma to a plasma source was explored. The magnetron sputtering plasma was generated in a remote source and extracted towards a lower pressure downstream region for measurement. This chapter details how Ar-H_2O plasma was used in the plasma source and explores the extraction characteristics of a pulsed, conduit-type extraction electrode system that realized the extraction process.

6.2 Magnetron Plasma Sources

Plasma sources that remotely generate the plasma and then extract the generated energetic species towards the surface allow for a greater degree of control compared to the conventional deposition process wherein the substrate surface is immersed in the plasma. This process realizes a uniform particle flux to the surface and typically requires an external control system, such as extraction electrodes or mass filtration systems. The deposition rate, however, is inherently lower than the direct deposition process and can significantly add complexity to the process. Nonetheless, as the aspect ratio requirement for devices scales to the nanometer level where substrate damage from uncontrolled energetic species flux is critical, deposition methods with precise control are required. Plasma sources have the potential to realize this.

Magnetron sputtering plasma sources are a known method for producing ions and neutrals of metals and metal oxides. This method has been used in generating nanoparticles or nanoclusters and can realize a continuous, controlled supply of material with a homogeneous size distribution through tailoring the discharge parameters (i.e. discharge current, gas admixture) [1]. An example of a deposition system involving magnetron sputtering plasma sources is gas aggregation sources. This deposition system involves ion cluster growth at relatively high working pressures at the plasma source, and the ion transport to the substrate region through a constricted aperture promotes the aggregation into nanoparticles [2–4].

The generation of ZnO nanoparticles using these types of magnetron sputtering plasma sources have been reported, with intended applications in electro-optical devices, such as quantum dots and storage devices, and gas sensors [5–8]. In this study, the formation of ZnO was explored using a magnetron sputtering plasma source using water vapor plasma. The reactive gas is an important factor in this process. At optimal amounts, the reactive gas acts as a binding agent for nanoparticle growth in gas aggregation sources. The growth was strongly dependent on the adsorption of the reactive gas on the growing nanoparticle [9, 10]. As water

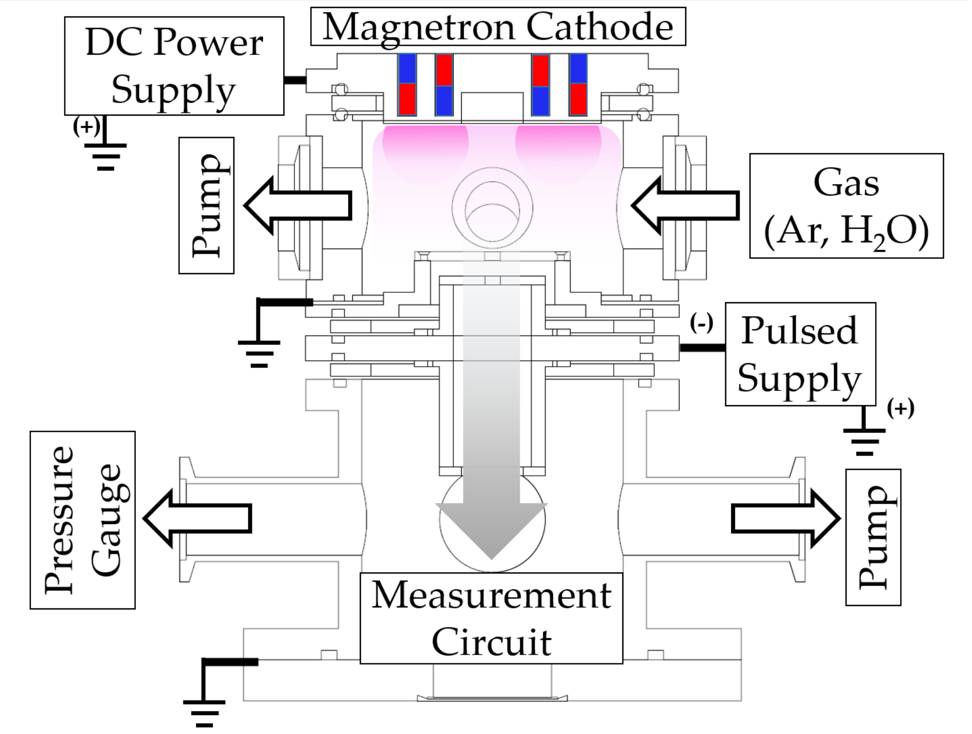

FIGURE 6.1: The reactive magnetron sputtering plasma source system with the pulsed conduit-type extraction electrode. Differential pumping of the plasma source from the downstreamr region was accomplished using the conduit-type electrode aperture.

vapor exhibits a strong adsorption behavior and the added hydrogen in the plasma is beneficial to the improvements in electronic properties of ZnO, investigating the behavior of water vapor in these plasma sources shows potential for the advancement of the technique. However, water vapor is difficult to control in terms of pressure and gas flow in the case of typical gas aggregation sources. The flow to the downstream region was controlled through a differentially pumped aperture, and a pulsed, conduit-type extraction system realized the charged species transport from the grounded plasma source.

6.3 Experimental System

The experimental system (Fig. 6.1) was composed of three regions, the ion source, the pulsed extraction region, and a downstream region. The ion source consisted of an externally-cooled magnetron cathode with two concentric, toroidal NdFeB magnets in an unbalanced magnetron magnetic field configuration and a 70-mm diameter metallic Zn (99.2%) as the target described in Chapter 3. The plasma was sustained using a DC-regulated power supply (Takasago HV1.0-10), with a ballast resistor (1 kΩ, 100W) and choke inductor (11.2 mH). The gases used in the study were argon (Ar, 99.999%) and water (H_2O, distilled water 99.999%). The constant flow of water vapor was achieved through a vaporization-driven water reservoir described in Chapter 2. The pressure was monitored at the two regions using two separate full-range, cold cathode gauges (Tokyo Electronics CC-10, Pfeiffer). The chamber walls of the ion

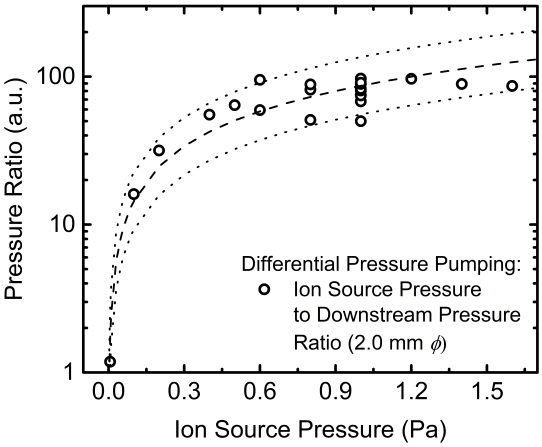

FIGURE 6.2: The pressure ratio of the plasma source region and the downstream region at varying plasma source pressure. The difference was approximately two orders of magnitude lower when using the 2.0 mm diameter aperture. The dashed lines indicate a logarithmic relation between the ratio and ion source pressure (r^2 = 0.932)

source are grounded, and a 2.0 mm diameter aperture in the plasma source was positioned 40.0 mm away from the magnetron cathode target surface. This aperture also serves as the orifice to allow differential pumping of the ion source to the downstream region, as the ion source is operated at a working pressure of 1.0 Pa and 100 mA discharge current, while the downstream region is kept in or below 10^{-2} Pa range for the downstream region measurements. Shown in Fig. 6.2 is the ratio of the ion source pressure to that of the downstream region. For the working pressure ranges considered, a pressure difference two orders of magnitude lower was realized by using the 2.0 mm diameter aperture, particularly for the 1.0 Pa to 1.6 Pa range.

6.3.1 Pulsed Conduit-type Extraction Electrode

The pulsed extraction region, as shown in Fig. 6.3, consisted of the ground plate with the 2.0 mm diameter aperture, PTFE insulators, and a conduit-type electrode. The extraction gap was set at 4.8 mm, and the total length of the extraction electrodes was 72.0 mm. The conduit-type electrode has an entrance aperture of 5.0 mm in diameter and an exit aperture of 20.0 mm in diameter. The voltage pulse was induced by a function generator (EZ Digital DFG6020) coupled with a high-speed amplifier/bipolar supply (NF Electronic Instruments, NF4020) to deliver a square wave pulse from 1 to 500 kHz with a 50% duty cycle. The negative pulse voltage magnitude varied from -20 to -120 V. The positive tailing pulse after the negative voltage phase was applied during the ground phase of the square wave, with a magnitude of 0 to 20 V, as shown in Fig. 6.4.

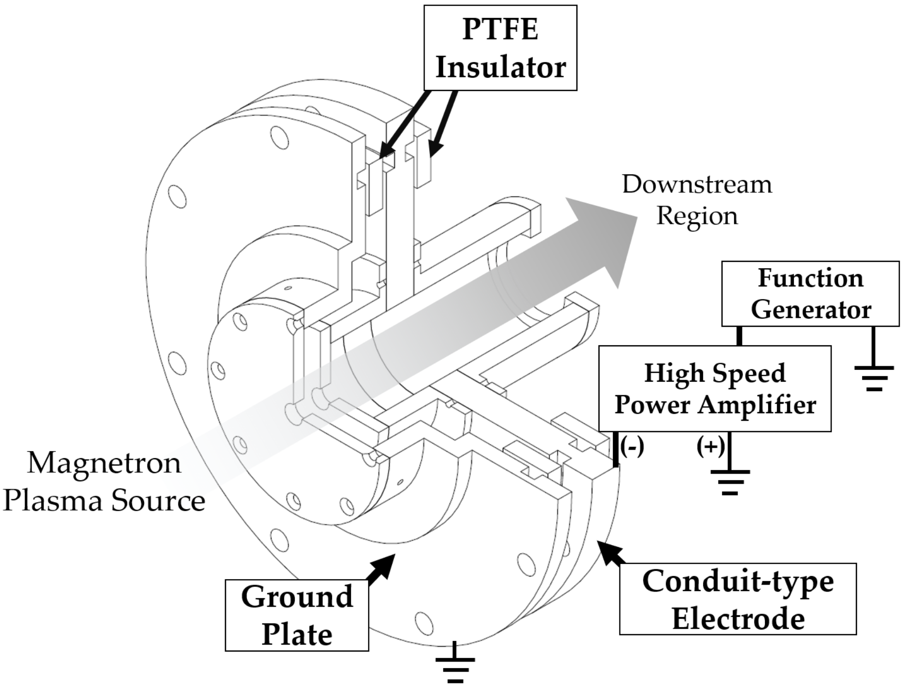

FIGURE 6.3: The pulsed, conduit-type extraction electrode used in this study. The ground plate aperture was set at 2.0 mm diameter, and the extraction gap and length was 4.8 mm and 72 mm, respectively. PTFE insulators isolate the conduit from the grounded plasma source and downstream region.

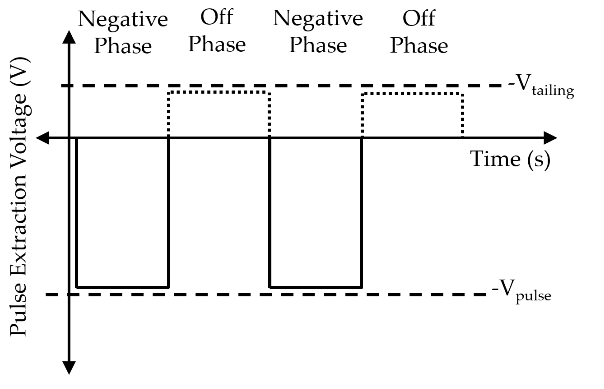

FIGURE 6.4: The positive tailing pulse after the negative voltage phase of the pulsed extraction voltage

6.4 Plasma Source Characterization Techniques

The transport of energetic species from the plasma source was measured at the differentially pumped downstream region. This measurement clarified the extraction and transport mechanism for the pulsed conduit-type extraction electrode system and how the species generated in the plasma source at varying Ar-H_2O ratios and discharge parameters affect the extraction characteristics.

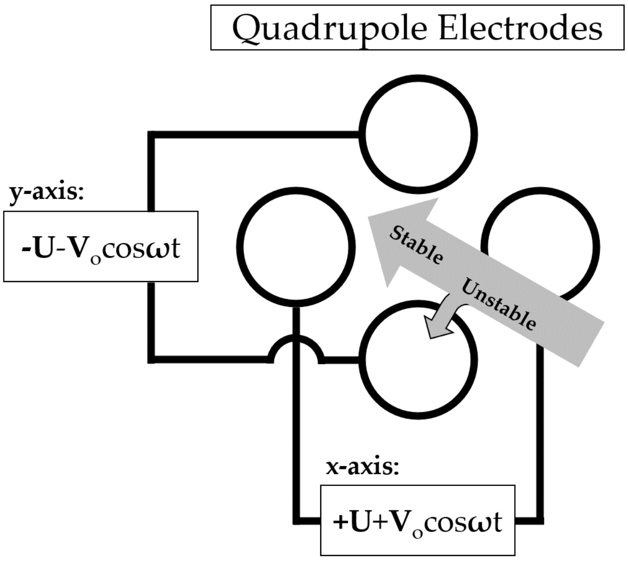

FIGURE 6.5: The schematic of a typical quadrupole mass spectrometer. Ions of with a specific mass-to-charge ratio are able to reach the detector at the z-axis direction, while lighter or heavier ions result to unstable trajectories and are collected at the electrodes.

6.4.1 Quadrupole Mass Spectrometry

Quadrupole mass spectrometry (QMS) was used to detect and identify the positive ion species transported from the plasma source to the downstream region and is a known technique for measuring the mass spectra of ions in deposition process plasmas [11, 12]. In this study, a commercially available residual gas analyzer (Stanford Research Systems, RGA 100) was used. QMS measures the steady state mass spectra from the plasma by trapping the ions in a set of electrodes as shown in Fig. 6.5. As ions enter the region of the electrodes, the electric field produced by DC and RF potentials applied at the electrode traps the ions. Only ions with a mass-to-charge ratio specific to the applied potential ratio at the electrodes can reach the detector. Other positive ions with a larger mass will have unstable trajectories and are lost by hitting the electrode. By sweeping the potentials, the mass-to-charge spectra are obtained from the detector signal [13, 14]. The QMS position was 36.0 mm away from the tip of the extraction electrode exit aperture.

6.4.2 Ion Current Measurements by Faraday Cup

Ion beam currents are typically quantified using a conductive surface as the detector, termed the Faraday cup. As energetic species from the plasma impinge on the surface, if the Faraday cup is hit by these charged particles and connected to an input signal terminal of a signal voltage measurement, a current directly proportional to the amount of impinging species can be measured.

Shown in Fig. 6.6 are the two Faraday cup configurations used in this chapter. Figure 6.6a shows a front-shielded Faraday cup with a 5.0 mm ϕ, with the grounded front plates positioned 28 mm away from the exit aperture of the conduit-type electrode. The current was measured

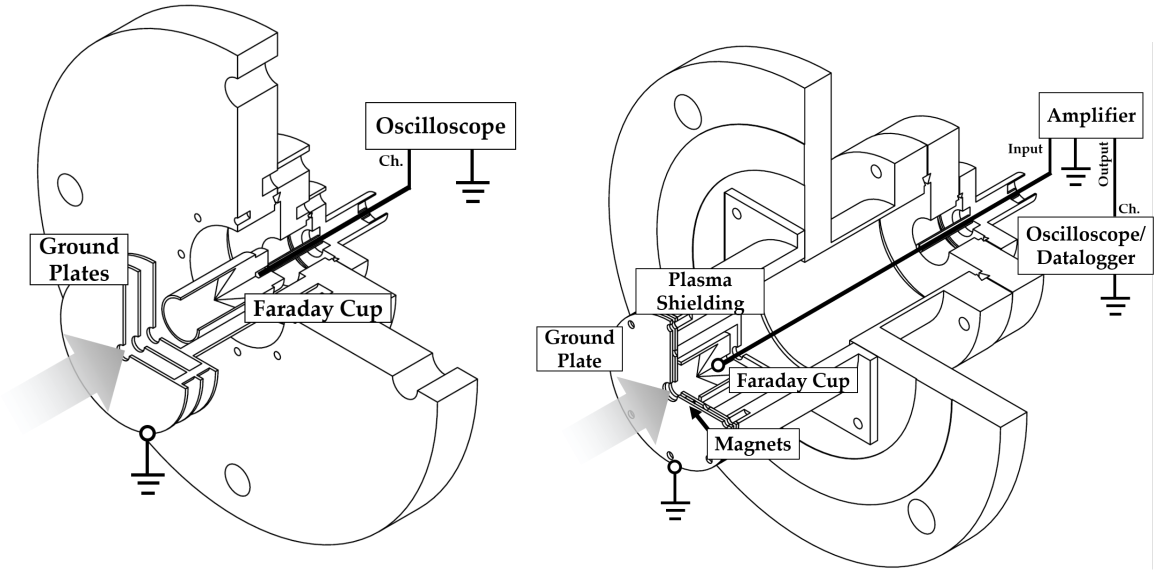

(A) Front shielded Faraday cup

(B) Fully shielded Faraday cup with magnet filter

FIGURE 6.6: The different Faraday cup configurations used in this study. (a) shows the front shielded configuration, while (b) shows a fully shielded configuration with a magnet filter.

by a 1 MΩ AC-coupled oscilloscope (Iwatsu, DS-5424). Figure 6.6b shows the second configuration, a fully shielded Faraday cup with a magnet filter attached at the grounded 5 mm ϕ aperture positioned 6 mm away from the exit aperture of the conduit-type electrode. The magnets realized a ≈ 500 G magnetic flux density to minimize the electron flux towards the Faraday cup. The current was detected using an isolation amplifier (NF Instruments, Model 5325, 10x gain and 1 MΩ input impedance) and oscilloscope. A lock-in amplifier (NF Instruments, Model 5610B) and datalogger (Graphtec Corp., GL900) measured the phase-dependent signal.

6.4.3 Retarding Potential Energy Analyzer

The configuration of the retarding potential analyzer (RPA) for ion energy measurements used in this chapter is detailed in Fig. 6.7. A triple plate configuration was used, with a pair of NdFeB magnets at the entrance aperture to minimize the electron flux configuration. The bias at the retardation plate and current at the Faraday cup was supplied and measured by a 4-wire source measure unit (Keithley, B2901). The bias voltage was swept from 0 to 200 V, with a measurement speed of 10 ms per 100 mV increment. The collimating plate had an entrance aperture of 1.5 mm diameter. The collimating plate, electron repeller plate, and Faraday cup shielding were at ground potential.

6.4.4 Langmuir Probe Measurements

Single Langmuir probe measurements were used to determine the plasma parameters inside the constricted volume of the conduit-type electrode. As described in Chapter 4, the plasma parameters were determined through the probe current as the probe bias, V_{probe}, was

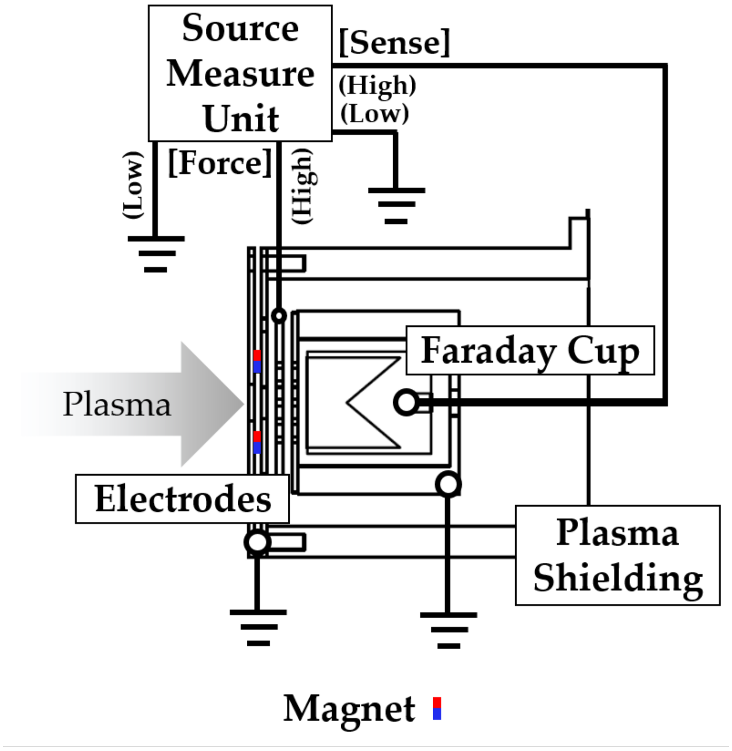

FIGURE 6.7: The retarding potential energy analyzer schematic used for the plasma source ion extraction energy measurements. The retardation bias and current were supplied and measured simultaneously using a 4-wire source measure unit.

swept from a negative to a positive potential. In this chapter, a 1.5 mm diameter, 4 mm long tungsten (W) probe tip was used, mounted on a manipulator flange to varying the location at the central axis of the system. The measurements were taken at 0.0 mm, 15 mm, 30 mm, 45 mm, and 55 mm from the extraction electrode exit aperture. A source measure unit (Keithley, B2901) in the 2-wire configuration supplied the sweep voltage and measured the probe current simultaneously. The sweep range was set at -40 to 40 V at a 0.1 V increment and 50 ms measurement time interval. The parameters investigated in this study are the ion and electron saturation currents, as these are least affected by the time-varying potential inside the extraction conduit.

6.4.5 Finite Element Simulations

Finite element simulations were performed using the FieldPrecision AMaze software to determine the space-charge limited ion trajectories for the pulsed conduit-type electrode. A singly charged (+q), single species is considered, originating from a uniformly and radially distributed 1.0 mm diameter region 1.0 mm away from the center of the ground plate at the plasma source as an approximation of the presheath region near the aperture. Ion-ion collisions were not considered to simplify the simulation. A Boltzmann energy distribution at the initial position was assumed with a set initial average kinetic energy (1 to 10 eV) and initial current of 10 μA. The pulsed extraction behavior was modified via a direct multiplier to the electric field (E-field) solution initially generated from the software by solving Poisson's equation. For

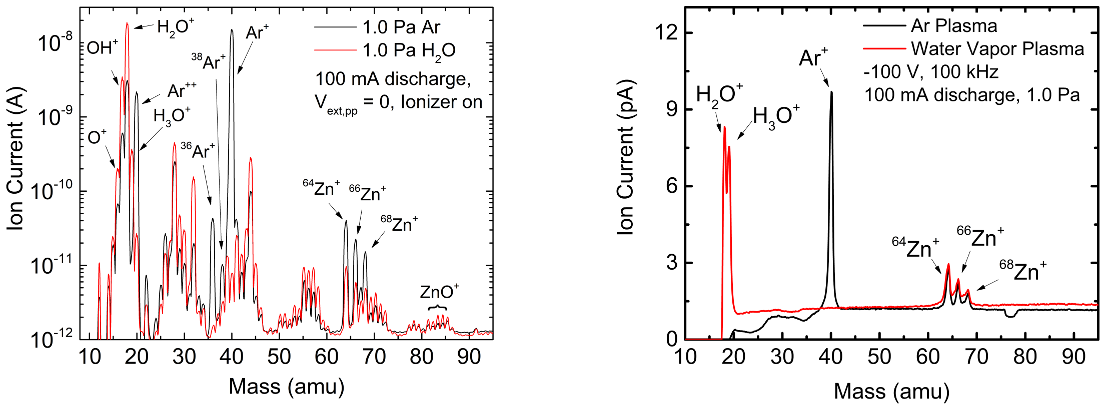

(A) Without pulsed extraction

(B) With pulsed extraction

FIGURE 6.8: The mass spectra for 1.0 Pa Ar and 1.0 Pa H_2O plasma in the reactive magnetron sputtering plasma source (A) without pulsed extraction and (B) with pulsed extraction. The filament ionizer in the RGA was used for the detection of the neutral species transport to the downstream region for the case (A) without pulsed extraction.

the space charge-limited transport, the results were limited to a single half-cycle by the AMaze software. The frequency contribution was simulated by taking the duration of the pulse half-cycle as the total simulation duration.

6.5 Mass Dependent Ion Extraction

6.5.1 Detection by Quadrupole Mass Spectrometry

The ion species formed in the reactive magnetron sputtering source were first confirmed by QMS measurements without pulsed extraction. To detect the neutral species using the QMS, the filament ionizer in the RGA emits eletrons, which ionize the neutral species via electron impact ionization. Shown in Fig. 6.8a are the neutral species transported from the plasma source without pulsed extraction and detected as the ion current through filament post-ionization in the QMS. The transport was caused by molecular flow from the higher pressure plasma source region to the lower pressure downstream region. The key peaks in the mass spectra were confirmed for the injected gas, Ar^+ (40 amu) and H_2O^+ (18 amu), the products from the reactions or fragmentation of the reactive gas, O^+ (16 amu), OH^+ (17 amu), and H_3O^+ (19 amu), and for the sputtered metal, Zn^+ (64,66,68 amu). The reacted oxide compound ZnO^+ (80,82,84 amu) was observed when the water vapor plasma was introduced as the reactive gas.

To detect the ions transported by the pulsed extraction system, the QMS was then operated without the filament ionizer. In Fig. 6.8b, the species extracted from the plasma source using a -100V extraction potential at a 100 kHz pulse frequency from 1.0 Pa Ar plasma were the Ar^+ and Zn^+ ions. For the case of a 1.0 Pa H_2O plasma, the species were H_2O^+, H_3O^+, and Zn^+ ions. The presence of these peaks confirmed that ion extraction occurred, however, the ZnO peak was not detected. The filament ionizer was not used in the measurement, thus, the

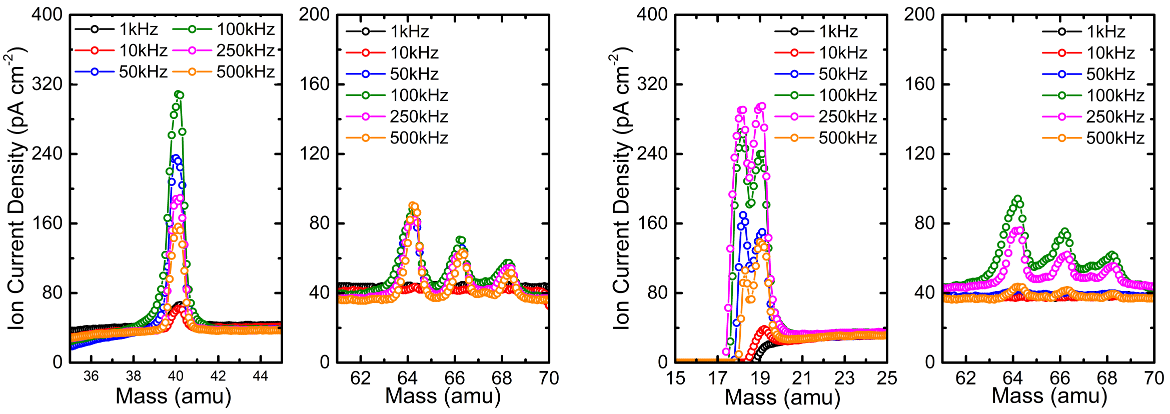

(A) Ar Plasma

(B) Water Vapor Plasma

FIGURE 6.9: The effect of the pulse frequency to the mass spectra peak intensity for Ar^+, H_2O^+, H_3O^+ and Zn^+ ions

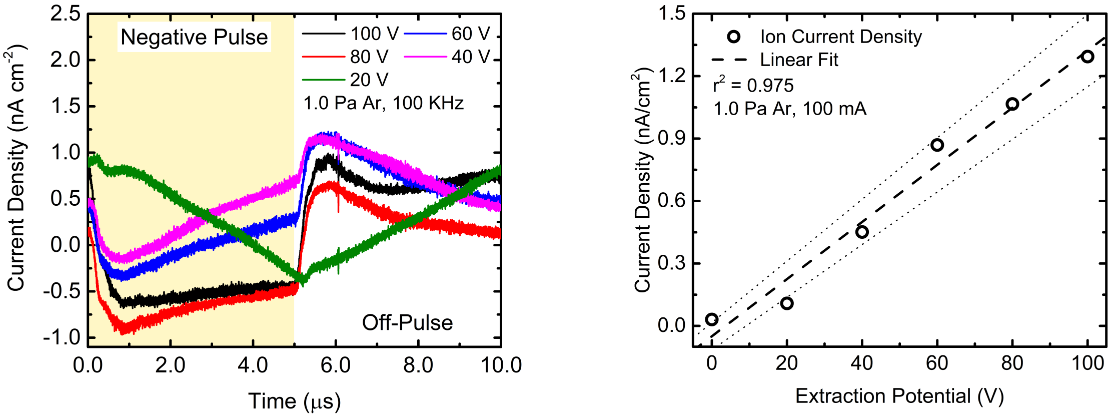

FIGURE 6.10: The effect of varying the pulse extraction potential to the current measured using a front-shielded Faraday cup in Fig. 6.6a and the peak current magnitude as the extraction pulse voltage was increased.

typical fragmentation pattern of gases (i.e. OH^+, O^+) and multiply charged species (i.e. Ar^{++}) were not observed.

6.5.2 Effect of the Pulsed Extraction Potential

The characteristics of the pulsed extraction system were investigated by varying the pulse frequency and the pulsed extraction voltage. As shown in Fig. 6.9, the QMS peak intensity of the detected ion changes as the frequency increases. At low frequencies of 1 kHz and 10 kHz, only ions from the gas, Ar^+, H_2O^+, and H_3O^+, were observed. The Zn^+ metal peak only appears at 50 kHz and higher. The maximum peak intensity for the detected species, in the 1.0 Pa Ar and 1.0 Pa H_2O plasma, was at the 100 and 250 kHz settings.

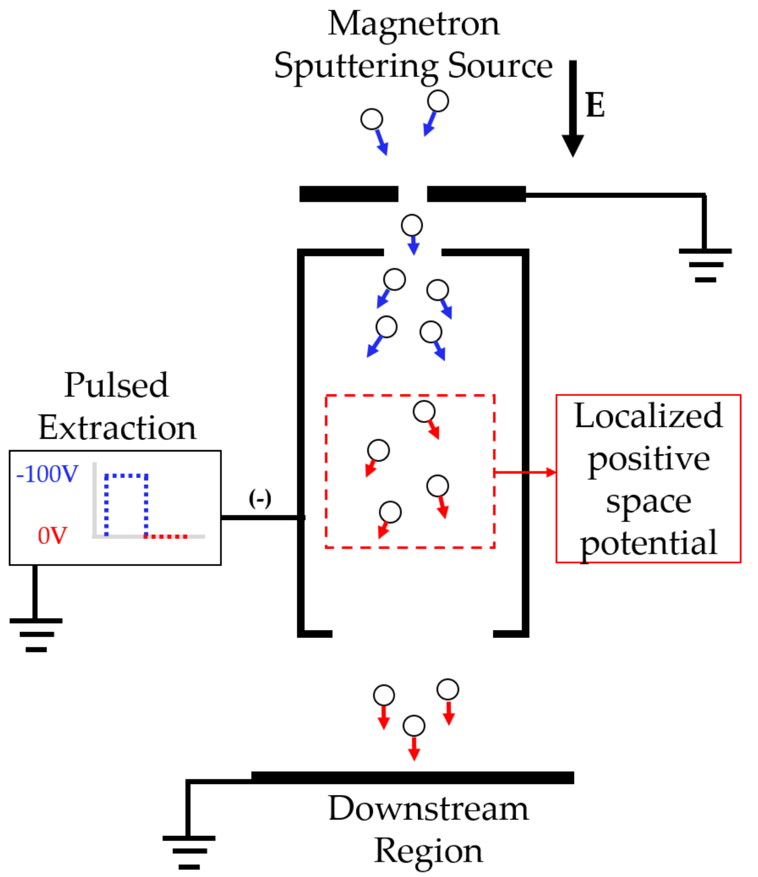

FIGURE 6.11: The proposed mechanism for the pulsed conduit-type extraction electrode configuration.

Figure 6.10 shows the effect of varying the extraction pulse voltage magnitude in a 1.0 Pa Ar plasma at the magnetron sputtering plasma source at a fixed extraction pulse frequency of 100 kHz. The current was measured using the Faraday cup as shown in Fig. 6.6a. The behavior of the measured current shifts as the potential increases. At -20V, the measured current was in phase with the extraction pulse. However, at -40V to -100V, the current has a 180^o phase shift. This shift indicated that at -20V and below, the transport of ions from the source to the conduit-type electrode was inefficient due to an insufficient potential difference between the extraction electrodes. At -40 V to -100 V, the peak was observed at the onset when the potential was reverted to ground, indicating the ion current contribution. This phase was termed the off-phase of the extraction pulse. To quantify the effect of the increasing potential, the peak height, measured from the onset of off-phase, is plotted against the pulse extraction potential (Fig. 6.10b). A linear dependence was observed and indicated that more ions were extracted from the plasma source at higher potentials. Saturation due to the Child-Langmuir law was not observed, as the current was significantly lower in the order of magnitude compared to the theoretical values.

To explain the observed behavior, a mechanism for the pulsed extraction of ions is proposed (Fig. 6.11). During the negative pulse, the positive ions arriving at the ground electrode

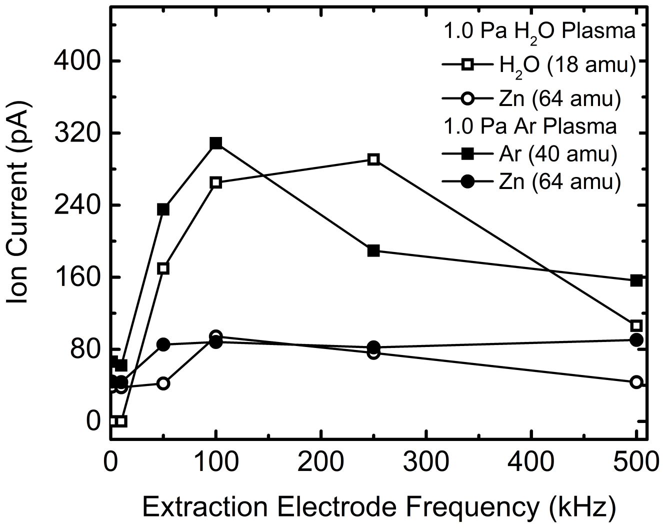

FIGURE 6.12: The ion current at varying extraction pulse frequencies, measured from the mass spectra. The gas ions, Ar^+ and H_2O^+, and sputtered metal, Zn^+, are shown.

aperture at ion acoustic speed are accelerated by the potential drop towards the downstream region. If the pulse duration is sufficiently near the ion transit time (t_{ion}), defined as the time it takes an ion to pass through the conduit length at a certain velocity, then, as the conduit reverts to ground potential in the off-phase, the ions present in the conduit are accelerated to the substrate target by the potential difference between the local positive space potential and the substrate target. This change in potential would realize the maximum possible ion current extracted from the plasma source and can be calculated using Equation 6.1:

$$t_{ion} = \frac{d_{conduit}}{\sqrt{\frac{k_b T_e}{m_{ion}}} + \sqrt{\frac{2qE}{m_{ion}}}} \tag{6.1}$$

where $d_{conduit}$ is the conduit length, and E is the magnitude of the pulsed extraction voltage.

For an electron temperature of 5.0 eV at the ion source, the value of t_{ion} are 2.83 μs for Ar^+, 3.58 μs for Zn^+, and 1.90 μs for H_2O^+. Converting this to the frequency for the extraction electrode pulse, which is a 50% duty cycle square wave, the frequency for Ar^+, Zn^+, and H_2O^+ is at 177 kHz, 140 kHz, and 263 kHz, respectively, as shown:

$$\frac{72\text{mm}}{\sqrt{\frac{k_B(5\text{eV})+2q(100\text{V})}{m_{ion}}}} = 2.83\mu\text{s} \Rightarrow 0.5(\frac{1}{(2.83\mu\text{s})}) = 176.6 \text{ kHz} \tag{6.2}$$

These values are close to the frequencies where maximum ion current was observed from the mass spectra of 1.0 Pa Ar and H_2O plasma as shown in Fig. 6.12. The maxima for the ions occurred at 100 and 250 kHz for Ar^+ and H_2O, respectively.

When the pulse duration is significantly smaller or greater than t_{ion}, the ions could be decelerated or deflected towards the conduit walls. This behavior, and possible ion-ion or ion-electron interactions that could result in a decreased space charge in the conduit, can account for the ion current measured at the different extraction frequencies. The possible space charge neutralization mechanism in the conduit, when the ions are present, is either through a self-neutralization mechanism [15], arising from the pulsed extraction, or by low energy electrons from the ion source [16].

6.6 Extraction Characteristics of a Pulsed Conduit-type Electrode

The extraction characteristics were measured to confirm the proposed extraction mechanism for the pulsed conduit-type electrode. First, the ion trajectories were simulated to identify what happens to ions when the negative pulse bias was applied. Then, the behavior observed was confirmed experimentally, both inside the conduit electrode and at the exit aperture, via single Langmuir probe measurements, ion energy measurements, and Faraday cup measurements that include phase-sensitive signal detection using a lock-in amplifier.

6.6.1 Simulation of Ion Extraction Mechanism

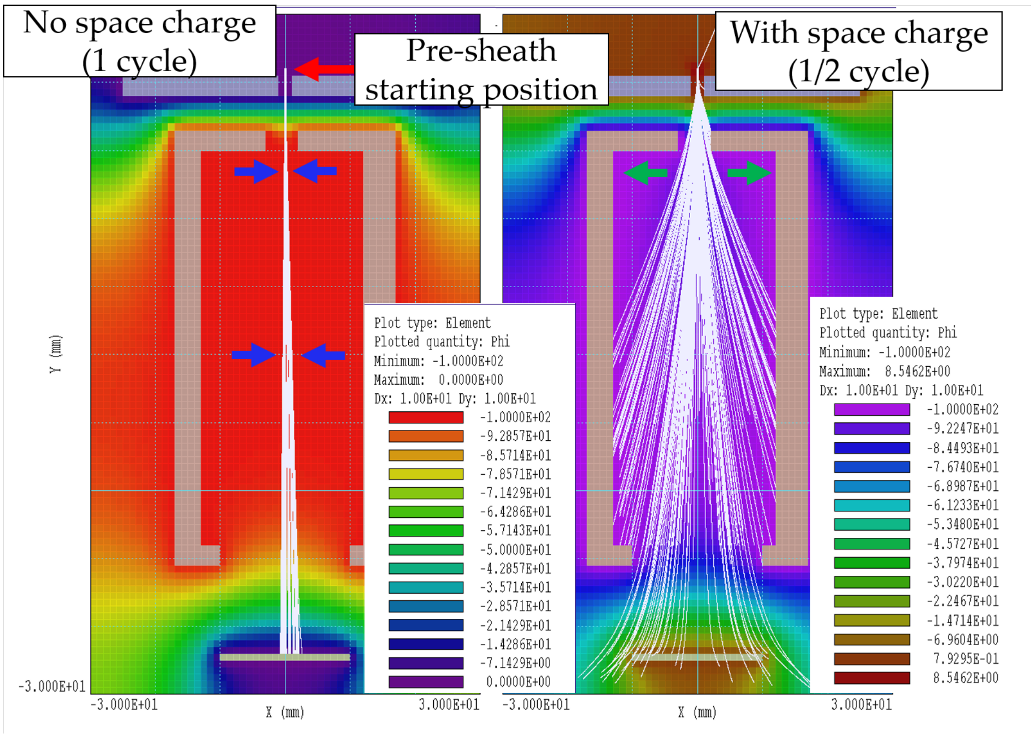

FIGURE 6.13: The effect of the space charge to the ion transport in the pulsed conduit-type extraction electrode as simulated by the finite element method using AMaze software. The divergence of the trajectories are highlighted.

Shown in Fig. 6.13 are the ion trajectory simulation results of the pulsed extraction conduit at a -100 V extraction electrode pulse voltage and 100 kHz using singly charged Ar (40 amu). It was clearly seen that the space charge contribution to the electric field and ion trajectories is significant. Without the space charge, the divergence of the ions was minimal, with minimal collection at the conduit walls and entrance aperture and a high degree of collection at the detector region. However, when the space charge was considered, the ions diverged considerably

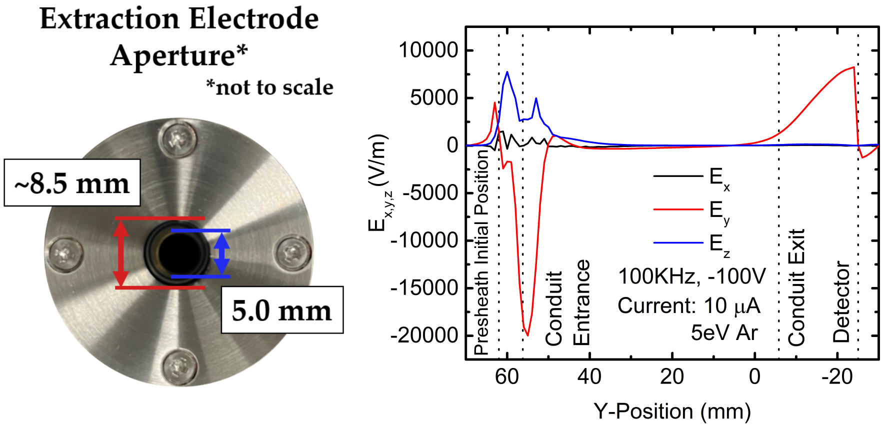

(A)

(B)

FIGURE 6.14: (a) The extraction electrode aperture after use in the pulsed conduit-type extraction electrode. A film deposit approximately 8.5 mm can be seen, indicating a 68.2^o beam divergence as it enters the conduit volume. (b) The electric field components (x, y and z directions) across the central axis of the experimental system as obtained from the space charge-considered ion transport trajectories in Fig. 6.13.

and were collected at the conduit walls and the extraction electrode entrance aperture. Experimentally, the space charge dominant behavior was confirmed at the surface of the entrance aperture, as seen in Fig.6.14a. The "ring" like area indicates that the beam indeed diverged at an angle of 68^o with respect to the ground aperture as it entered the conduit electrode.

The electric field components across the central axis were investigated to quantify this divergence, as shown in Fig. 6.14b. The y component of the electric field indicates the acceleration to the downstream region, and the x and z directions indicate the divergence from the central axis. At the electric field maximum of the plasma source-electrode region, the electric field components for x and y indicated a 42.4^o from $+y$ direction. This behavior is a significant factor, as the divergence of the ion beam at the initial electrode region determines whether the ions are successfully transported to the downstream region or collected at the surface of the electrode [17].

The effect of the transported ions into the conduit volume was measured through the electrostatic potential, ϕ. As the ions fill the conduit volume, ϕ changes depending on the amount present as a consequence of the space charge. The effect of the initial energy and the pulse extraction frequency is shown in Fig. 6.15. Experimentally, the extraction initial energy is varied directly by changing the plasma discharge parameters, such as the discharge voltage or working pressure, which was connected to the thermalization of the ions in a magnetron sputtering discharge [18, 19]. At higher initial energies (Fig. 6.15a), ϕ at the conduit volume deviates positively from the initial DC condition, which indicates that more ions fill the conduit volume. For the frequency (Fig. 6.15b), the 100 kHz setting resulted in the highest shift in ϕ compared to the 250 and 500 kHz settings. This behavior was attributed to the ion plasma frequency. At sufficiently high frequencies, the ions are unable to react readily with the changes in the electric field [20], thus, fewer ions are able to fill the conduit volume.

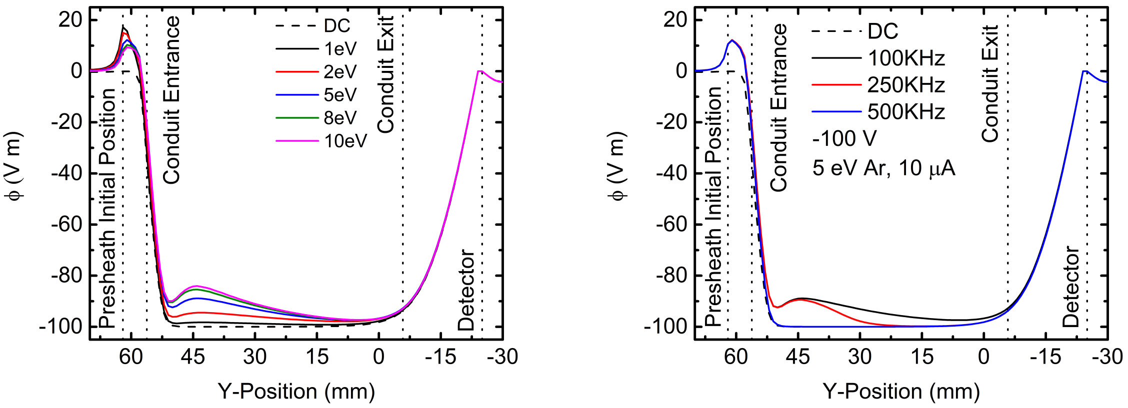

(A) Effect of Initial Energy

(B) Effect of Extraction Electrode Voltage Frequency

FIGURE 6.15: The effect of the initial energy at the plasma source and the extraction electrode voltage frequency to ϕ at varying positions along the central axis of the extraction electrode configuration.

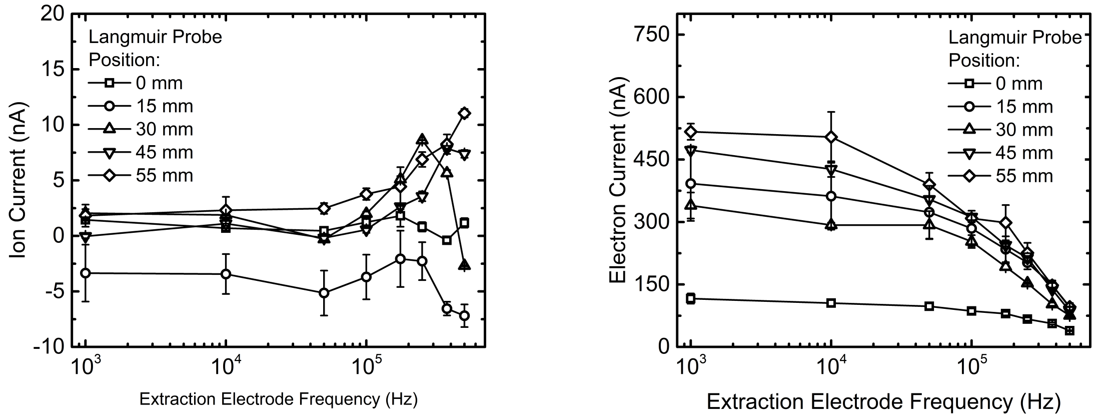

(A) Ion Saturation Current

(B) Electron Saturation Current

FIGURE 6.16: The ion and electron saturation current measured from single Langmuir probes measured in the conduit volume for 1.0 Pa Ar, 100 mA discharge current plasma and a -100 V pulse extraction voltage. The positions are based on the exit aperture location, where 0 mm was at the exit aperture and the 55 mm position was 5 mm away from the entrance aperture.

6.6.2 Ion and Electron Transport using a Single Langmuir Probe

The simulations indicated that the conduit-type electrode was filled with charged species depending on the applied extraction voltage frequency. To characterize how this occurs at different positions across the conduit volume, a single Langmuir probe was inserted to quantify the local species density through the ion ($I_{ion,sat}$) and electron ($I_{e,sat}$) saturation currents.

Shown in Fig. 6.16 are the $I_{ion,sat}$ and $I_{e,sat}$ at varying extraction voltage frequencies for 1.0 Pa Ar at 100 mA discharge current and -100 V pulsed extraction voltage. It can be directly seen that the behavior of the ions and that of electrons are drastically different. $I_{ion,sat}$ exhibited a peak depending on the probe position. This peak current shifts to higher frequencies as the distance from the entrance aperture decreases. The peak current position started from 175 kHz at the 0 and 15 mm positions and consistently increased to 500 kHz at the 55 mm position. The peak position shift confirms Eq. 6.1, as $d_{conduit}$ decreased based on the probe position.

For $I_{e,sat}$, the trend was different from $I_{ion,sat}$. $I_{e,sat}$ increased as the probe was inserted further into the conduit volume, but decreased with increasing extraction electrode voltage frequency. This trend was attributed to the mobility behavior of the electrons. Electrons are more mobile than ions, and the electron plasma frequency is two orders of magnitude greater than the frequency range investigated (1 to 500 kHz) [20]. This means that the electrons can easily respond to changes in the electric field. The electrons could be extracted from the plasma source during the off-phase by the positive space potential inside the conduit volume and are trapped by the extraction voltage shifts at the negative phase. The position of the localized trapping of electrons was estimated to be at the 15 mm position, where $I_{ion,sat}$ was negative and $I_{e,sat}$ was higher than at the 30 mm position. I_{probe} can be shifted to positive currents at the ion saturation region by the presence of an electron source [21], which in this case was attributed to the trapped electrons in the conduit volume.

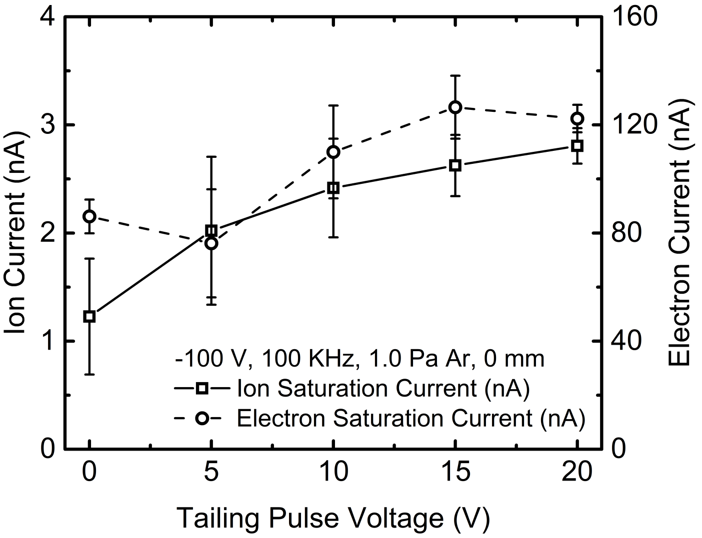

FIGURE 6.17: The effect of a positive tailing pulse to the $I_{ion,sat}$ and $I_{e,sat}$ obtained from single Langmuir probe measurements at the exit aperture position.

As saturation currents were strongly affected by the frequency, the effect of a positive tailing pulse was explored at the 0 mm position as shown in Fig. 6.17. The positive tailing pulse is intended to reduce the divergence produced by the negative phase and accelerate ions from the conduit volume to the detector region during the off phase. The added tailing pulse should allow more ions to pass through to the detector region and would reflect as an increase in the measured current. From the $I_{ion,sat}$, this intended effect occurs as the tailing pulse magnitude increased by a factor of 2.3 by applying a positive tailing pulse of only 20 V. As a consequence, $I_{e,sat}$ also increased by a factor of 1.4, as more electrons from the magnetron sputtering plasma source could have been extracted by the increased positive voltage during the off phase. These results show the possibility of increasing the transported ion density to the downstream region by utilizing a tailing pulse voltage with the conduit-type extraction electrode configuration.

6.6.3 Ion Energy Distributions

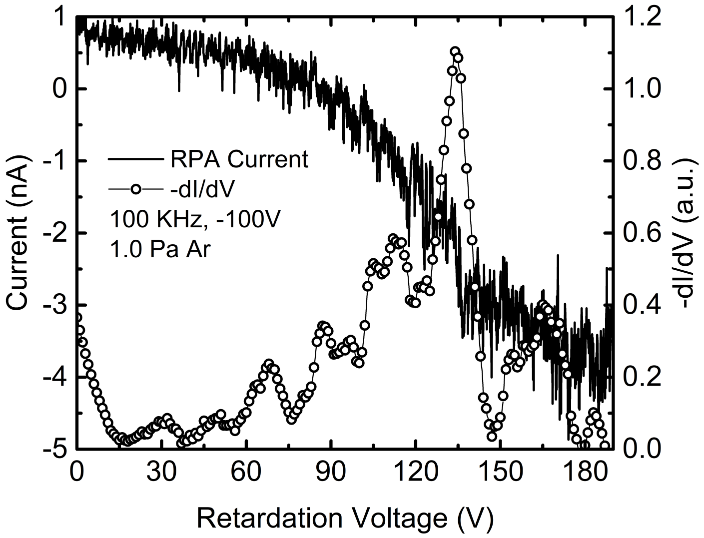

FIGURE 6.18: The typical ion energy distribution obtained from the retarding potential analyzer, for 1.0 Pa Ar plasma at 100 mA discharge current extracted using a 100 kHz, 100 V extraction electrode voltage pulse.

The energy distribution from the plasma source was measured using the RPA to determine the effect of the pulsed extraction voltage frequency on the ion energy. Shown in Fig. 6.18 is a typical current trace obtained during the RPA measurements. A peak with a low-energy tail was observed. Assuming a singly-charged species, the peak corresponds to a 134 eV ion energy extracted from the plasma source.

To investigate the shape of the energy distribution, the Ar^+ and Zn^+ energy spectra from the finite element simulations were used in comparison as shown in Fig. 6.19a. The normalized energy distribution from simulations also showed a low energy tail contributed by heavier Zn^+ ions. For heavier ions, the decreased energy can be attributed to an inhomogeneous local positive space potential at different positions along the conduit volume that influenced the ion's trajectory as it was repeatedly accelerated-decelerated by the applied pulse and the longer ion transit time that could promote the thermalization of the ions. Thus, the extraction of multiple species from the plasma source caused the broad peak shape measured experimentally.

The peak position from the experiment shifted to higher energies by ≈16%. This energy shift could be attributed to acceleration by the accumulated positive space charge in the conduit volume. This phenomenon is supported by Fig. 6.19b, as the peak energy position shifted to lower energies as the extraction electrode voltage frequency increased. At high frequencies, the positive ion density in the conduit decreased and was a result of two possible mechanisms. First, as the ions cannot follow the changes in the electric field, the formation of a DC self-bias could occur [22]. The formation of DC self-bias was reported in conduit tube type geometries

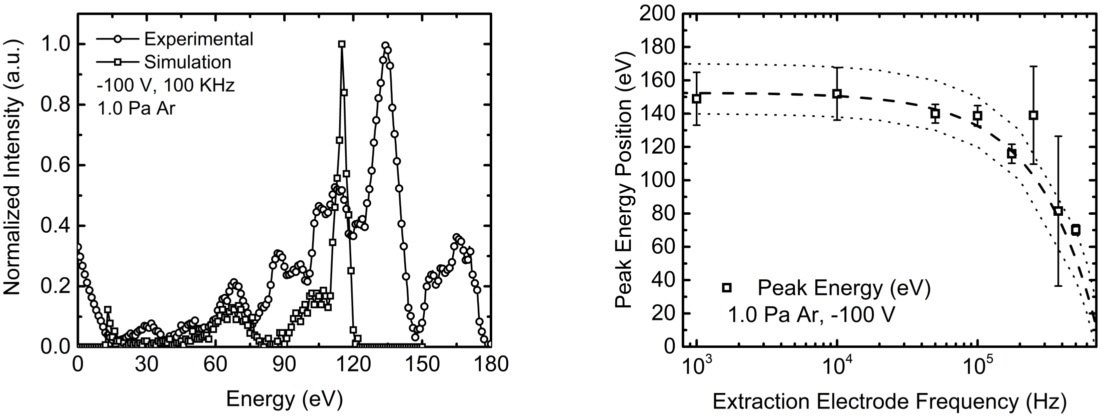

(A) Comparison to Simulation Results

(B) Effect of Extraction Electrode Voltage Frequency

FIGURE 6.19: (A) The comparison of the simulation results to the measured ion energy distribution of the extracted ions at a 100 kHz, -100 V pulsed extraction voltage of 1.0 Pa Ar plasma. (B) The effect of the extraction electrode voltage frequency to the peak position of the ion energy.

[23], and this could be the case for conduit electrodes at higher frequency settings. The DC self-bias magnitude could be lower than that of the peak pulse voltage, resulting in lower energy and density of extracted ions. Second, the electron trapping at the conduit volume can result in the space charge neutralization of the plasma in the conduit volume at high frequencies. The trend of $I_{e,sat}$ obtained from the single Langmuir probe measurements (Fig. 6.16b) matches that of the peak ion energy and indicated that the electron density in the conduit decreased. As electrons have higher mobility, the oscillations by the pulsed voltage could promote ion-electron neutralization interactions and decrease the charge species density in the conduit volume. These two phenomena explain the decreasing ion energy trend observed.

6.6.4 Ion Current Measurements

The pulsed ion transport mechanism proposed for the pulsed conduit-type electrode was a time-dependent phenomenon. Because the plasma extraction approached a steady-state DC self-bias at higher frequencies, the lower half of the frequency range was investigated. To accurately measure this time dependence and the transport time for ions at the downstream region, Faraday cup measurements were performed at the exit aperture location from 1 to 175 kHz. As the ion density at the downstream region was expected to be low, a fully grounded Faraday cup configuration was utilized and a magnet filter was added to minimize the electron contribution to the signal and improve the accuracy of measurements.

6.6.4.1 Average and Peak-to-Peak Current Density Measurements

The measured Faraday cup current contained time-dependent and steady-state components in the signal. Shown in Fig. 6.20 are the steady-state components, represented by the

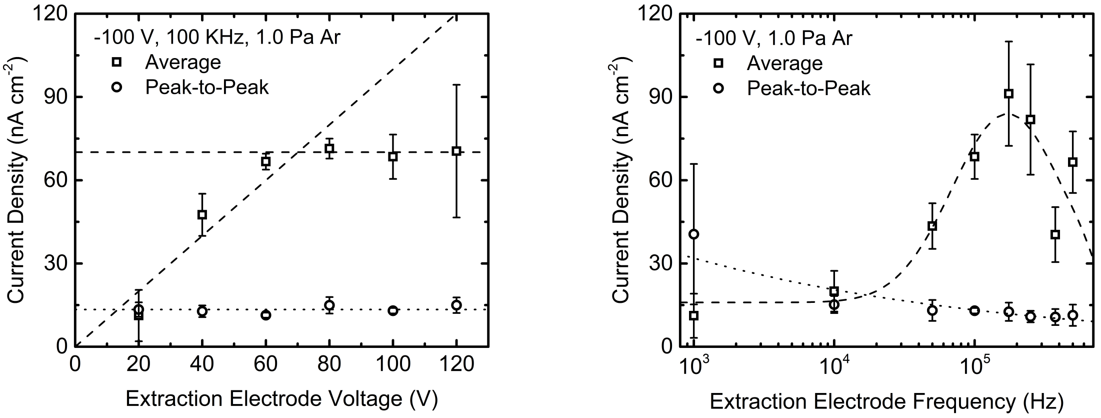

(A) Extraction electrode bias

(B) Extraction electrode voltage frequency

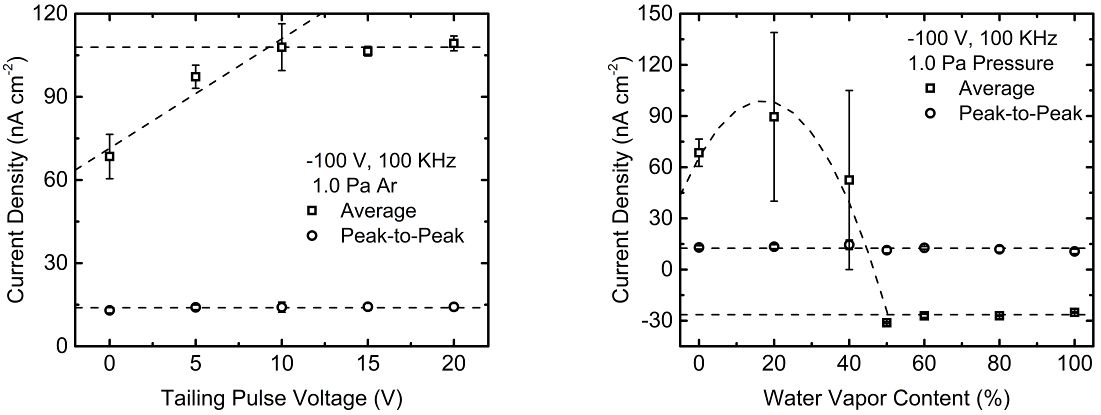

(C) Positive tailing pulse

(D) Water vapor content

FIGURE 6.20: The steady state ion current density measurements at varying discharge and extraction parameters.

average and peak-to-peak current densities measured at varying discharge and extraction electrode parameters.

As shown in Fig. 6.20a, only the average current density increased as the extraction electrode voltage increased. The peak-to-peak current density was relatively constant from 20 to 120 V. From the 80 to 120 V settings, the average current saturation value of 13.6 $\frac{\text{nA}}{\text{cm}^2}$ was measured. This behavior indicates that excessive extraction electrode bias does not necessarily improve the density of the ions that exit the conduit-type electrode.

The effect of the extraction electrode voltage frequency is shown in Fig. 6.20b. The average current density, similar to the QMS and single Langmuir probe measurements, showed a maximum at the 175 kHz setting for the 1.0 Pa Ar plasma. When fitted to a Gaussian distribution, the average current density was centered at 171 kHz (Coefficient of determination, r^2=0.845). This peak fit further reinforced that Eq. 6.1 can be used to estimate where the peak current will occur for a given ion mass. The peak-to-peak current density steadily decreased as the frequency increased. This decrease could be attributed to the mass selectivity of the extraction

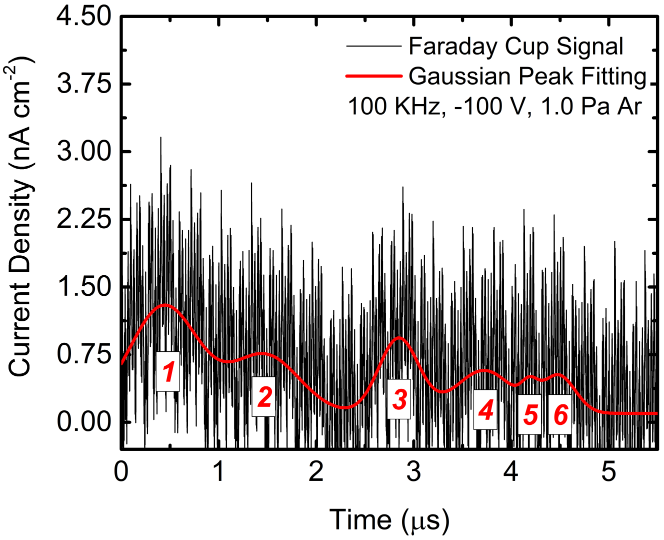

FIGURE 6.21: The typical Faraday cup signal obtained in Sec. 6.6.4 at the off phase. The Gaussian deconvolution of the signal yielded six peaks present in the signal. Peak 3 corresponded to an ion mass of 40.6 amu.

electrodes, where lower frequencies allowed for a wide range of masses to pass through the conduit.

Another method explored was the effect of a positive tailing pulse on the extraction mechanism. As seen in Fig. 6.20c, the peak-to-peak current was unaffected by the positive tailing pulse. However, the average current density significantly increased. For the same increase in extraction electrode bias (100 to 120 V), the current density increased by ≈60% when applying a positive tailing pulse of 20 V as compared to a ≈3% increase for the extraction electrode bias. This trend shows that the positive tailing pulse can effectively improve the current extraction when further increasing the extraction electrode voltage yields minimal results.

When water vapor plasma was used, the average current density drastically changed while the peak-to-peak current was relatively constant. The average current density peaked at the 20% water vapor content setting and decreased to a negative current density value from 50 to 100%. This behavior can be directly attributed to the amplification of the ion density at low water vapor contents as it has lower ionization energy (15.7 eV for Ar and 12.59 eV for H_2O)[24], and a significant negative ion density transported in the conduit.

6.6.4.2 Phase Dependent Measurement

The time-dependent behavior of the ion transport is complex given the multiple ion species present and the low density at the downstream region. Shown in Fig. 6.21 is a typical AC component of the Faraday cup trace during the off phase of the -100 V, 100 kHz pulsed extraction of a 1.0 Pa Ar plasma. A Gaussian deconvolution technique [25] determined the positions of 6 peaks in the trace. Peak 3 was ≈2.85 μs from the onset of the negative phase. If the transport time was converted to the ion mass(Eq. 6.1), this corresponds to a mass of 40.6 amu for the Ar ion. Thus, by analyzing the time-dependent behavior, the species transported to the

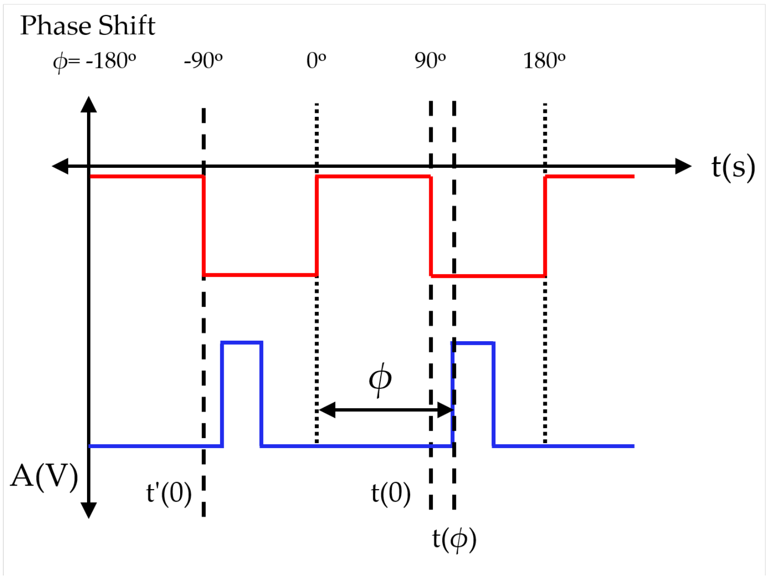

FIGURE 6.22: The analysis method for obtaining t_{ion} using the indirect time-of-flight measurement method that uses the phase-dependent measurements of a lock-in amplifier.

downstream region can be directly identified and controlled using extraction electrode parameters. However, the signal-to-noise ratio was significantly low which made the direct analysis difficult. Thus, a lock-in signal amplifier was utilized. The advantage of a lock-in amplifier in signal detection is its phase-dependent detection. By using a reference during the analysis, amplifying the signal while rejecting the noise components can be realized [26]. This method will improve the signal-to-noise ratio and thus, the accuracy of the measurement.

The indirect time-of-flight measurement using a lock-in amplifier has been utilized for light-based distance detection and was based on the phase shift of the measured signal with respect to reference signal [27, 28]. In this application, the mechanism for phase detection was slightly different. Shown in Fig. 6.22 was the analysis method utilized in this study, with the reference signal being the extraction electrode voltage pulse. As the extraction mechanism started at the off phase, the start position, $t(0)$, was shifted by 90^o. The measured phase shift (ϕ) was then converted to the time of flight using the frequency of the reference signal. In phase-sensitive detection, the overlap of ions with times-of-flight longer than the pulse period used will be rejected by the lock-in amplifier and a clear, amplified signal with the same frequency as the extraction electrode voltage can be directly measured.

The phase was converted into t_{ion} at varying discharge and extraction parameters, as shown in Fig. 6.23. The effect of the extraction electrode voltage is seen in Fig. 6.23a. The shaded areas in the graph indicate the time for Ar^+ and Zn^+ at varying discharge voltage and initial T_e at the plasma source. The 20 and 120 V settings lie outside this region. At 20 V, the low extraction voltage could be insufficient in accelerating the ions due to the low space potential in the conduit volume. At the 120 V setting, the inverse occurred, where an excess of space charge in the conduit volume further accelerated the ions. In the 40 to 100 V settings, t_{ion} passed the Ar^+ and Zn^+ ion regions. This phenomenon meant that tailoring the extraction voltage of the conduit-type electrode allows us a certain degree of control over the mass ratio of the extracted

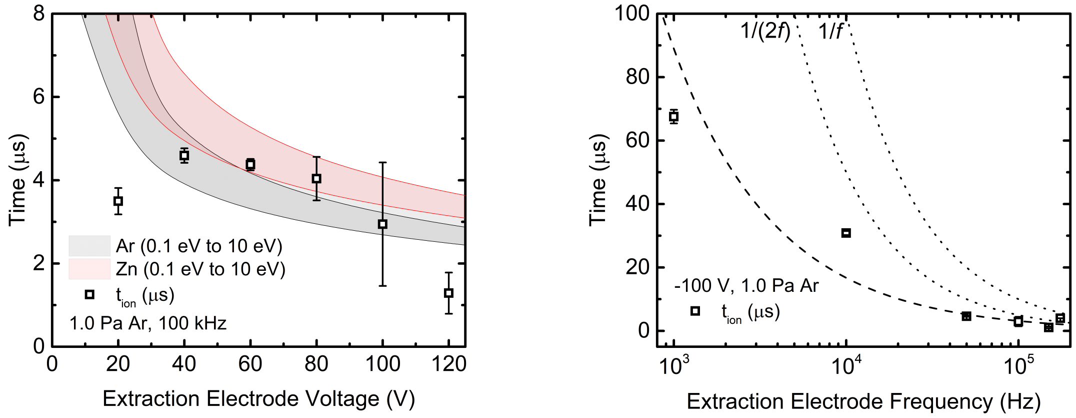

(A) Extraction electrode bias

(B) Extraction electrode voltage frequency

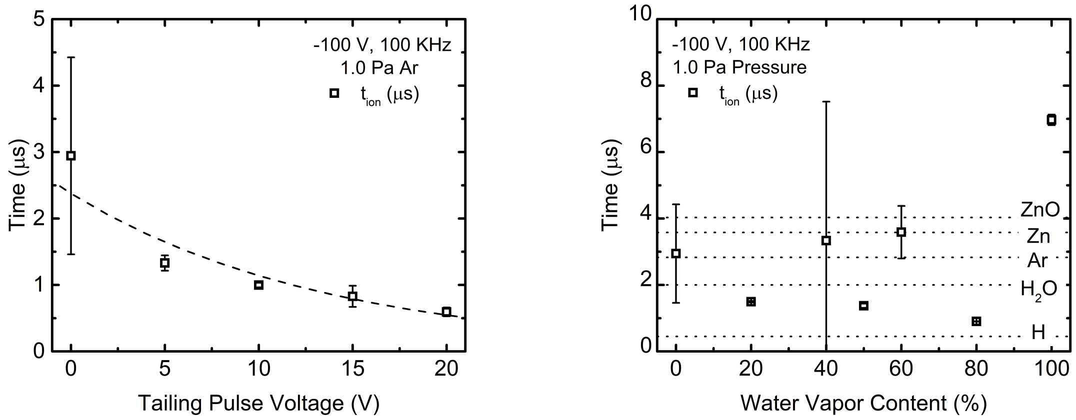

(C) Positive tailing pulse

(D) Water vapor content

FIGURE 6.23: The ion transit time, t_{ion}, as measured from the phase shift, at varying discharge and extraction parameters

ions, where lower voltages tend towards the heavier ions. The effect of the extraction electrode frequency is seen in Fig. 6.23b. The $\frac{1}{f}$ and $\frac{1}{2f}$ highlighted the position of ion transit time with respect to the frequency used. The ion transit time decreased exponentially as the extraction electrode frequency increased, approaching the region in between $\frac{1}{f}$ and $\frac{1}{2f}$ at the 175 kHz setting. From this behavior, it is expected that at higher frequencies, t_{ion} will be significantly longer than the period of the extraction electrode pulse. Lower extraction electrode frequencies would realize more efficient heavier ion extraction.

The effect of the positive tailing pulse voltage is seen in Fig. 6.23c. t_{ion} significantly decreases as the tailing pulse voltage increases. This trend further supports earlier observed trends in the average current density (Fig. 6.20c and single Langmuir probe (Fig. 6.17), and the mechanism where the positive space potential in the filled conduit volume accelerates the ions towards the exit aperture during the off phase.

The effect of the water vapor content in the plasma source was significantly different. There are no visible trends as the water vapor content increased, and it varied widely within the range of possible ion masses in the plasma. A possible cause for anomalous behavior is ion-electron or ion-ion reactions inside the conduit volume. These reactions could significantly change the ion trajectories during the extraction, resulting in the erratic trend for t_{ion}.

6.7 Summary of Results

A reactive magnetron sputtering plasma source that uses a differentially pumped ion source and downstream region with a pulsed, conduit-type extraction electrode has been designed and tested. Using Ar and H_2O plasma in the ion source, the charged species transported to the downstream region with and without pulsed extraction were identified. The pulsed conduit-type extraction electrode extracted Ar^+, H_2O^+, H_3O^+, and Zn^+ ions, and the intensities of the extracted ions as detected by QMS were frequency dependent. A mechanism for the pulsed extraction of ions was proposed where the ion transport strongly depends on the space potential inside the conduit-type electrode.

Multiple plasma characterization techniques confirmed the proposed extraction mechanism. The simulation of the ion transport using the finite element method showed that the amount of ions in the conduit volume is highly dependent on the initial energy conditions at the plasma source and the extraction electrode voltage frequency. At the initial electrode gap, a beam divergence of 68.2^o was observed. Across the conduit volume, the variation of the ions and electrons was measured using a single Langmuir probe. $I_{ion,sat}$ exhibit a peak current at a certain frequency depending on the position inside the conduit volume. $I_{e,sat}$ steadily decreased as the frequency increased, with a local region at 15 mm from the exit aperture where possible electron trapping occurred. In terms of energy, the positive space charge in the conduit volume accelerated the ions further to a higher energy than that set by the extraction electrode voltage. The trapping of electrons at high frequencies (<250 kHz) steadily decreased the ion energy, possibly through ion-electron neutralization pathways. The steady-state current was measured using a shielded and magnet-filtered Faraday cup. The average ion current density extracted from the source saturated starting from 80 V and exhibited a peak ion current density with a Gaussian profile centered at 171 kHz. The indirect time-of-flight measurements showed that the extraction electrode voltage could control the mass ratio of extracted ions, with lower voltages favoring heavier ions. At high frequencies, heavy ion mass extraction could be possible. The mass selectivity and detection are difficult for higher frequencies when t_{ion} exceeds the period of the extraction electrode pulse. The addition of water vapor significantly complicates the behavior of the ion extraction. The presence of the negative ions was detected by the Faraday cup and possible reactions in the conduit volume significantly affected the ion trajectories regardless of mass. A control mechanism to improve the density of extracted ions was proposed. By using a positive tailing pulse in the off phase, the density can be appreciably increased when compared to a similar increase in the extraction electrode voltage.

References

[1] R. Gunnarsson, U. Helmersson, and I. Pilch, "Synthesis of titanium-oxide nanoparticles with size and stoichiometry control," *Journal of Nanoparticle Research*, vol. 17, 9 Sep. 2015.

[2] H Haberland, M Karrais, and M Mall, "A new type of cluster and cluster ion source," *Z. Phys. D: Atoms, Molecules and Clusters*, vol. 20, 413–415, 1991.

[3] O. Polonskyi *et al.*, "Plasma based formation and deposition of metal and metal oxide nanoparticles using a gas aggregation source," *European Physical Journal D*, vol. 72, 5 May 2018.

[4] A. Shelemin, O. Kylian, J. Hanus, A. Choukourov, I. Melnichuk, A. Serov, D. Slavínská, and H. Biederman, "Preparation of metal oxide nanoparticles by gas aggregation cluster source," *Vacuum*, vol. 120, 162–169, 2015.

[5] Z. W. Zhao, B. K. Tay, J. S. Chen, J. F. Hu, X. W. Sun, and S. T. Tan, "Optical properties of nanocluster-assembled zno thin films by nanocluster-beam deposition," *Applied Physics Letters*, vol. 87, 25 2005.

[6] J. Antony, X. Chen, J. Morrison, L. Bergman, Y. Qiang, D. McCready, and M. Engelhard, "Zno nanoclusters: Synthesis and photoluminescence," *Applied Physics Letters*, vol. 87, 2005.

[7] Y. F. Tian, J. Antony, R. Souza, S. S. Yan, L. M. Mei, and Y. Qiang, "Giant positive magnetoresistance in co-doped zno nanocluster films," *Applied Physics Letters*, vol. 92, 19 2008.

[8] V. Postica *et al.*, "Tuning zno sensors reactivity toward volatile organic compounds via ag doping and nanoparticle functionalization," *ACS Applied Materials and Interfaces*, vol. 11, 31452–31466, 2019.

[9] A. Marek, J. Valter, S. Kadlec, and J. Vyskocil, "Gass aggregation nanocluster source - reactive sputter deposition of copper and titanium nanoclusters," *Surface and Coatings Technology*, vol. 205, S573–S576, 2011.

[10] T. Peter, O. Polonskyi, B. Gojdka, A. Ahadi, T. Strunskus, V. Zaporojtchenko, H. Biederman, and F. Faupel, "Influence of reactive gas admixture on transition metal cluster nucleation in a gas aggregation cluster source," *Journal of Applied Physics*, vol. 112, 11 2012.

[11] C. Paternoster, I. Zhirkov, and M. Delplancke-Ogletree, "Structural and mechanical characterization of nanostructured titanium oxide thin films deposited by filtered cathodic vacuum arc," *Surface and Coatings Technology*, vol. 227, 2013.

[12] D. B. Zolotukhin, A. V. Tyunkov, Y. G. Yushkov, and E. M. Oks, "Modified quadrupole mass analyzer rga-100 for beam plasma research in forevacuum pressure range," *Review of Scientific Instruments*, vol. 86, 12 2015.

[13] R. March, "An introduction to quadrupole ion trap mass spectrometry," *Journal of Mass Spectrometry*, vol. 32, 351–369, 1997.

[14] C. Steel and M. Henchman, "Understanding the quadrupole mass filter through computer simulation," *Journal of Chemical Education*, vol. 75, 1049–1954, 1998.

[15] Y. Chen, R. Sawadichai, S. Tian, V. Donnelly, P. Ruchhoeft, and D. Economou, "Nearly monoenergetic positive ion beam with self-neutralized space charge extracted from a pulsed plasma," *Journal of Physics D: Applied Physics*, vol. 52, 35 2019.

[16] M. Vasquez, M. Ilasin, L. Pengson, M. Ramos, and A. Cuevas, "Extraction and transport of low-energy ar ion beams with a broad cross-section," *Vacuum*, vol. 187, 2021.

[17] I. Brown, *The physics and technology of ion sources*. Wiley-VCH, 2004, 379.

[18] S Kadlec, C Quaeyhaegens, G Knuyt, and L. M. Stals, "Energy distribution of ions in an unbalanced magnetron plasma measured with energy-resolved mass spectrometry," 1997, 177–184.

[19] E Kusano, K Fukushima, T Saitoh, S Saiki, N Kikuchi, H Nanto, and A Kinbara, "Effects of ar pressure on ion flux energy distribution and ion fraction in r.f.-plasma-assisted magnetron sputtering," 1999, 189–193.

[20] M. A. Lieberman and A. J. Lichtenberg, *Principles of Plasma Discharges and Materials Processing*, Second Edition. Wiley-Interscience, 2005.

[21] N. Hershkowitz, "How langmuir probes work," in *Plasma Diagnostics*, O. Auciello and D. Flamm, Eds., Elsevier, 1989, 113–183.

[22] Y. Yin, M. Bilek, and D. McKenzie, "The origins of self-bias on dielectric substrates in rf plasma processing," *Surface and Coatings Technology*, vol. 200, 3670–3674, 2006.

[23] J. Upadhyay, J. Peshl, S. Popovic, A. Valente-Feliciano, and L. Vuskovic, "Effect of slefbias on cylindrical capacitive discharges for processing of inner walls of tubular structures - case of srf cavities," *AIP Advances*, vol. 8, 2018.

[24] N. S. J. Braithwaite, "Introduction to gas discharges," *Plasma Sources Science and Technology*, vol. 9, 517–527, 4 2000.

[25] A. Caldarelli, F. Filleul, R. W. Boswell, C. Charles, N. J. Rattenbury, and J. E. Cater, "Data processing techniques for ion and electron-energy distribution functions," *Physics of Plasmas*, vol. 30, 4 Apr. 2023.

[26] J. Aguirre, D. García-Romeo, N. Medrano, B. Calvo, and S. Celma, "Square-signal-based algorithm for analog lock-in amplifiers," *IEEE Transactions on Industrial Electronics*, vol. 61, 5590–5598, 10 2014.

[27] C. Bamji, J. Godbaz, M. Oh, S. Mehta, A. Payne, S. Ortiz, S. Nagaraja, T. Perry, and B. Thompson, "A review of indirect time-of-flight technologies," *IEEE Transactions on Electron Devices*, vol. 69, 2779–2793, 2022.

[28] K. Yasutomi and S. Kawahito, "Lock-in pixel based time-of-flight range imagers: An overview," *IEICE Transactions on Electronics*, vol. E105.C, 301–315, 7 2022.

Chapter 7

CONCLUSIONS AND RECOMMENDATIONS

7.1 Conclusions

In this chapter, the significant results of the dissertation are summarized. The application of water vapor as the reactive gas in a reactive magnetron sputtering deposition system and plasma source was explored through a systematic investigation of the deposition process.

7.2 On the stable introduction of water vapor plasma and simulation using a reactive magnetron sputtering model

The heated vaporization-driven reservoir realized the stable flow of water into a low-pressure deposition system. Temperature control of the reservoir increased the responsiveness of the water vapor reservoir as a gas source. The simulation of Berg's reactive magnetron sputtering model for water vapor plasma was performed at varying model parameters (sticking coefficients, α, sputtering yield, Y_c, and surface site density, $k(n_s)$). By fitting experimentally measured pressure curves of water vapor plasma with the time-resolved model, it was shown that these model parameters were significantly affected by the pressure behavior at varying discharge parameters, such as the working pressure, the discharge current, and the gas admixture with an inert gas, Ar. The gas admixture was determined to be the most suitable as the compound fraction at the substrate, θ_s, was found to increase linearly up to a water vapor content of 60%.

7.3 On the surface processes at the target surface region

The target surface condition at varying water vapor content and the center and racetrack regions of the metallic target at the magnetron sputtering cathode were investigated through its surface composition, surface morphology, and laser differential reflectance as an *in-situ* monitoring technique. The dominant surface processes were dependent on the target region. At the center, the redeposition of material was strong compared to the racetrack region where the erosion of target material by sputtering was dominant. The presence of redeposited layers with a preferred crystallographic orientation was observed at the 0% and 20% settings, while an oxide overlayer was indicated by the (100) and (002) peaks of ZnO at the higher water vapor content settings. The average roughness, R_a, decreased for both regions the center and racetrack region at increasing water vapor content. At the racetrack region, pitting was observed as confirmed through laser microscopy. The trend for the oxide formation as estimated by the XRD, the decrease in R_a, and the laser differential reflectance at the center region were similar with θ_s from Berg's time-resolved mode. These results elucidated what happens at the target surface, and confirmed the viability of using the laser differential reflectance incident at the center region as a viable *in-situ* method for monitoring the target surface during reactive magnetron sputtering.

7.4 On the deposition of ZnO thin films

The ZnO thin films were deposited at varying water vapor content in an Ar - H_2O gas admixture. The change in film properties was correlated to changes in the near substrate surface plasma parameters obtained from a single Langmuir probe. The addition of water significantly changed the behavior of the plasma and changed the growth mechanism of the film. The transition from a metallic Zn film to ZnO was observed at a water vapor content of 40% and this shift coincided with the plasma parameters. Deposition at the 40% water content setting resulted in a transparent (87.5% transmittance) and conductive thin film (ρ = 1.20 Ωcm). The measured E_g represented a 0.4% decrease compared to the theoretical value, confirming the shallow H donor doping phenomenon when water vapor plasma was used. The ZnO deposition at varying substrate bias and substrate temperatures was investigated as a form of deposition control. The polarity of the substrate bias changed the incident charged species, while the bias magnitude affected the energy. The film characteristics were directly linked to the ion and electron flux to the surface. The shallow donor doping (3.32 eV) and optical transparency of the films ($\approx$85%) were unaffected by the substrate bias. When substrate heating is employed, the adsorption behavior of water became an important factor governing the plasma process. Increasing the substrate temperature resulted in a localized increase in ions near the surface, whereas crossing a threshold temperature resulted in the promotion of film growth. At higher substrate deposition temperatures, the growth of ZnO peaks other than (002) was preferred at higher temperatures while consistently decreasing ρ. The desorption of the oxygen species from the film surface at higher substrate temperatures can be the reason for decreasing the film resistivity. The shallow donor doping of ZnO for films deposited using water vapor plasma was stable for the 20^o to 140^oC range.

7.5 On the positive and negative ion production

The production of positive and negative ions in water vapor plasma was confirmed using OES and RPA measurements. The production of Ar^+, H^+, Zn^+, O^+, and OH^+ ions was confirmed from the atomic and molecular band spectra at the visible (400-1000) and UV regions (200-500). The trend of the relative light emission intensities indicated that the maximum rate of ion formation was at 40% water vapor content. The energy distributions for positive and negative ions produced using water vapor plasma showed significantly different behavior. The positive ion energy distribution across the water vapor settings had an average peak ion energy at $\approx$5.4 eV and the addition of water vapor to the plasma shifted the peak by $\approx$0.26 eV. The intensity ratio of two overlapping peaks confirmed that the maximum ion formation was at the 40% water vapor content setting. On the other hand, the negative ion energy distribution was significantly broader and was at higher energies ($\approx$274 eV for the 20 to 100% settings). These results indicated that the use of water vapor plasma resulted in the formation of energetic negative ions. The negatively-biased target surface accelerated the negative ions by ≈69 to 89% of the cathode discharge voltage.

7.6 On the controlled ion transport using a pulsed-conduit type extraction electrode system

A reactive magnetron sputtering plasma source with a pulsed, conduit-type extraction electrode has been designed and tested. Using Ar and H_2O plasma in the ion source, the charged species transport to the differentially pumped downstream region was confirmed using quadrupole mass spectrometry (QMS). The pulsed conduit-type extraction electrode extracted Ar^+, H_2O^+, H_3O^+, and Zn^+ ions, and the intensities of the extracted ions as detected by QMS were frequency dependent. Multiple plasma characterization techniques confirmed the proposed space charge-dependent extraction mechanism. The simulation of the ion transport showed that the number of ions in the conduit volume was highly dependent on the initial energy conditions at the plasma source and the extraction electrode voltage frequency. The maximum ion current at certain frequencies depends on its position inside the conduit volume. The electron saturation current steadily decreased as the frequency increased, indicating the possibility of electron trapping. The positive space charge in the conduit volume accelerated the ions further to higher energies than that set by the extraction electrode voltage (1 kHz to 250 kHz). The trapping of electrons, however, steadily decreased the ion energy as the frequency increased (<250 kHz). The average ion current density measured by a shielded Faraday cup exhibited a peak ion current density with a Gaussian profile centered at 171 kHz. For the time-resolved measurements, the indirect time-of-flight showed that the extraction electrode voltage could control the mass ratio of extracted ions, with lower voltages favoring heavier ions. At high frequencies, heavy ion mass extraction could be possible, but mass selective detection is difficult since the ion transit time, t_{ion}, exceeds the period of the extraction electrode pulse. The addition of water vapor significantly complicates the behavior of the ion extraction. The presence of the negative ions was detected by the Faraday cup and reactions in the conduit volume could significantly affect the ion trajectories regardless of mass. A control mechanism using a positive tailing pulse in the off phase realized an increased ion extraction density compared to a similar increase in the extraction electrode voltage.

7.7 Further Studies and Recommendations

Further experiments with water vapor plasma in a reactive magnetron sputtering deposition process would involve mass-dependent negative ion measurements in the bulk plasma, such as laser photodetachment. This method involves the injection of photons into the reactive plasma containing the negative ions. If the photon energy is sufficient, electrons resulting from the relaxation of the negative ion to the ground state can be measured by a positively biased

Langmuir probe. By measuring the exact negative ion contribution, the mechanism of formation at the target cathode surface that accounts for the reduced negative ion energy by using water vapor plasma will be determined

For the pulsed conduit-type extraction electrode system and reactive magnetron sputtering plasma source, different aperture geometries with the positive tailing pulse could significantly increase the ion density. Combining this with the use of a reactive gas could realize nanoparticles with a unique geometry, such as core-shell structures.

Appendix A

Chapter 2: Supplementary Data

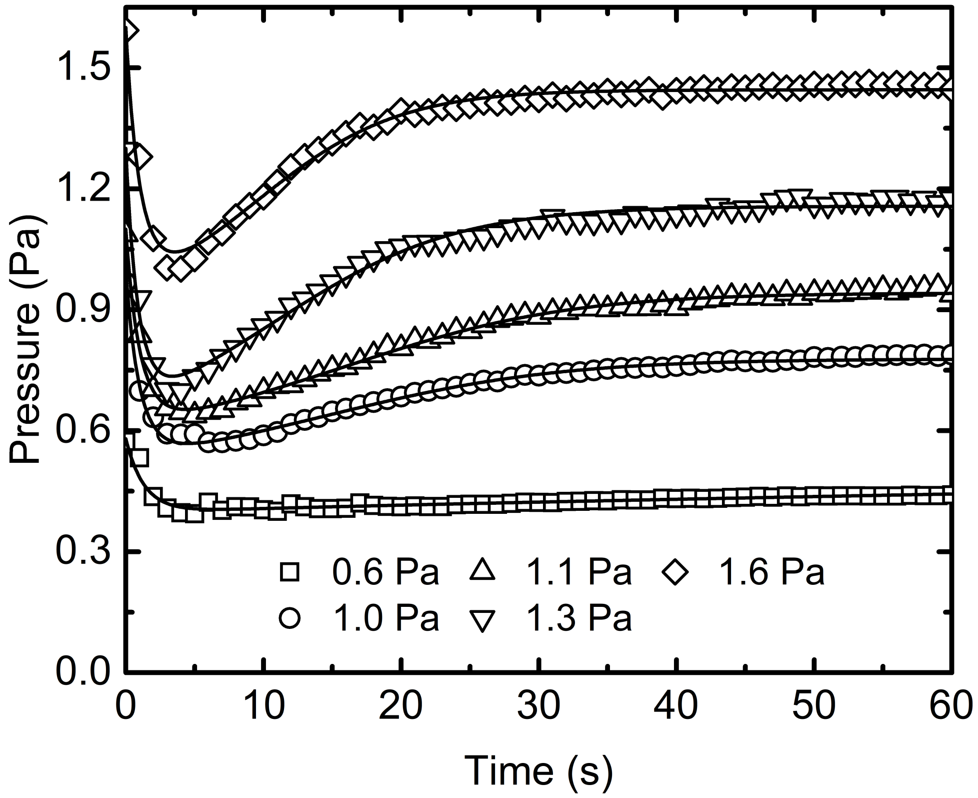

FIGURE A.1: The fit of the pressure at varying water vapor plasma working pressures

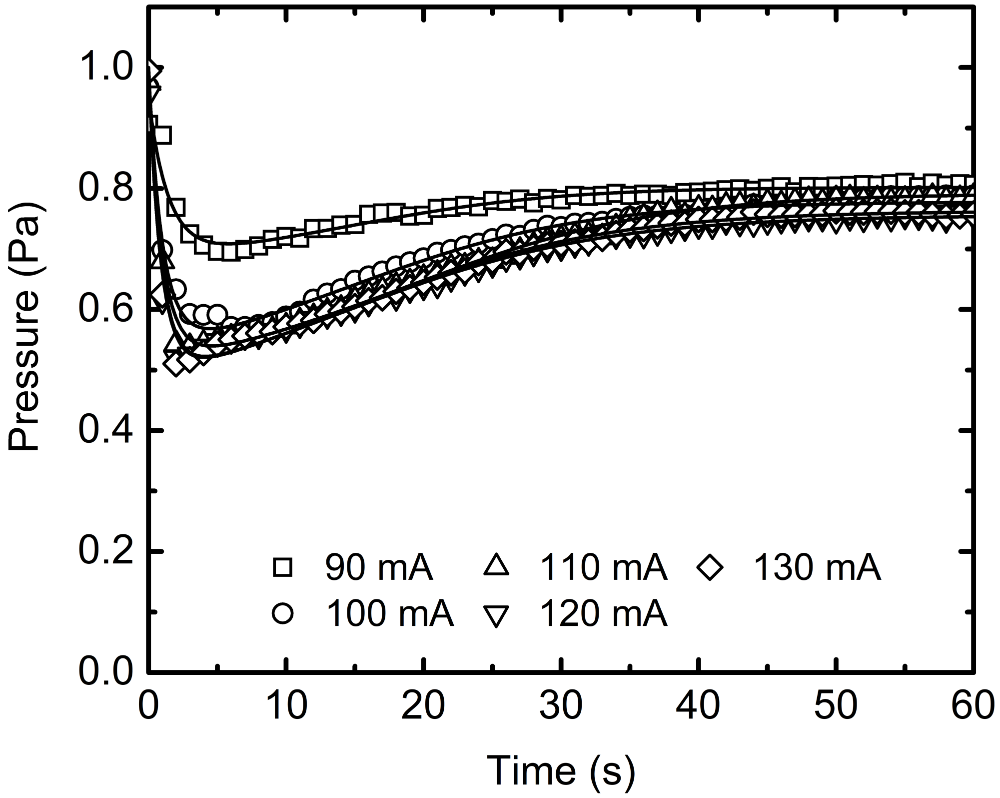

FIGURE A.2: The fit of the pressure at varying water vapor plasma discharge currents

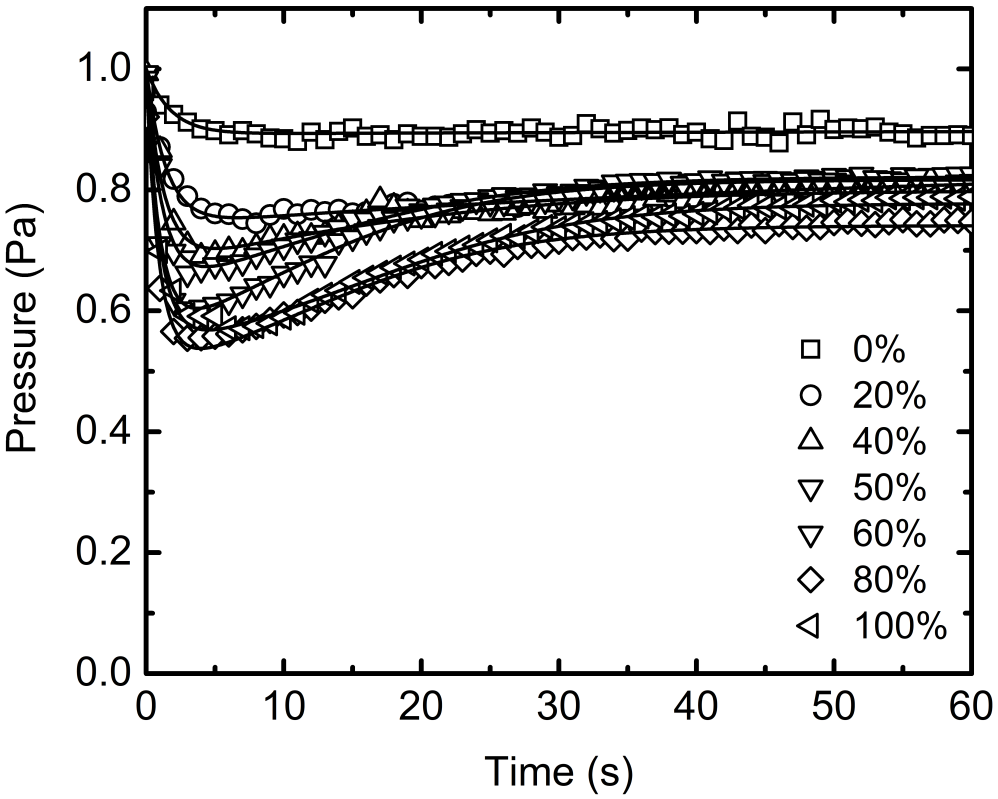

FIGURE A.3: The fit of the pressure at varying water vapor content

TABLE A.1: Parameters for the fitting of the time-dependent pressure at varying water vapor pressure

Pressure (Pa)	Y_c	n_{layer}	α_{sub}	α_t	χ^2
0.6	$9\text{x}10^{-4}$	1270	$4\text{x}10^{-5}$	$6\text{x}10^{-5}$	$6.703\text{x}10^{-5}$
1	0.0025	720	$9\text{x}10^{-5}$	$8\text{x}10^{-5}$	$1.633\text{x}10^{-4}$
1.1	0.002	850	$8\text{x}10^{-5}$	$9\text{x}10^{-5}$	$1.924\text{x}10^{-4}$
1.3	0.0038	1150	$9\text{x}10^{-5}$	$1.8\text{x}10^{-4}$	$5.871\text{x}10^{-4}$
1.6	0.003	830	$7\text{x}10^{-5}$	$1\text{x}10^{-4}$	$4.955\text{x}10^{-4}$

TABLE A.2: Parameters for the fitting of the time-dependent pressure at varying discharge current

Discharge Current (mA)	Y_c	n_{layer}	α_{sub}	α_t	χ^2
90	$7\text{x}10^{-4}$	230	$4\text{x}10^{-5}$	$2\text{x}10^{-5}$	$1.130\text{x}10^{-4}$
100	0.0025	720	$9\text{x}10^{-5}$	$8\text{x}10^{-5}$	$1.633\text{x}10^{-4}$
110	0.0018	780	$1\text{x}10^{-4}$	$8\text{x}10^{-5}$	$1.729\text{x}10^{-4}$
120	0.0034	1130	$1\text{x}10^{-4}$	$1.5\text{x}10^{-4}$	$2.247\text{x}10^{-4}$
130	0.0026	1050	$1\text{x}10^{-4}$	$1.4\text{x}10^{-4}$	$3.390\text{x}10^{-4}$

TABLE A.3: Parameters for the fitting of the time-dependent pressure at varying Ar - H_2O content

Water Vapor Content (%)	Y_c	n_{layer}	α_{sub}	α_t	χ^2
0%	0	5410	$1\text{x}10^{-5}$	$1\text{x}10^{-5}$	$5.223\text{x}10^{-5}$
20%	0.0029	1960	$3\text{x}10^{-5}$	$5\text{x}10^{-5}$	$4.060\text{x}10^{-5}$
40%	0.0048	1240	$4\text{x}10^{-5}$	$9\text{x}10^{-5}$	$1.972\text{x}10^{-4}$
50%	0.0034	890	$5\text{x}10^{-5}$	$1.1\text{x}10^{-4}$	$1.352\text{x}10^{-4}$
60%	0.0043	950	$7\text{x}10^{-5}$	$1.7\text{x}10^{-4}$	$1.494\text{x}10^{-4}$
80%	0.0047	880	$1\text{x}10^{-4}$	$1.3\text{x}10^{-4}$	$1.006\text{x}10^{-4}$
100%	0.0025	720	$9\text{x}10^{-5}$	$8\text{x}10^{-5}$	$1.637\text{x}10^{-4}$

Appendix B

Energy Distribution from Retarding Potential Analyzers

The energy distribution of the ions collected by a retarding potential analyzer (RPA) is based on the current collected at the Faraday cup. The current, I collected can be described as:

$$I = qnA \int_{v_{min}}^{\infty} v f(v) dv \tag{B.1}$$

where v_{min} is the minimum velocity required to pass through the retardation plate voltage. The velocity of the particle can be correlated depending on the relation with the retardation potential for singly charged species:

$$\frac{1}{2} m v^2 = qV \tag{B.2}$$

and the velocity distribution can be transformed to the energy distribution based on:

$$f(v) dv = g(E) dE \tag{B.3}$$

where $E = \frac{1}{2} m v^2$. Taking this into account and eliminating the derivative terms, the energy distribution $g(E)$ can be expressed as:

$$f(v) = m v g(E) \tag{B.4}$$

To obtain the energy distribution, the derivative of Eq. B.1 is taken to remove the integral portion of the equation:

$$\frac{dI}{dV} = \frac{d}{dV} (nqA \int_{v_{min}}^{\infty} v f v \frac{dv}{dV} dV) \tag{B.5}$$

The evaluation of this equation involves taking the relation of the current of the RPA at a certain potential, V, described as:

$$I_{RPA}(E) = I(V = 0) - I(V) \tag{B.6}$$

which would result to the following equation, and its simplification:

$$\frac{dI}{dV} = -nqAvf(v)\frac{d(\sqrt{\frac{2qV}{m}})}{dV} \tag{B.7}$$

$$\frac{dI}{dV} = -nqAvf(v)(\sqrt{\frac{2qV}{m}})\frac{1}{2V^{\frac{1}{2}}} \tag{B.8}$$

$$\frac{dI}{dV} = -nqAvf(v)\frac{q}{mu} \tag{B.9}$$

$$\frac{dI}{dV} = -\frac{nq^2A}{m}f(v) \tag{B.10}$$

$$\frac{dI}{dV} = -nq^2A\sqrt{\frac{2qV}{m}}g(E) \tag{B.11}$$

For multiple reactive species plasma, where obtaining an effective ion mass is difficult, the energy distribution in the plasma can be related to the shape of the negative first derivative of the RPA current:

$$-\frac{dI}{dV} \propto g(E) \tag{B.12}$$